EARTH SCIENCE AND RESOURCE ENGINEERING
www.csiro.au

GEOMECHANICAL MODELLING OF TRAP INTEGRITY IN THE NORTHERN OFFSHORE PERTH BASIN

A collaboration between CSIRO and Geoscience Australia

Laurent Langhi[1], Yanhua Zhang[1], Chris Nicholson[2], George Bernardel[2], Nadège Rollet[2], Peter Schaubs[1], Richard Kempton[1] and John Kennard[2]

[1] CSIRO Earth Science and Resources Engineering

[2] Geoscience Australia

CSIRO Open File Report EP12425

March 2012

Australian Government
Geoscience Australia

Enquiries should be addressed to:

Dr Laurent Langhi

CSIRO Earth Science and Resource Engineering

26 Dick Perry Avenue

Kensington, WA, 6151

AUSTRALIA

Laurent.Langhi@csiro.au

+61 8 6436 8741

Dr Richard Kempton

CSIRO Earth Science and Resource Engineering

26 Dick Perry Avenue

Kensington, WA, 6151

AUSTRALIA

Richard.Kempton@csiro.au

+61 8 6436 8537

Citation

Langhi et al., (2012) GEOMECHANICAL MODELLING OF TRAP INTEGRITY IN THE NORTHERN OFFSHORE PERTH BASIN. CSIRO Open File Report EP12425, CSIRO Australia.

Copyright and disclaimer

Important disclaimer

Contents

Contents i

Figures iii

Tables viii

Executive summary ix

1 Introduction 10

1.1 Tectonic setting of the offshore northern Perth Basin 10

2 Geomechanical Modelling Methods 13

2.1 Geomechanical fault seal prediction 13
  2.1.1 Fracture stability 14
  2.1.2 Slip stability 14
  2.1.3 Slip tendency 14
  2.1.4 Dilation tendency 14
  2.1.5 Stress regime 15
  2.1.6 Rock and fault rock properties 16

2.2 Geomechanical deformation modelling based on finite difference code 16
  2.2.1 Model architecture: faults and stratigraphy 18
  2.2.2 Model material properties 19
  2.2.3 Boundary conditions 20

3 Cliff Head Oilfield 21

3.1 Geomechanical fault seal prediction - Cliff Head 22
  3.1.1 Fracture stability 24
  3.1.2 Slip stability 26
  3.1.3 Slip tendency 27
  3.1.4 Dilation tendency 29

3.2 Geomechanical deformation modelling – Cliff Head 30
  3.2.1 Strain distribution 32
  3.2.2 Stress distribution 35

3.3 Discussion - Cliff Head 36

4 Dunsborough Oil/Gas Discovery and Lilac Breached Trap 39

4.1 Geomechanical fault seal prediction – Dunsborough and Lilac 40
  4.1.1 Fracture stability 41
  4.1.2 Slip stability 44
  4.1.3 Slip tendency 45

4.1.4 Dilation tendency 47
4.2 Geomechanical deformation modelling – Dunsborough and Lilac 48
4.2.1 Strain distribution 48
4.2.2 Stress distribution 53
4.3 Discussion – Dunsborough/Lilac 55
4.3.1 Dunsborough and Lilac palaeo-accumulation 56
4.3.2 Geomechanical models and palaeo-accumulations 58
4.3.3 Fault slip history – Dunsborough and Lilac 60
5 Morangie Breached Trap 62
5.1 Geomechanical fault seal prediction – Morangie 62
5.1.1 Fracture stability 63
5.1.2 slip stability 66
5.1.3 Slip tendency 67
5.1.4 Dilation tendency 68
5.2 Geomechanical deformation modelling – Morangie 70
5.2.1 Strain distribution 70
5.2.2 Stress distribution 74
5.3 Discussion – Morangie 74
6 Trap Intergity Risk Factors In The Northern Perth Basin 76
7 Limitations and Future Directions 85
8 Conclusions 86
References 87
Appendix A – Palaeo-Oil Charge Reconstructions 92

Figures

Figure 1: Structural elements of the offshore Perth Basin showing location of 3D seismic surveys, exploration wells and 2011 release area W11-18. 11

Figure 2: Generalised stratigraphic column for the northern Perth Basin showing location of oil and gas discoveries. Modified from Roc Oil Company Ltd........ 12

Figure 3: Stress regime used for the geomechanical fault seal prediction model based on data from the Cliff Head Field and the present-day sedimentary column. The horizontal guidelines represent the stress state for the Cliff Head reservoir for different erosion scenarios. Data is from GeoMechanics International (2003). 16

Figure 4: Architecture of the Cliff Head model without the overburden. Mesozoic faults=blue, Geraldton Fault=red. The Permian faults are inside the host rocks and are invisible in the image........ 18

Figure 5: Architecture of the Dunsborough/Lilac model without the overburden. Faults (blue) are blind faults and are buried within the top sandstone layer above the shale layer........ 19

Figure 6: Architecture of the Morangie model without the overburden. Faults (blue) are blind faults and are buried within the top sandstone layer above the shale layer. 19

Figure 7: Post-drill Cliff Head-6 depth map of the Cliff Head structure (top Permian reservoir) and oil-water contact (OWC) (modified from Roc Oil, 2005). Location of Main Horst and East Ridge are indicated (Roc Oil terminology). The west-dipping Geraldton Fault is shown. Blue box is the 3D seismic location....... 22

Figure 8: Permian faults for the geomechanical fault seal prediction and top reservoir structure. 23

Figure 9: Fracture stability for the Permian faults at 2275 m below elevation (including 1000m of eroded sediments; chosen as the approximate depth of the top Permian reservoir before erosion). The values on the stereonets (right) refer to the increase in pore pressure required to force the plane into failure; the same values are shown on the Mohr circle (left) with the failure envelope (red) defined by the fault rock properties. (A) Cohesive strength of 1 MPa and coefficient of internal friction of 0.3. (B) Cohesive strength of 5 MPa and coefficient of internal friction of 0.6. 25

Figure 10: Fracture stability distribution (cohesive strength of 1 MPa and an internal coefficient of friction of 0.3). Maximum fracture stability is blue and minimum fracture stability in red. (A) View from the east showing the higher stability of fault 1 and the low stability of faults 7 and 8. (B) View from the west showing the low stability for the faults oriented to the NNE, i.e. faults 5, 6, 7 and 8........ 26

Figure 11: Slip stability for the Permian faults at 2275 m below elevation (including 1000m of eroded sediments). Faults are cohesionless and coefficient of internal friction is 0.486. The values on the stereonets refer to the increase in pore pressure required to force the plane into failure. The values on the stereonets (right) refer to the increase in pore pressure required to force the plane into failure; the same values are shown on the Mohr circle (left) with the failure envelop (red) defined by the fault properties........ 27

Figure 12: Slip tendency for the Permian faults at 2275 m below elevation (including 1000 m of eroded sediments). The values on the stereonets (right) refer to the likelihood of slip to occur; the same values are shown on the Mohr circle (left)........ 28

Figure 13: Slip tendency distribution. (A) View from the east showing the higher tendency of NNE oriented faults and the low tendency of NW oriented faults. Maximum slip tendency is red and minimum slip tendency is blue. (B) View from the west showing the variation in slip tendency on the NNE oriented fault 7 and the NW oriented fault 1........ 29

Figure 14: Dilation tendency for the Permian faults at 2275 m below elevation (including 1000 m of eroded sediments). The values on the stereonets (right) refer to the likelihood of dilation to occur; the same values are shown on the Mohr circle (left). 29

Figure 15: Dilation tendency distribution. Maximum dilation tendency is red and minimum dilation tendency is blue. (A) View from the east showing the higher tendency of NNE oriented faults and the low tendency of NW oriented faults. (B) View from the west. 30

Figure 16: Structural scenarios used in the deformation modelling of the Cliff Head Field. (A) Model overview with mechanical layers, brown=basement, blue=sandstone/reservoir, purple=shale/top seal, green=sandstone/overburden. (B) Scenario 1. (C) Scenario 2. (D) Scenario 3. 31

Figure 17: Location of cross-sections over the Cliff Head Field displayed in Figure 18 and Figure 20. I-II intersects the East Ridge and III-IV intersects the Main Horst. 32

Figure 18: Shear strain distribution in section for structural scenario 1. The lower faults are the reactivated Permian reservoir faults and the upper faults are the Mesozoic faults. Maximum strain is red and minimum strain is blue. (A) Shear strain distribution for the East Ridge. (B) Detail shear strain distribution for the East Ridge. (C) Shear strain distribution for the Main Horst. (D). Detail shear strain distribution for the Main Horst 33

Figure 19: Shear strain distribution in plan view (intra reservoir horizon). Maximum strain is red and minimum strain is blue. (A) Shear strain distribution of the main Permian faults for the Cliff Head Field and the regional Geraldton Fault. (B) Detail shear strain distribution of the main Permian faults for the Cliff Head Field 34

Figure 20: Volumetric strain distribution in section for structural scenario 1. The lower faults are the reactivated Permian reservoir faults and the upper faults are the Mesozoic faults. Maximum strain is red and minimum strain is blue. (A) Volumetric strain distribution for the East Ridge. (B) Volumetric strain distribution for the Main Horst. 34

Figure 21: Volumetric strain distribution in plan view for the Cliff Head Field (intra reservoir horizon). Maximum strain is red and minimum strain is blue. 34

Figure 22: Shear strain vs. bulk extension. (A) Reactivated Permian trap-bounding faults. (B) Mesozoic faults. 35

Figure 23: Plan-view stress patterns for a horizon within the reservoir rock in the model for the Cliff Head Field. (A) Mean stress. Values are all negative which indicate compressive stresses. (B) Shear stress.. . 36

Figure 24: Current oil-water contact (OWC) superimposed on Permian fault shear strain distribution for the Cliff Head Field. Maximum strain is red and minimum strain is blue. 37

Figure 25: 3D shear strain distribution showing the shielding effect of the Geraldton Fault on the Cliff Head Field. The Y direction refers to the north, the X direction refers to the east. Maximum strain is red and minimum strain is blue. 38

Figure 26: Throw distribution on the Permian and Mesozoic faults for the Cliff Head structure. 38

Figure 27: Dunsborough and Lilac structures. Base Kockatea Shale depth converted horizon. 40

Figure 28: Permian faults for the geomechanical fault seal prediction and top reservoir structure. Fault labels refer to the geomechanical fault seal prediction (4.1); different labels are used for the geomechanical deformation modelling (4.2). 41

Figure 29: Fracture stability for the Permian faults at 3400 m below elevation (including 2000 m of eroded sediments; chosen as the approximate depth of the top Permian reservoir before erosion). The values on the stereonets (right) refer to the increase in pore pressure required to force the fault plane into failure; the same values are shown on the Mohr circle (left) with the failure envelope (red) defined by the fault rock properties. (A) Cohesive strength of 1 MPa and coefficient of internal friction of 0.3. (B) Cohesive strength of 5 MPa and coefficient of internal friction of 0.6. 42

Figure 30: Fracture stability distribution (cohesive strength of 1 MPa and an internal coefficient of friction of 0.3). Maximum fracture stability is blue and minimum fracture stability red. The top reservoir surface is coloured for depth. 43

Figure 31: Fracture stability distribution (Cohesive Strength of 5 MPa and an internal coefficient of friction of 0.6). Maximum fracture stability is blue and minimum fracture stability red.The top reservoir surface is coloured for depth. 44

Figure 32: Slip stability for the Permian faults at 3400m below ground elevation (including 2000m of eroded sediments). Faults are cohesionless and coefficient of internal friction is 0.48. The values on the stereonets (right) refer to the increase in pore pressure required to force the fault plane into failure; the same values are shown on the Mohr circle (left) with the failure envelop (red) defined by the fault properties. 45

Figure 33: Slip tendency for the Permian faults at 3400m below ground elevation (including 2000m of eroded sediments). The values on the stereonets (right) refer to the likelihood of slip to occur; the same values are shown on the Mohr circle (left). 46

Figure 34: Slip tendency distribution. Areas of high slip tendency are present on the trap-bounding faults 1 (Dunsborough) and L1 (Lilac) (black arrows). Maximum slip tendency is red and minimum slip tendency is blue. The top reservoir surface is coloured for depth. 46

Figure 35: Dilation tendency at 3400m below ground elevation (including 2000m of eroded sediments). The values on the stereonets (right) refer to the likelihood of dilation to occur; the same values are shown on the Mohr circle (left). 47

Figure 36: Dilation tendency distribution. Maximum dilation tendency is red and minimum dilation tendency is blue. The top reservoir surface is coloured for depth. 48

Figure 37: 3D shear strain distribution and location of cross-sections and plan views. Maximum strain is red and minimum strain is blue. 49

Figure 38: Shear strain distribution in plan view after 2% extension. Maximum strain is red and minimum strain is blue. (A) Horizontal slice at 800m below seabed. (B) Horizontal slice at 1000m below seabed. (C) Horizontal slice at 1500m below elevation, i.e. near top reservoir level. The red arrows show local decrease in shear strain accommodation on NW oriented segments. Yellow arrows show local increase in shear strain accommodation on NNW oriented segments adjacent to low strain segments. (D) Horizontal slice at 2000m below seabed. 50

Figure 39: Volumetric strain distribution in plan view after 2% extension. Maximum strain is red and minimum strain is blue. (A) Horizontal slice at 800m below seabed. (B) Horizontal slice at 1000m below seabed. (C) Horizontal slice at 1500m below seabed, i.e. near top reservoir level. The red arrows show local decrease in shear strain accommodation on NW oriented segments. Yellow arrows show local increase in volumetric strain accommodation on NNW oriented segments adjacent to low strain segments. (D) Horizontal slice at 2000m below seabed. 51

Figure 40: Shear strain distribution in cross-section view after 2% extension. Maximum strain is red and minimum strain is blue. 52

Figure 41: Volumetric strain distribution in cross-section view after 2% extension. Maximum strain is red and minimum strain is blue. 53

Figure 42: 3D shear strain distribution after 2% extension. Maximum strain is red and minimum strain is blue. (A) South-east view. (B) South-west view showing the lateral variation in shear strain distribution for fault F1. 53

Figure 43: Plan-view stress patterns for a horizon at the 800m level in the model for the Dunsborough Field and Lilac structure. (A) Mean stress. (B) Shear stress. For mean stresses, negative values denote compressive stresses. Shear stresses all have positive values. 54

Figure 44: Plots of mean stress patterns for 4 cross-sections in the model for the Dunsborough Field and Lilac structure. Negative values denote compressive stresses. Cross-section locations are shown in Figure 37. 55

Figure 45: Plots of shear stress patterns for 4 cross-sections in the model for the Dunsborough Field and Lilac structure. Cross-section locations are shown in Figure 37. 55

Figure 46: Palaeo-charge scenarios for the Dunsborough Field. (A) Dunsborough-2 well with GOI data and oil shows. P-OWC1a is the palaeo-oil-water contact for the first charge scenario based on the GOI data. P-OWC2a is the palaeo-oil-water contact for the second charge scenario based on the GOI data and oil shows. P-OWC1 is the common depth range for both P-OWCs defined in Dunsborough-1 and -2 for the first charge scenario. (B) Dunsborough-1 well with GOI data and oil shows. P-OWC1a is the palaeo-oil-water contact for the first and second charge scenario based on the GOI data and oil shows. D-POWC2 is the deepest palaeo-oil-water contact based on the GOI data located 25 m above P-OWC2a (see text for discussion). (C) A post charge block rotation, coeval with the Middle-Jurassic to Early Cretaceous reactivation could be responsible for the depth of P-OWC2a in Dunsborough-2........................ 57

Figure 47: Relationship between shear strain distribution and charge history for the Dunsborough trap. . Top reservoir depth in m SS. (A) Shear strain distribution and present-day structure. (B) Shear strain distribution and possible palaeo-oil column down to c. 1535 mRT (c. 1505 mSS). (C) Shear strain distribution and present-day oil column. 59

Figure 48: Relationship between shear strain distribution and charge history for the Lilac trap. Top reservoir depth in mSS. (A) Shear strain distribution and present-day structure. (B) Shear strain distribution and palaeo-oil column down to c. 1420 mRT (c. 1390 mSS). 60

Figure 49: on the Permian and Mesozoic faults for the Dunsborough and Lilac structures. A) Throw distribution with the Lilac bounding-fault F4 in the foreground. B) Throw distribution with the Dunsborough bounding-fault F2 in the foreground. 61

Figure 50: Permian faults for the geomechanical fault seal prediction and top reservoir structure. Fault labels refer to the geomechanical fault seal prediction (5.1); different labels are used for the geomechanical deformation modelling (5.2). 63

Figure 51: Fracture stability for the Permian faults at 1900 m below ground elevation (including 300 m of eroded sediments; chosen as this is the approximate depth of the top Permian reservoir during Middle Jurassic to Early Cretaceous extension and prior to Early Cretaceous erosion). The values on the stereonets (right) refer to the increase in pore pressure required to force the fault plane into failure; the same values are shown on the Mohr circle (left) with the failure envelop (red) defined by the fault rock properties. (A) Cohesive strength of 1 MPa and coefficient of internal friction of 0.3. (B) Cohesive strength of 5 MPa and coefficient of internal friction of 0.6. 64

Figure 52: Fracture stability distribution for a (cohesive strength of 1 MPa and an internal coefficient of friction of 0.3). Maximum fracture stability is blue and minimum fracture stability red. The top reservoir surface is coloured for depth. (A) View from the east. (B) View for the south-west, The black arrow shows a decrease of fracture stability near Morangie-1. 65

Figure 53: Fracture stability distribution (cohesive strength of 5 MPa and an internal coefficient of friction of 0.6). Maximum fracture stability is blue and minimum fracture stability red. The top reservoir surface is coloured for depth. (A) View from the east. (B) View for the south-west.................................... 66

Figure 54: Slip stability for the Permian faults at 1900 m below ground elevation (including 300 m of eroded sediments). Faults are cohesionless and coefficient of internal friction is 0.48. The values on the stereonets (right) refer to the increase in pore pressure required to force the fault plane into failure; the same values are shown on the Mohr circle (left) with the failure envelop (red) defined by the fault properties.. 67

Figure 55: Slip tendency for the Permian faults at 1900 m below ground elevation (including 300 m of eroded sediments). The values on the stereonets (right) refer to the likelihood of slip to occur; the same values are shown on the Mohr circle (left)... 68

Figure 56: Slip tendency distribution. Maximum slip tendency is red and minimum slip tendency is blue. The top reservoir surface is coloured for depth. Areas of higher slip tendency (white arrows) are present

on the trap-bounding faults F3 (at the trap crest) and F1 (down-dip of the trap crest). The top reservoir surface is coloured for depth. (A) View from the east. (B) View from the south-west. 68

Figure 57: Dilation tendency distribution. The values on the stereonets (right) refer to the likelihood of dilation to occur; the same values are shown on the Mohr circle (left). 69

Figure 58: Dilation tendency distribution. Maximum dilation tendency is red and minimum dilation tendency is blue. The top reservoir surface is coloured for depth. (A) View from the east. (B) View from the south-west. 70

Figure 59: Shear strain distribution in plan view after 2% extension. Maximum strain is red and minimum strain is blue. (A) Horizontal slice at 1000 m below ground elevation. (B) Horizontal slice at 1500 m below elevation. (C) Horizontal slice at 2000 m below elevation, i.e. near top reservoir level. (D) Horizontal slice at 3000 m below ground elevation. Black dot is Morangie-1 location. 71

Figure 60: Volumetric strain distribution in plan view after 2% extension. Maximum strain is red and minimum strain is blue. (A) Horizontal slice at 1000 m below ground elevation. (B) Horizontal slice at 1500 m below ground elevation. (C) Horizontal slice at 2000 m below ground elevation, i.e. near top reservoir level. (D) Horizontal slice at 3000 m below ground elevation. Black dot is Morangie-1 location....72

Figure 61: 3D distribution of shear strain (A) and volumetric strain (B). Maximum strain is red and minimum strain is blue. 73

Figure 62: Plan-view stress patterns for a horizon of -1500 meter depth in the model for the Morangie field. (A) Mean stress. (B) Shear stress. F1-F4 denotes fault traces. For mean stresses, negative values denote compressive stresses. Shear stresses all have positive values. Black dot is Morangie-1 location. 74

Figure 63: Relationship between shear strain distributions, geometry and charge history for the Morangie structure. Maximum strain is red and minimum strain is blue. (A) Shear strain distribution and present-day structure. Isolines are form 2050 mSS to 2250 mSS. (B) Shear strain distribution and palaeo-oil column down to c. 2160 mRT (c. 2130 mSS). Black dot is Morangie-1 location. 75

Figure 64: Fault seal risk based on fault orientation for the fields and prospects modelled. Integrated geomechanical fault seal prediction, geomechanical deformation models and charge data suggest that fault planes oriented between the NNW (~340°) and ESE (~100°) are likely to reactivate under the Middle Jurassic to Early Cretaceous stress regime (upper right) and allow fluid flow. Sealing and leaking faults from the modelled areas are plotted (green and red respectively). Note that the WNW oriented segment of the fault bounding the dry Morangie structure lies within the low risk area although along fault leakage was possible. In this case the intersection of fault planes (and not the fault orientation) was probably the driving factor for fault reactivation and top seal bypass. 77

Figure 65: Comparison between the fault seal risk and the orientation of trap bounding faults in the offshore northern Perth Basin. The main trap bounding faults are identified by their orientation. Green dots refer to faults bounding current accumulations (i.e. sealing fault); red dots refer to faults that offset the top seal and bound dry structures with a palaeo accumulation (i.e. top seal bypass and along fault fluid flow is the suggested cause of leakage), red/green dot refers to faults with indication of leakage and currently holding a hydrocarbon column (healed fault), orange dots refer to faults bounding dry structure with no oil show (lack of charge or undetected migration pathway?), red/green dots with question mark refer to faults bounding a gas accumulation with a palaeo oil column resulting either from oil displaced by gas or oil leaked along the fault plane. Note the leaking faults are mostly orientated between the NNW (335°) and the NNE (20°), which correlates with the risk prediction form the geomechanical models. Faults oriented to the NNW (i.e. 330° - 340°) in the transition zone between high and low reactivation risk - can either seal or leak. Faults oriented to the NW are likely to seal. 78

Figure 66: Strain distribution on trap bounding faults. (A) Shear strain from the trap bounding faults for the Cliff Head, Dunsborough, Lilac and Morangie structures. A threshold around 0.1 is proposed to differentiate between sealing faults and leaking fault breaching the top seal. Shear strain value near the threshold might induce short term fault breach followed by fault self healing process. (B) Volumetric strain from the trap bounding faults for the Cliff Head, Dunsborough, Lilac and Morangie structures. A

threshold around 0.05 is proposed to differentiate between sealing faults and leaking fault breaching the top seal. Shear strain value near the threshold might induce short term fault breach followed by fault self healing process. 80

Figure 67: Top seal (Kockatea Shale) thickness in the offshore northern Perth Basin. 82

Figure 68: Comparison between top seal (Kockatea Shale) thickness and top seal bypass risks in the offshore northern Perth Basin. The group of wells on the left represents the four discoveries arranged form south to north. The group of wells in the middle represents dry structures with palaeo-accumulations and with along fault flow suggested as the cause of leakage. The group of wells on the right represents dry structures without oil shows. The bar colours refer to the risk of reactivation for the crest bounding faults as shown in Figure 65. 83

Figure 69. Mechanical properties of the Kockatea Shales seal. (A) Uniaxial compressive strength (UCS) in MPa for Cliff Head-1, Dunsborough-2, Perseverance-1, Lilac-1 and Flying Foam-1. Low UCS values represent incompetent facies and high UCS values represent competent facies; a classic range of UCS for shales is 5 MPa – 100 MPa. The soft-linkage observed over the Cliff Head oilfield cannot be attributed to a more incompetent Kockatea Shales; the average UCS for Cliff Head-1 is 28 MPa, which similar to the average UCS at locations where hard-linkage developed (Dunsborough-2, Perseverance-1, Lilac-1). (B) Brittleness index (BRI) for Cliff Head-1, Dunsborough-2, Lilac-11 and Flying Foam-1. For BRI>2 the risk of embrittlement increases with increasing BRI. The soft-linkage observed over the Cliff Head oilfield cannot be attributed to a more ductile Kockatea Shales; the BRI for Cliff Head-1 is between 3 and 6, which higher than the BRI at locations where hard-linkage developed (Dunsborough-2, Lilac-1, Flying Foam-1). 84

Figure 70: Cliff Head oilfield— GOI log. 94

Figure 71: Dunsborough oil/gas discovery— GOI log. 95

Figure 72: Lilac-1— GOI log. 96

Figure 73: Morangie-1— GOI log. 97

Tables

Table 1: Initial properties of the Cliff Head Dunsborough/Lilac and Morangie numerical models. 20

Executive summary

Recent work in the offshore northern Perth Basin revealed a widespread charge system for oil accumulation below the Triassic Kockatea Shale regional seal and identified trap integrity as a likely cause for the high incidence of breach traps. This report details the results of a trap integrity study in which 3D geomechanical modelling was used to simulate the response of a complex set of trap-bounding faults to Middle Jurassic to Early Cretaceous extensional reactivation and to investigate the hydrocarbon preservation risk in the Abrolhos Sub-basin and Wittecarra Terrace. The modelling focused on four structures; the Cliff Head and Dunsborough oil discoveries and the Lilac and the Morangie breached traps. Additional fields and prospects were also included in a regional discussion and for comparison with the modelling results. Two modelling techniques were used:

1. *Geomechanical fault seal prediction* assesses the likelihood of fault surfaces to be active and conduct fluid within the current stress regime. It predicts fault seal attributes, which may control leakage through fractures associated with fault planes.
2. G*eomechanical deformation* modelling is a finite-difference approach which simulates impact of regional and local deformations on the distribution of reactivated and dilatant faults.

Strain-accommodating faults intersecting a reservoir top seal have shown to act as conduits for fluids and, so create seal bypass. The main factors controlling the accommodation of reactivation strain in the northern offshore Perth Basin includes: (i) fault strike orientation–faults oriented between NNW (~340°) and ESE (~100°) are more likely to fail, while fault segments oriented to the NW are more prone to seal and, (ii) intersections of fault planes that generate zones of high shear deformation and dilation. Fault strike length is also a significant factor controlling strain partitioning as reactivation strain tends to progressively localize onto the largest faults over time, which then act to protect neighbouring structures.

Fault growth and linkage style during reactivation represents a key element in the development of seal bypass. The Cliff Head, Dunsborough and Lilac structures show that this strain nucleates into new sets of Late Jurassic faults and also reactivates Permian trap-bounding faults. As deformation accumulates, the Jurassic faults propagate downwards towards the top seal and the reactivated Permian faults propagate upward into the top seal. Based on the magnitude of reactivation strain, either soft-linkage or hard-linkages develop between these two systems. Hard-linked faults are more likely to be associated with a critical increase in structural permeability and the development of migration pathways that bypass the top seal. The Cliff Head trap is an example of soft-linked faults through the top seal and currently supports an oil column.

Shear and volumtetric strain threshold values can be used to locally can be defined to differentiate between sealing and leaking faults (0.1 and 0.05 for shear and volumetric strain respectively).

The top seal thickness variations do not appear to represent a first order risk factor for the development of hard-linked top seal bypass. Several breached structures associated with hard-linked faults have top seals thicker than the Cliff Head top seal (~300 m). However, all these structures have crest trap faults with either (i) a high risk of reactivation due to their orientations, and/or (ii) intersection of fault planes (Flying Foam, Morangie, Livet). These suggest that structural parameters are the primary risk factors for the development of seal bypass rather than shale thickness or geomechanical properties.

In the light of this work, it appears that prevalence of breached oil columns in the basin can be partly explained by the general tendency to drill structural traps that: (i) are bounded by larger faults with large offsets (larger volume) and (ii) have risky NNW fault orientations that align with the regional structural grain. Both these elements represent key trap integrity risks.

1 Introduction

Critically stressed faults are widely cited as conduits for fluid flow (e.g. Anderson et al., 1994; O'Brien et al., 1999), and seal breach by fault reactivation represents a critical exploration risk for hydrocarbons in many petroleum provinces (Smith, 1966; Abrams, 1996; Sibson, 1996; Gartrell et al. 2006; Zhang et al., 2009; Langhi et al., 2010). In the northern offshore Perth Basin, Kempton et al. (2011a, 2011b) recently revealed a widespread charge system for oil with residual palaeo-oil columns detected in about 14 of 18 exploration wells. Implicit in the data was a validation of key petroleum system elements of oil-mature source, available trap and migration pathways from source to trap over a large area of the basin. The high incidence of palaeo-oil and residual columns, however, suggests that trap integrity and preservation of oil is likely to be a more important risk factor for exploration.

This report details results of a CSIRO-led study, in collaboration with Geoscience Australia, on trap integrity in the northern offshore Perth Basin. To investigate the hydrocarbon preservation risks, three-dimensional (3D) geomechanical modelling methods were used to simulate the response of a relatively complex set of trap-bounding faults to Mesozoic extensional reactivation—that is, Middle Jurassic to Early Cretaceous extension that culminated in continental breakup in the Valanginian between Australia and greater India. This study focused on identifying first-order risk factors for trap breach in three areas covered by 3D seismic data, which included several drilled prospects with a mix of both breached and preserved oil columns — (i) the Cliff Head 3D survey over the Cliff Head oilfield, (ii) the Diana 3D survey over the Dunsborough well oil/gas discovery and Lilac prospect and, (iii) the Macallan 3D survey over the Morangie prospect (Figure 1).

1.1 Tectonic Setting of the offshore Northern Perth Basin

The regional geology and tectonic setting of the offshore northern Perth Basin is summarised by Jones et al. (2011), but generally comprises depocentres and structural features formed in an obliquely-oriented extensional rift system on Australia's southwest margin during the Palaeozoic to Mesozoic breakup of eastern Gondwana (Figure 1). The basin has had a complex, multi-phase history of extension and reactivation, and regional tectonic events that affected basin evolution and controlled sedimentation (Figure 2; generalised stratigraphic column) include: (i) Early to Middle-Permian east-northeast–west-southwest extension, (ii) Mid-Permian regional uplift, (iii) Late Permian to Late Triassic thermal subsidence, (iv) possible latest Triassic to Early Jurassic west-northwest–east-southeast extension, (v) Early Jurassic to Middle Jurassic thermal subsidence, (vi) Middle Jurassic to Late Jurassic northwest–southeast extension, (vii) Early Cretaceous northwest–southeast extension and local transpression, (viii) Valanginian regional uplift, breakup and basin inversion, (ix) Early Cretaceous to Cenozoic passive margin subsidence, and (x) Miocene inversion.

For this study we consider the Middle Jurassic to Early Cretaceous extension prior to continental break-up as the primary cause of fault reactivation and the likely mechanism behind potential trap breaching. This is consistent with the timing of hydrocarbon charge for oil from the Hovea Member (Figure 2) which is modelled to have occurred between the Late Jurassic and earliest Cretaceous (160-130 Ma) in mature source kitchens of the Abrolhos Sub-basin (Jones et al., 2011).

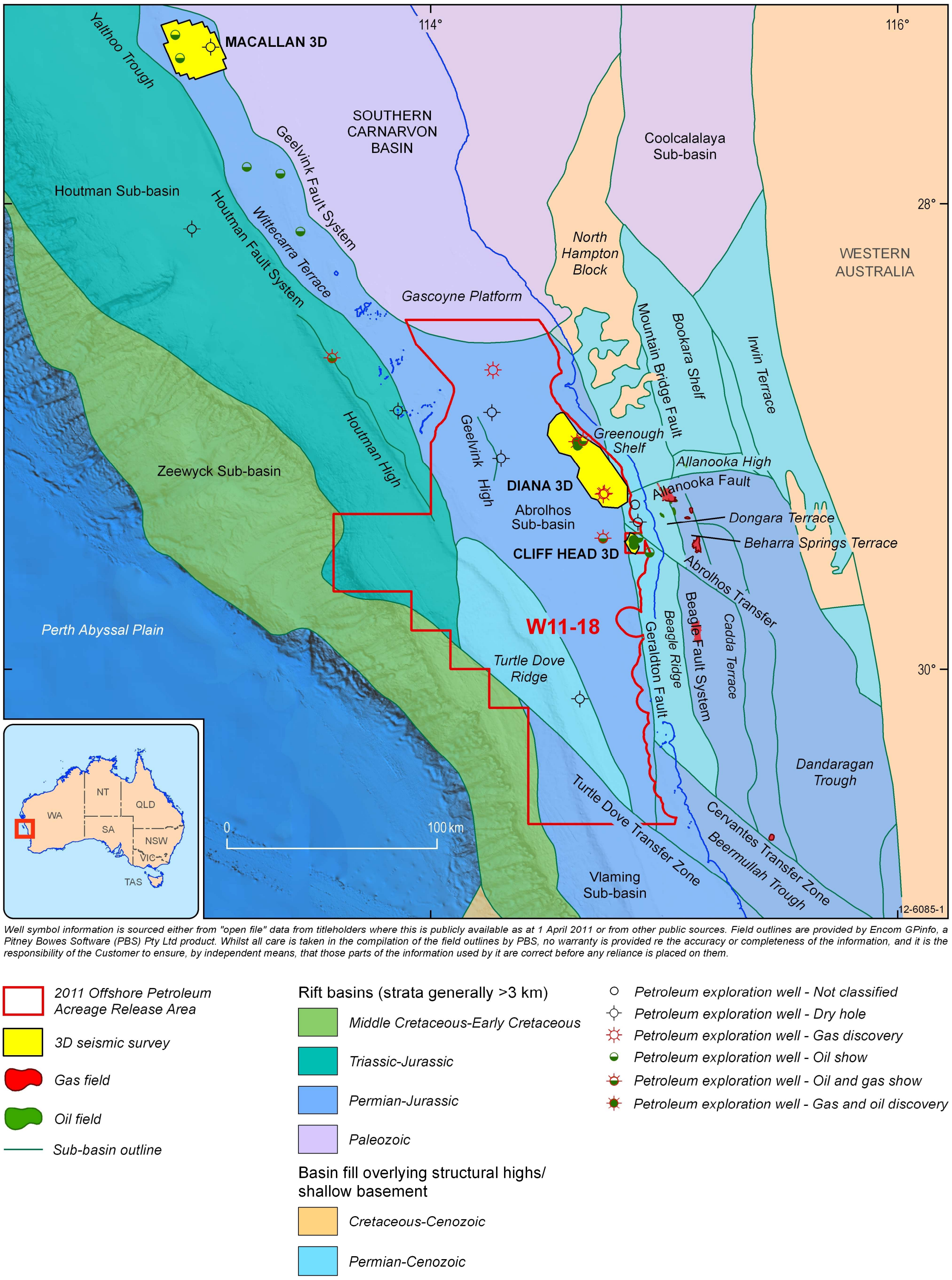

Well symbol information is sourced either from "open file" data from titleholders where this is publicly available as at 1 April 2011 or from other public sources. Field outlines are provided by Encom GPinfo, a Pitney Bowes Software (PBS) Pty Ltd product. Whilst all care is taken in the compilation of the field outlines by PBS, no warranty is provided re the accuracy or completeness of the information, and it is the responsibility of the Customer to ensure, by independent means, that those parts of the information used by it are correct before any reliance is placed on them.

Figure 1: Structural elements of the offshore Perth Basin showing location of 3D seismic surveys, exploration wells and 2011 release area W11-18.

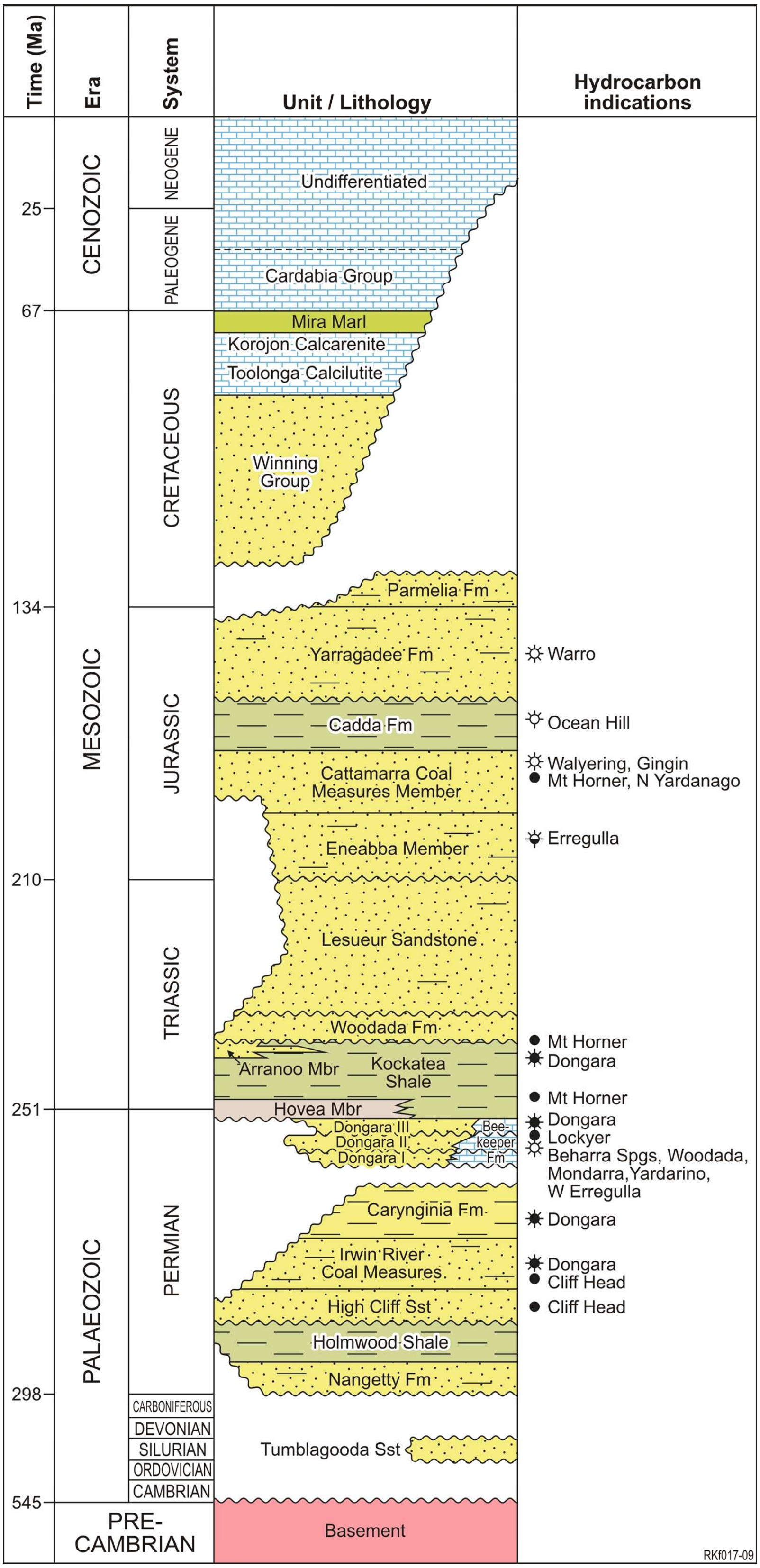

Figure 2: Generalised stratigraphic column for the northern Perth Basin showing location of oil and gas discoveries. Modified from Roc Oil Company Ltd.

2 Geomechanical Modelling Methods

Several geomechanics-based risking techniques have been applied to the study areas to assess the likelihood of shear failure occurring in the caprock and triggering up-fault leakage.

The first series of techniques relies on the *geomechanical fault seal prediction* method (see 2.1), which enables the modelling of the stress regime on the fault plane elements (i.e. faults are triangulated during modelling and each triangle represents an element with a dip and azimuth values). This method has been broken up into four components which potentially control leakage through fractures associated with the fault planes. The components of fracture stability, slip stability, slip tendency and dilation tendency concentrate on the likelihood of the fault surfaces to conduct fluid within the current stress regime.

The second series of techniques relies on *geomechanical deformation modelling based on a finite-difference code* (see 2.2 below), which enables the simulation of regional and local deformations to investigate the distribution of reactivated and dilatant faults. This modelling technique allows the determination of strain partitioning between structures and can be coupled with fluid flow modelling.

2.1 Geomechanical fault seal prediction

This approach focuses on the fault plane's interaction with the regional stress field and has been broken up into four attributes (i.e. fracture stability, slip stability, slip tendency and dilation tendency) which can control up-fault leakage and bypass of the caprock. Slip tendency and dilation tendency provide a ranking criterion to highlight which fracture orientations are more likely to reactivate and break a seal and/or be open and, thereby allow fluids to pass along the fault plane. These attributes are expressed as a ratio between 0 and 1, the higher the value the more likely the fault will dilate (extensional fractures) or slip and, so, the greater its ability to transmit fluids or gas.

In addition to these static measures of fault stability, the regional stress field data can be used to compute the risk of reactivation in terms of the increase in pore fluid pressure required to bring a fault, or parts of a fault, to a state of instability (i.e. fracture and slip stability attributes). The risk of reactivation is expressed as the increase in pore pressure required to induce failure. A low increase in pore pressure equates to a high risk of reactivation. Fault seals breached by reactivation can enhance fluid migration.

No simplification of the structural and stratigraphic model is required for the geomechanical fault seal prediction method and all faults interpreted from 3D seismic, for the three study areas, have been incorporated.

These attributes rely on the assumption that all faults optimally oriented will be associated with shear or tensile failure. However various studies have shown that strain can be heavily partitioned between faults during tectonic episodes. For example, Cowie (1998), Meyer et al. (2000), Walsh et al. (2003), Gartrell et al. (2005 and 2006) show that strain progressively localises onto increasingly larger faults during reactivation, leading to reduction and / or termination of activity on smaller faults.

2.1.1 FRACTURE STABILITY

Fracture stability considers the increase in pore pressure required to force a fault into shear or extensional failure under the conditions of the Coulomb failure. An increase in pore pressure corresponds to an arrival of buoyant fluid(s) such as hydrocarbons. That is, an increase in pore pressure can be related to a hydrocarbon column height. The factors which affect the magnitude of the increase needed to reach the failure envelope are:

- differential stress (i.e. maximum compressive stress - minimum principal stress)
- orientation of the fault plane within the stress field; and
- tensile strength, cohesive strength and the coefficient of friction

The failure mode (i.e. whether the fault will fail through shear failure, extensional-shear failure or extensional failure) will also depend on these factors. The lower the calculated fracture stability (i.e. the lower the increase in pore pressure required to induce failure), the higher the risk of fault plane reactivation and hence the higher the potential for fluid leakage along the fault.

2.1.2 SLIP STABILITY

Slip stability is a special case of fracture stability where the fault-rock is believed to have zero cohesive strength, meaning that only shear failure is possible. Slip stability is a measure of the increase in pore pressure required to enable slip on a fault in a particular orientation. The lower the slip stability, the higher the risk of the fault plane failing due to slip reactivation, hence the higher the potential of fluid migration along the fault.

2.1.3 SLIP TENDENCY

Analysis of slip tendency provides a way of assessing which faults are near the ideal orientation for slip to occur and are therefore the most likely to be associated with enhanced permeability (i.e. the greater the estimated slip tendency of a fault the more likely the fault is to leak). Slip tendency (Ts) is defined as the ratio of shear (τ) to normal stress (σ_n) acting on the fault surface.

$$Ts = \tau/\sigma_n$$

2.1.4 DILATION TENDENCY

Dilation tendency (Td) provides a ranking criterion to highlight which fracture orientations are more likely to be open and able to transmit fluids. The dilation tendency is a ratio ranging from 0 to 1, the higher the value the more likely the fault will dilate (extensional fractures) and the greater its ability to transmit fluids or gas. Dilation tendency is defined as:

$$Td = (\sigma_1 - \sigma_n)/(\sigma_1 - \sigma_3)$$

With σ_n the normal stress on the fault plane and σ_1 and σ_3 the maximum and minimum stresses respectively.

2.1.5 STRESS REGIME

The geomechanical fault seal prediction model relies on the assessment of the impact of the regional stress filed on the fault planes.

For this study we consider the Middle Jurassic to Early Cretaceous extensional stress regime as the primary cause of fault reactivation and the likely mechanism behind potential trap breaching. Bradshaw et al. (2003) proposed that the northwest–southeast extension during the Middle Jurassic to Early Cretaceous culminated in the break-up of Australia and Greater India during the Valanginian, and produced much of the final structural architecture of the Perth Basin. This represents the main phase of fault reactivation postdating the development of the Permian reservoirs. For a detailed description and discussion of the tectonic history of the Perth Basin the reader is referred to previous studies (Smith and Cowley, 1987; Marshall et al., 1993; Harris, 1994; Quaife et al., 1994; Mory and Iasky, 1996; Song and Cawood, 2000; Crostella and Backhouse, 2000; Gorter and Deighton, 2002 and Norvick, 2004).

The stress field used for the geomechanical fault seal prediction represents an extensional regime (Sv>SHmax>Shmin, Figure 3). The stress gradient used for the vertical stress Sv was 0.0235 MPa/m and is similar to the present-day vertical stress gradient defined for the Cliff Head oil field (GeoMechanics International, 2003). The gradient used for the horizontal stresses (SHmax and Shmin) were set to 0.018 MPa/m and 0.016 MPa/m respectively. This results in a stress state (using the present-day sedimentary column) at 1000 m below sea level characterised by Shmin=16 MPa, SHmax=19 MPa and Sv=21 MPa. However, burial history suggests that significant erosion may have occurred during the Valanginian breakup (e.g. Mory and Iasky, 1996) and for each study area we take into account an estimate of the eroded stratigraphic section that affected the stress field. Figure 3 shows the case for different amounts of erosion at the Cliff Head oil field.

For the three modelled sites we use 310N as the direction of extension consistent with Harris (1994) and Mory and Iasky (1996) and an average pore pressure gradient of 0.011 MPa/m is used for the geomechanical analysis Figure 3.

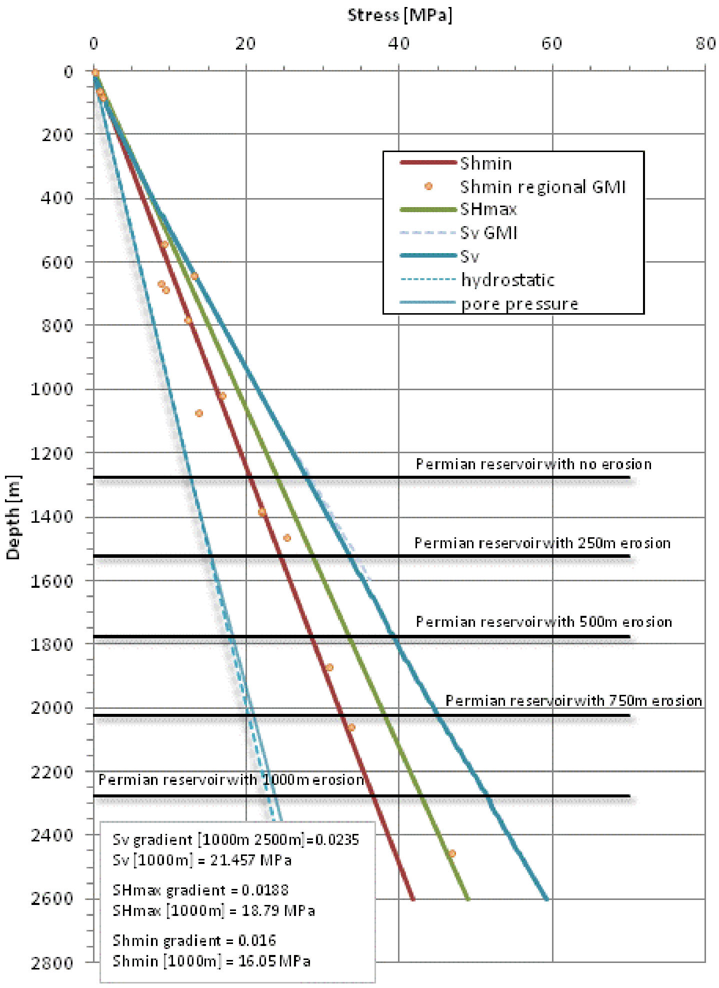

Figure 3: Stress regime used for the geomechanical fault seal prediction model based on data from the Cliff Head Field and the present-day sedimentary column. The horizontal guidelines represent the stress state for the Cliff Head reservoir for different erosion scenarios. Data is from GeoMechanics International (2003).

2.1.6 ROCK AND FAULT ROCK PROPERTIES

To define the fracture stability, as the Coulomb Failure Criterion for the fault rocks, coefficients of internal friction varying between 0.3 and 0.6 and cohesive strengths between 1 MPa and 5 MPa were used. To define the slip stability a coefficient of internal friction for the intact rock of 0.485 was used (i.e. average value for sandstone and shale).

2.2 Geomechanical deformation modelling based on finite difference code

FLAC3D™ (Fast Lagrangian Analysis of Continua) (Cundall and Board, 1988; Itasca, 2005) was used for the coupled geomechanical deformation modelling. This three-dimensional finite difference code enables the simulation of the interactions between deformation and fluid flow in rocks. The application of the code to geological problems is based on the use of constitutive laws governing deformation and fluid-flow behaviours, as described in Ord (1991), Ord and Oliver (1997), Strayer et al. (2001), and McLellan et al. (2004). As such, a brief description of the major aspects of the code is provided here.

In FLAC3D™ models, rock materials are represented by a 3-D continuum mesh consisting of hexahedral elements. Each element behaves according to prescribed mechanical and hydraulic laws. The mesh deforms and moves with the modelled materials in response to the applied boundary conditions. The mechanical deformation of the model is governed by the Mohr-Coulomb isotropic elastic-plastic constitutive law, which involves constitutive parameters including shear modulus (*G*), bulk modulus (*K*), cohesion (*C*), tensile strength (*T*), friction angle (ϕ), and dilation angle (ψ). Under mechanical loading, the modelled material deforms initially in an elastic manner until the maximum shear stress reaches the yield stress (a critical value), and then deforms plastically to a large strain after yielding. The Mohr-Coulomb yielding criteria can be described by:

$$|\tau_s| = C - \sigma_n \, tan \, \varphi$$

where τ_s is the shear stress and σ_n is the normal stress on the arbitrary plane in the material. The plastic strain is governed by a non-associated plastic flow law with constant cohesion, friction, and dilation angles (Vermeer and de Burst, 1984). Furthermore, tensile failure occurs when the effective minimum principal stress is in tension and overcomes rock tensile strength. A Mohr-Coulomb material may undergo volume changes (dilation is expressed as positive volume strain or volume increase) during plastic shearing deformation (Ord and Oliver, 1997). The dilatant potential of the Mohr-Coulomb material for plastic deformation is characterized by a positive dilation angle (ψ). Darcy's law for an isotropic porous medium is involved for the simulation of fluid flow and hydrological process. By coupling mechanical deformation and hydrological processes, the models consider the effects of hydrological conditions on mechanical deformation (i.e. effects of fluid pore pressure on the mechanical failure of rocks).

The units and convention of the strain and stress values presented below are:

- Shear strain (γ) involved here is the tensor shear strain and is defined by

  $$\gamma = 0.5 \times \tan A$$

  that is, half of the tangent of the shear angle (A); another common measure of shear strain is the engineering shear strain that is twice of the tensor shear strain. The shear angle reflects the change in the angle between pairs of lines that are initially perpendicular in a deforming body. Increase in the values of shear strain indicates the enhancement of deformation.
- Volumetric strain represents the ratio between the volumetric change and the initial volume. Negative values correlate with compaction and positive values correlate with dilation. For example, a volumetric strain of 0.01 means 1% volume increase or dilation for the examined location.
- Shear stress is the half of the differential stresses between the maximum and minimum principle stresses, expressed in Pascal [Pa]. Increasing values correlate with increasing shear stress.
- The mean stress is the mathematical average between the maximum, intermediate and minimum principal stresses (σ_1, σ_2 and σ_3), expressed in Pascal [Pa]. Negative values correlate with compressive stress and positive values with tensile stress.

2.2.1 MODEL ARCHITECTURE: FAULTS AND STRATIGRAPHY

The complexities in the structure of each of the three study areas (i.e. Cliff Head, Dunsborough/Lilac and Morangie) represent a significant challenge for building 3D meshes for deformation models. Simplifications to the fault architecture were deemed necessary for each area, with a preferential focus on major faults.

The *Cliff Head model* includes 11 faults (Figure 4): the regional Geraldton Fault, 5 Permian faults oriented NNE and NW (reservoir faults) and 5 overlying Mesozoic faults also oriented to the NNE and the NW. The Permian and Mesozoic faults are soft-linked and therefore treated as distinct planes. The model represents a box of 17.4 km (E-W) by 14.8 km (N-S) by 6 km (depth). The top reservoir, top seal horizons and top basement are interpreted from the Cliff Head 3D seismic data. A horizontal surface was used to approximate the seabed. A simplified stratigraphic framework was used for reflecting the main mechanical boundaries in the area. This framework consists of 4 rock units, from top to bottom: (1) a Triassic-Jurassic sandstone layer (overburden); (2) an Early Triassic shale layer (caprock); (3) a Palaeozoic sandstone layer (reservoir) and (4) a granite basement. The thicknesses of these layers are variable based on their 3D seismic expression. The Geraldton Fault is the largest fault in the area, with its root in the basement and is exposed on the sea floor. The trap-bounding faults are smaller, with the Permian faults situated below the shale layer, and the younger Triassic faults situated above the top of the shale layer and extending to the top surface of the model.

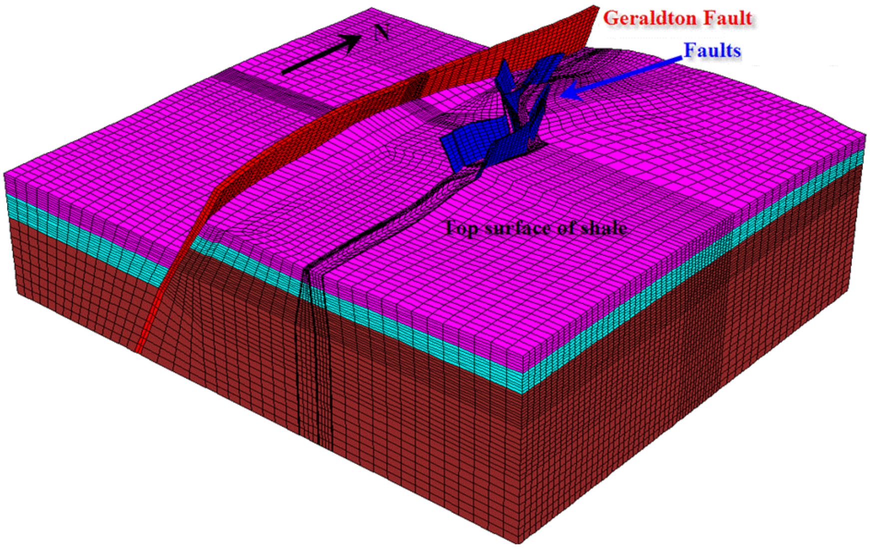

Figure 4: Architecture of the Cliff Head model without the overburden. Mesozoic faults=blue, Geraldton Fault=red. The Permian faults are inside the host rocks and are invisible in the image.

The *Dunsborough/Lilac model* includes 5 faults trending to the north and north-north-west (Figure 5). The model represents a box of 13.95 km (E-W) by 10.95 km (N-S) by 3 km (depth). The top reservoir and top seal horizons are interpreted from the Diana 3D seismic data. . The mechanical framework comprises 3 rock units, from top to bottom: (1) a Triassic-Jurassic sandstone layer (overburden); (2) an Early Triassic shale layer (caprock) and (3) a Palaeozoic sandstone layer (reservoir). The thicknesses of these layers are variable based on their 3D seismic expression. All fault planes penetrate through the top of the shale layer and extend into the Triassic-Jurassic sandstone layer but do not reach the top surface (i.e. blind faults).

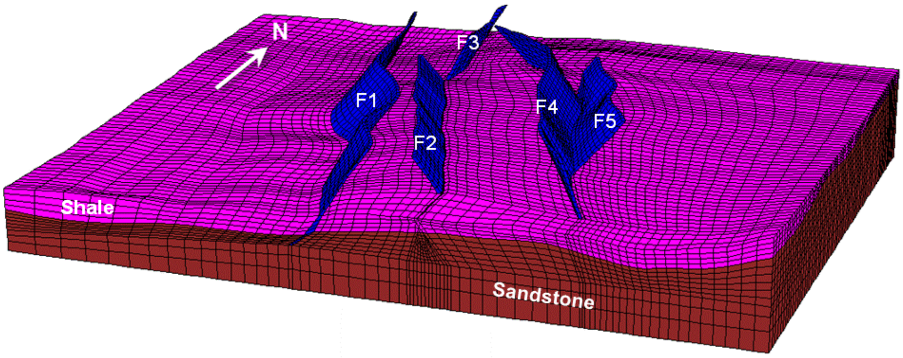

Figure 5: Architecture of the Dunsborough/Lilac model without the overburden. Faults (blue) are blind faults and are buried within the top sandstone layer above the shale layer.

The *Morangie model* includes 4 faults trending to the north-west and north-north-west (Figure 6). The model represents a box of 14.8 km (E-W) by 13.55 km (N-S) by 4 km (depth). The top reservoir and top seal horizons are interpreted from the Macallan 3D seismic data. The mechanical framework comprises 3 rock units, from top to bottom: (1) a Triassic-Jurassic sandstone layer (overburden); (2) an Early Triassic shale layer (caprock) and (3) a Palaeozoic sandstone layer (reservoir). The thicknesses of these units are variable based on their 3D seismic expression. All fault planes penetrate through the top of the shale layer and extend into the Triassic-Jurassic sandstone layer but do not reach the top surface (i.e. blind faults).

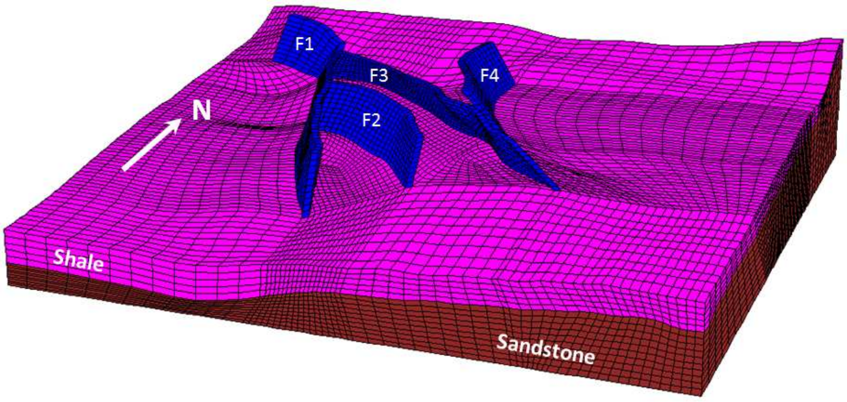

Figure 6: Architecture of the Morangie model without the overburden. Faults (blue) are blind faults and are buried within the top sandstone layer above the shale layer.

2.2.2 MODEL MATERIAL PROPERTIES

The rock mechanical and fluid flow properties that were used in the deformation models are shown in Table 1. These values are selected from the literature or from rock property data for the region. In the models, faults are simulated as narrow zones with lower strength parameters and with permeabilities initially identical to those of host rocks. This represents a continuum approach for the simulation of faults, which has been adopted in a number of previous studies (e.g. McLellan et al., 2004, Zhang et al. 2009). A limitation of the continuum approach, by comparison with the discrete approach (i.e. faults are simulated as discrete fault planes), is its difficulty to achieve large fault movement. However, this study only deals with a relatively small amount of regional deformation. Fluid flow properties and boundary conditions (e.g. fluid pore pressures) are incorporated in the model, so that the mechanical deformation of faults and host rocks are coupled with fluid flow behaviours. However, this study focuses on the geomechanical behaviour of the system and reactivation of faults.

Table 1: Initial properties of the Cliff Head Dunsborough/Lilac and Morangie numerical models.

MODEL UNIT	DENSITY (kg m^{-3})	YOUNG'S MODULUS (Pa)	POISSON'S RATIO	COHESION (Pa)	TENSILE STRENGTH (Pa)	PERMEABILITY (m^{2})	POROSITY	DILATION ANGLE (°)	FRICTION ANGLE (°)
Tri-Jur sandstone	2500	2.5x10^{10}	0.25	1. 5x10^{7}	7. 5x10^{6}	1.5x10^{-13}	0.2	2	30
E. Triassic shales	2250	2.0x10^{9}	0.35	2.75x10^{6}	1.38x10^{6}	1.0x10^{-17}	0.3	2	22
Palaeozoic sandstone	2500	2.5x10^{10}	0.25	1. 5x10^{7}	7. 5x10^{6}	1.5x10^{-13}	0.2	2	30
Basement*	2650	4.0x10^{10}	0.22	2. 0x10^{7}	1x10^{7}	1.0x10^{-16}	0.04	2	30
Faults	2300	1.0x10^{9}	0.15	1.0x10^{6}	0.5x10^{6}	Various	0.2	3	15

* Basement is only present in the Cliff-Head model.

2.2.3 BOUNDARY CONDITIONS

Based on the interpretation of tectonic settings for the region during the Mesozoic (Harris, 1994 and Mory and Iasky, 1996) the current models are subjected to NW-SE (310-130) extension. The deformation boundary condition for such an extensional direction is implemented in the model by partitioning a uniform NW-SE extensional velocity field onto the modelled space, fixing velocities only for the vertical boundary edges of the model and leaving the internal areas of the model free for deformation velocity changes based on local deformation conditions. The model top is simulated as a free surface. The model bottom boundary is fixed in the vertical direction, but free to move in the horizontal directions. Because the Mohr-Coulomb elastic-plastic constitutive rheology (i.e. rate independent) is adopted here to simulate mechanical deformation, the extensional deformation of the current model does not involve an extensional strain rate.

Fluid pore pressures are also specified in the model. A hydrostatic fluid pore pressure is initially defined for the sandstone layer above the shale unit. For the shale and sandstone layers below this, an initially higher fluid pressure gradient (approximately 15% above the hydrostatic gradient) was adopted. Fluid pore pressures are only fixed at initial values at the top free surface of the model.

3 Cliff Head Oilfield

The Cliff Head structure is a large faulted anticline at top Permian reservoir, sealed by the overlying Triassic Kockatea Shale (Figure 7). The closure is located on a narrow NW-SE oriented horst bounded by a conjugate pair of sub-parallel faults (Jones and Hall, 2002, Main Horst in Figure 7). The structure is part of a larger NNE-SSW trending rotated block created in the early Permian and is bound to the west by the Geraldton Fault, which has acted as a significant hinge zone across which the Mesozoic section thickens westward into the Abrolhos Sub-basin. Post-Permian tectonic episodes have resulted in complex faulting, reactivating both the NNE-SSW and NW-SE oriented fault sets developed in the Early Permian and creating additional faulting, particularly in a NW-SE direction. Over the Cliff Head structure the reactivated Permian faults and newly formed Middle Jurassic to Early Cretaceous faults formed soft linkage that might interact within the Kockatea top seal. The post-Permian reactivation has resulted in compartmentalization of the western Beagle Ridge into a series of discrete structures of which Cliff Head is one (Jones and Hall, 2002).

A 31-33 °API oil is reservoired in the Permian Dongara Sandstone, Irwin River Coal Measures and High Cliff Sandstone, with a field-wide oil-water contact (OWC) at 1260 mTVDSS (Roc Oil (WA) Pty Ltd, 2003).

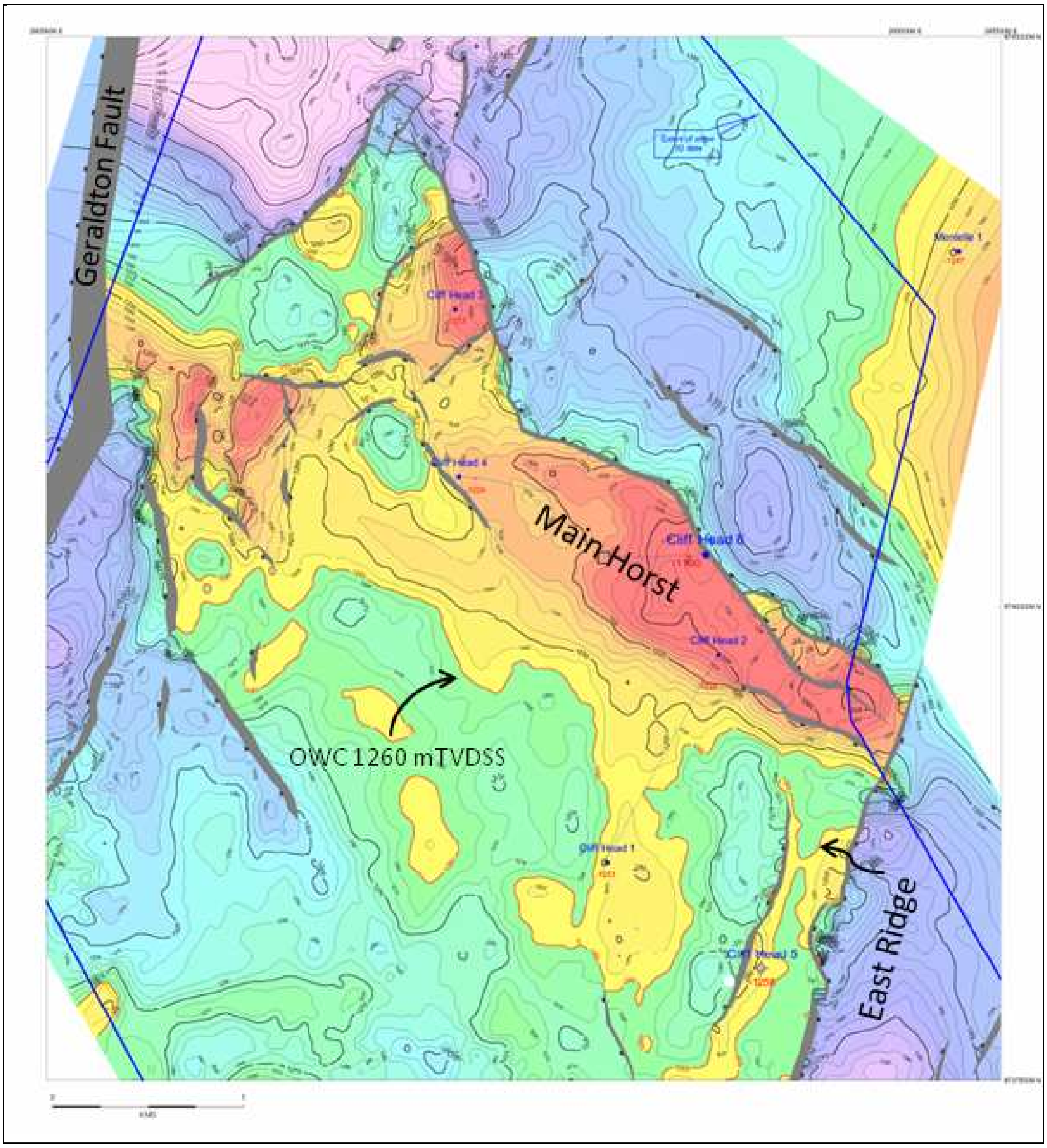

Figure 7: Post-drill Cliff Head-6 depth map of the Cliff Head structure (top Permian reservoir) and oil-water contact (OWC) (modified from Roc Oil, 2005). Location of Main Horst and East Ridge are indicated (Roc Oil terminology). The west-dipping Geraldton Fault is shown. Blue box is the 3D seismic location.

3.1 Geomechanical fault seal prediction - Cliff Head

The stress fields used in the modelling of the stress regime on the fault planes are described in section 2.1.5.

Regional subsidence curves suggest that up to 1000 m of Yarragadee Formation was eroded during the Valanginian breakup (Mory and Iasky, 1996) and the models here are based on fault seal attributes that relate to an extensional stress regime (Sv>SHmax>Shmin) associated with an extra 1000 m of overburden. This additional rock column does not affect the stress gradients described in section 2.1.5 (Sv=0.0235 MPa/m; SHmax=0.018 MPa/m and

Shmin=0.016 MPa/m). However, it does result in an increase in the stress values at the Permian reservoir level before the erosion occurs (i.e. 2275 m below palaeo-elevation) with Shmin=32 MPa, SHmax=36 MPa and Sv=44 MPa.

Rock and fault rock properties of the model are described in section 2.1.6.

The main Permian trap-bounding faults used for the geomechanical fault seal prediction were interpreted from 3D seismic data and their configurations delimit the main NW-SE (i.e. Main Horst) and NNE-SSW (i.e. East Ridge) oriented compartments (Figure 7).

Figure 8 shows the configuration of the Permian faults used for the geomechanical fault seal prediction.

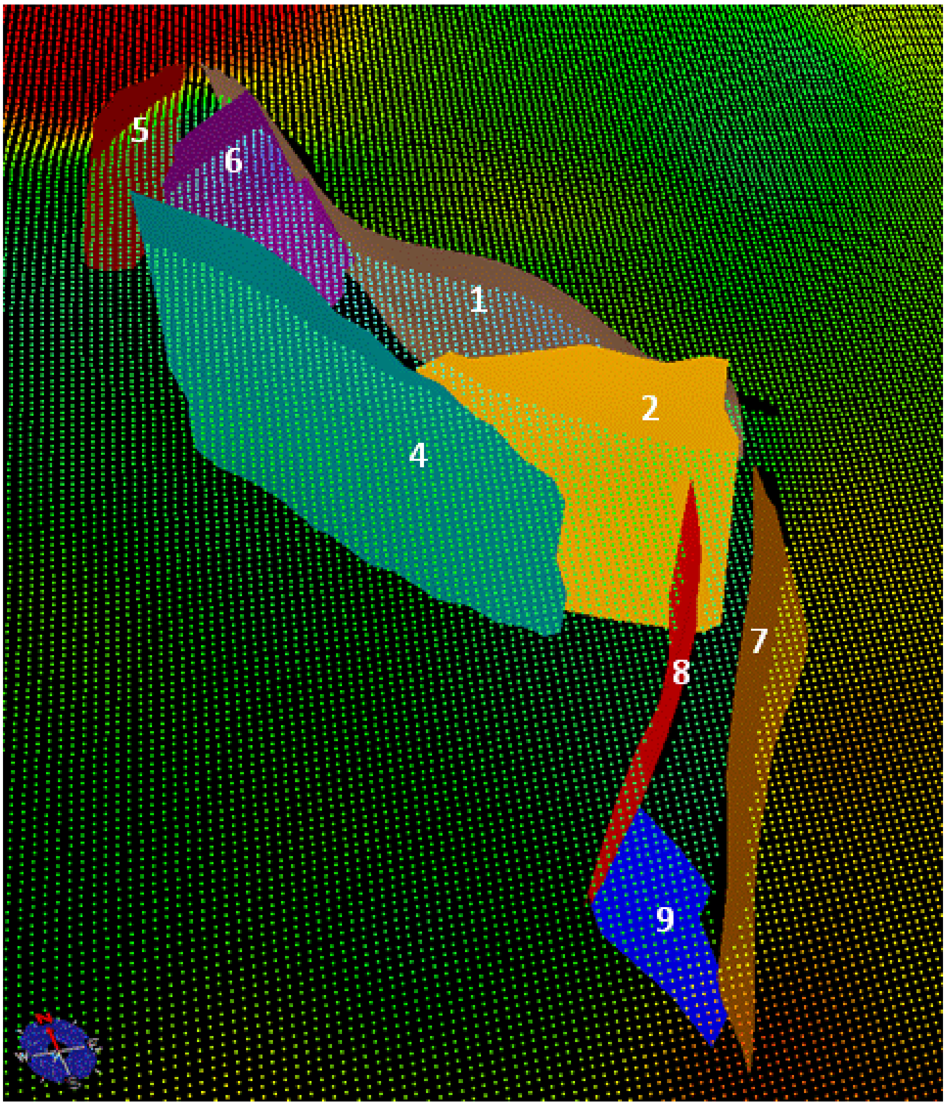

Figure 8: Permian faults for the geomechanical fault seal prediction and top reservoir structure.

3.1.1 FRACTURE STABILITY

Figure 9 displays the state of stress on the Permian faults at 2275m below the ground elevation (chosen as the approximate depth of the top Permian reservoir before erosion). In the modelled stress regime for Cliff Head there is an average-high likelihood of fault shear failure for faults oriented in the N and NNE direction and a low likelihood of fault shear failure for faults oriented in the NW direction. Using a cohesive strength of 1 MPa and an internal coefficient of friction of 0.3 (i.e. case for low rock strength and low internal coefficient of friction favouring failure, Figure 9A), the fluid pressure would need to be approximately 20-30% higher than the estimated pore pressure to induce failure on the N and NNE oriented faults. That is, it would need an increase of at least 5 MPa on the best oriented fault planes (e.g. fault 8). The Geraldton Fault is the best oriented fault plane for reactivation under this stress regime. By comparison, the NW oriented faults of the Main Horst would require a 30-60% increase in the fluid pressure to induce failure. On fault 1, which delimits the northern extent of the current hydrocarbon column, it would need an increase of at least 14 MPa. Using a cohesive strength of 5 MPa and an internal coefficient of friction of 0.6 (i.e. the case for higher rock strength and higher internal coefficient of friction hindering failure, Figure 9B), the fluid pressure would need to be approximately 55-70% higher to induce failure on the N and NNE oriented faults. That is, it would need an increase of at least 13 MPa on the best oriented fault planes (e.g. fault 8). The Geraldton Fault is still the best oriented fault plane for reactivation under this stress regime. The NW oriented faults would require an 80-90% increase in the fluid pressure to induce failure. On fault 1, it would need an increase of at least 18-20 MPa to induce failure, which again is significantly greater than the N and NNE faults under these conditions hindering failure.

Figure 10 shows the 3D fracture stability distribution (cohesive strength of 1 MPa and an internal coefficient of friction of 0.3). The fault plane orientation is the primary factor controlling the failure potential with planes sub-parallel to SHmax most likely to fail due to an increase of pore pressure.

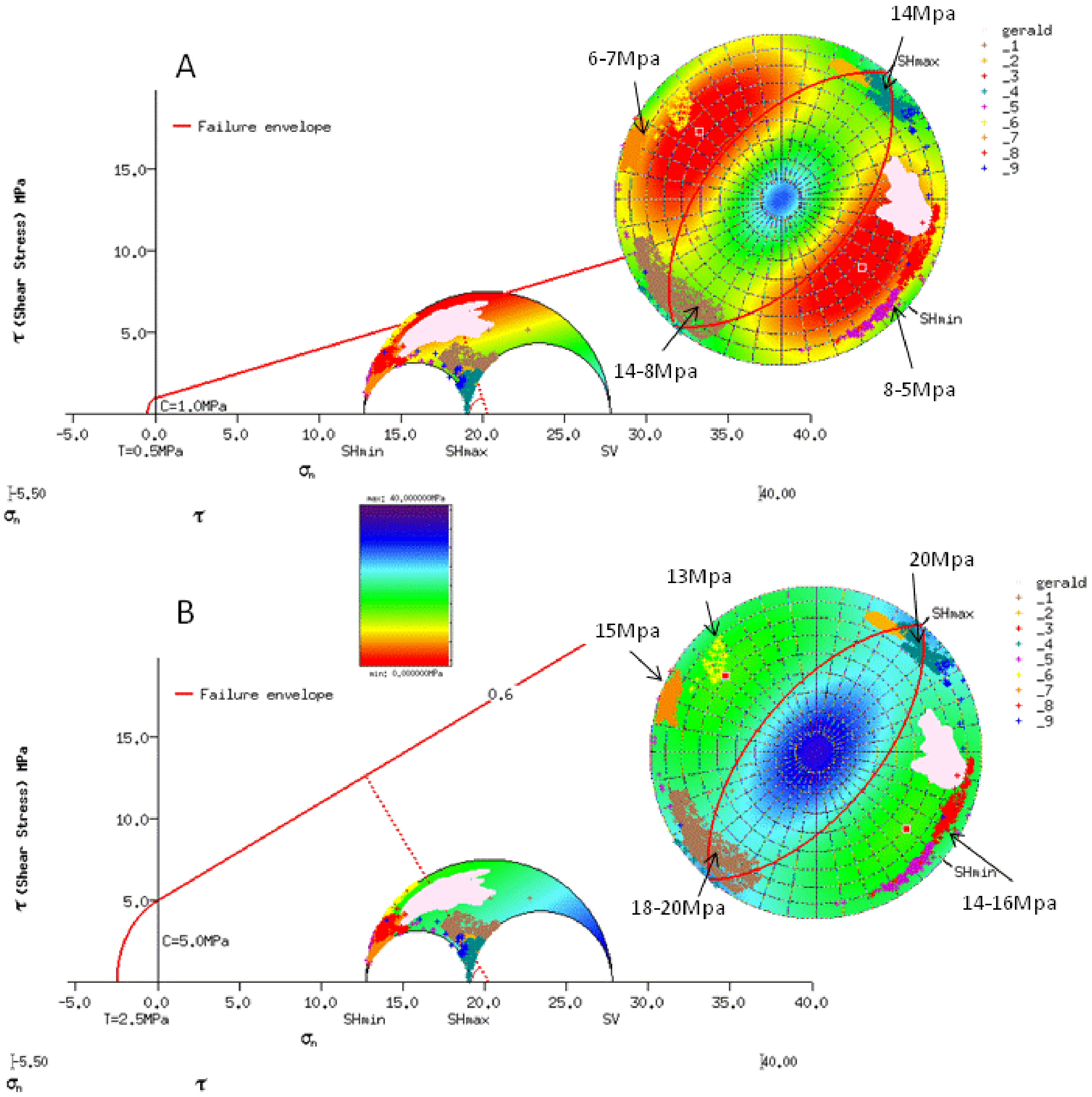

Figure 9: Fracture stability for the Permian faults at 2275 m below elevation (including 1000m of eroded sediments; chosen as the approximate depth of the top Permian reservoir before erosion). The values on the stereonets (right) refer to the increase in pore pressure required to force the plane into failure; the same values are shown on the Mohr circle (left) with the failure envelope (red) defined by the fault rock properties. (A) Cohesive strength of 1 MPa and coefficient of internal friction of 0.3. (B) Cohesive strength of 5 MPa and coefficient of internal friction of 0.6.

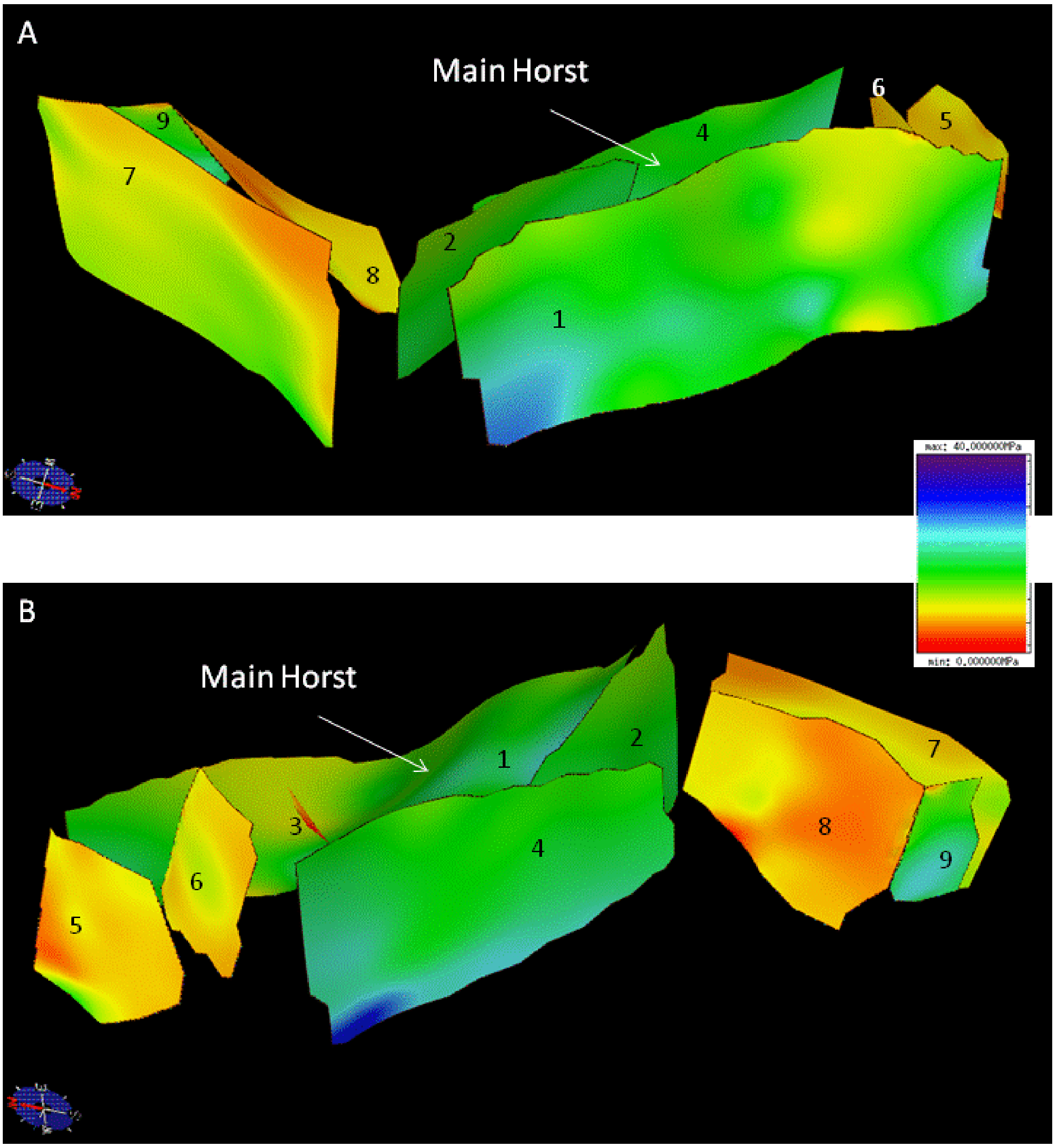

Figure 10: Fracture stability distribution (cohesive strength of 1 MPa and an internal coefficient of friction of 0.3). Maximum fracture stability is blue and minimum fracture stability in red. (A) View from the east showing the higher stability of fault 1 and the low stability of faults 7 and 8. (B) View from the west showing the low stability for the faults oriented to the NNE, i.e. faults 5, 6, 7 and 8.

3.1.2 SLIP STABILITY

Figure 11 show the slip stability for the Permian faults assuming 1000 m of post-Valanginian erosion. As with the fracture stability cases the slip stability shows that there is an average-high likelihood of fault shear failure for faults oriented to the N and NNE and a low likelihood of fault shear failure for faults oriented to the NW. With a coefficient of internal friction of 0.48 the NW oriented faults would require a 60% increase in the fluid pressure to induce failure. That is, it would need an increase of at least 14 MPa on fault 1, which delimits the northern limit of the current hydrocarbon column. By comparison, the fluid pressure would need to be approximately 35% higher than the estimated pore pressure to induce failure on the N and NNE oriented faults, equating to an increase of at least 7 MPa on the best oriented fault planes (fault 8). The Geraldton Fault is again the best oriented fault for failure to occur.

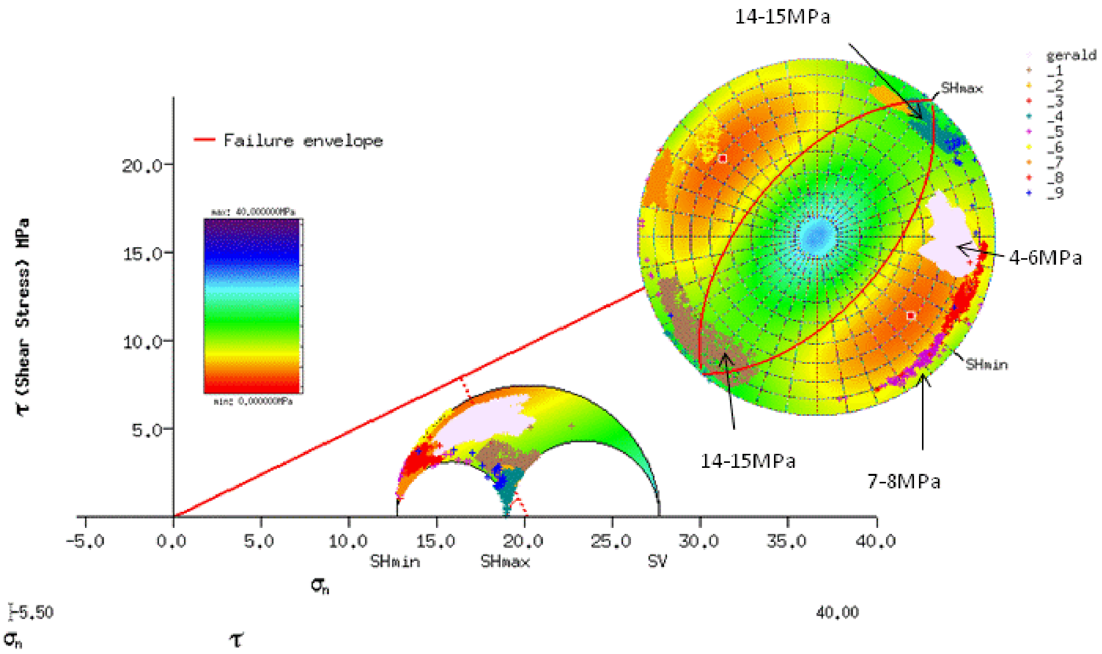

Figure 11: Slip stability for the Permian faults at 2275 m below elevation (including 1000m of eroded sediments). Faults are cohesionless and coefficient of internal friction is 0.486. The values on the stereonets refer to the increase in pore pressure required to force the plane into failure. The values on the stereonets (right) refer to the increase in pore pressure required to force the plane into failure; the same values are shown on the Mohr circle (left) with the failure envelop (red) defined by the fault properties.

3.1.3 SLIP TENDENCY

Figure 12 and Figure 13 show the slip tendency for the Permian faults assuming 1000 m of post-Valanginian erosion. Like the fracture/slip stability, the most significant part of this analysis is that the slip tendency is orientation dependent, with the higher tendency values coinciding with NNE oriented faults.

The NNE oriented faults are characterised by slip tendency values greater than 0.25 and the comparison with the NW faults shows that they are more likely to leak, as they are near the ideal orientation for slip to occur, and are therefore most likely to be associated with enhanced permeability (Figure 12). The large Geraldton Fault is again the most likely structure to slip and accommodate reactivation strain in the study area (Figure 12). Despite their strike orientation sub-parallel to SHmax, several parts of NNE faults show only average slip tendency due to their dip being greater than 80°. This element is, however, subject to errors as interpretation and depth conversion can strongly influence this parameter.

The NW faults, which are orientated sub-parallel to Shmin and have dip being greater than 70°, are characterised by a low slip tendency (<0.1).

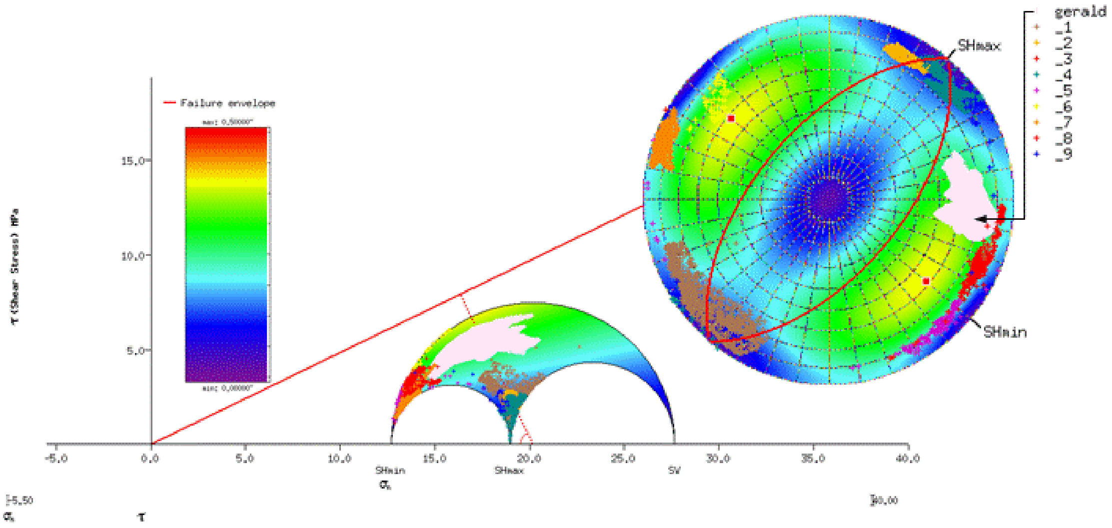

Figure 12: Slip tendency for the Permian faults at 2275 m below elevation (including 1000 m of eroded sediments). The values on the stereonets (right) refer to the likelihood of slip to occur; the same values are shown on the Mohr circle (left).

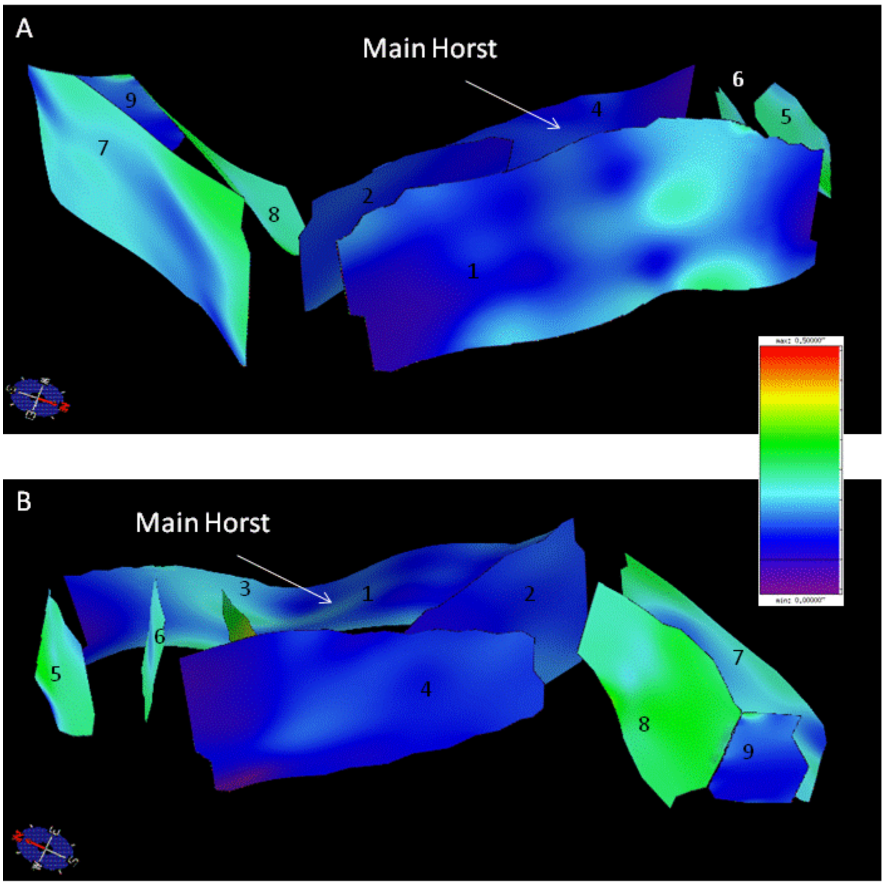

Figure 13: Slip tendency distribution. (A) View from the east showing the higher tendency of NNE oriented faults and the low tendency of NW oriented faults. Maximum slip tendency is red and minimum slip tendency is blue. (B) View from the west showing the variation in slip tendency on the NNE oriented fault 7 and the NW oriented fault 1.

3.1.4 DILATION TENDENCY

Figure 14 and Figure 15 show the dilation tendency for the Permian faults assuming 1000 m of post-Valanginian erosion. Like the slip tendency, the most significant part of this analysis is that the dilation tendency is orientation dependent with the higher tendency values coinciding with steeply dipping NE oriented fault surfaces.

The model predicts that all faults have a likelihood above 0.5 to dilate. The NW oriented faults of the Main Horst show values between 0.5 and 0.6 while the NNE oriented faults have generally higher values, usually above 0.8. As the ability of fractures to transmit fluid is also related to their aperture, risk of leakage is usually associated with high dilation tendency. However recent work on the Gippsland Basin (Ciftci et al., 2012) shows a poor match of high dilation tendency to leakage indicators, suggesting that it may not always be a good parameter with which to assess along-fault leakage risk.

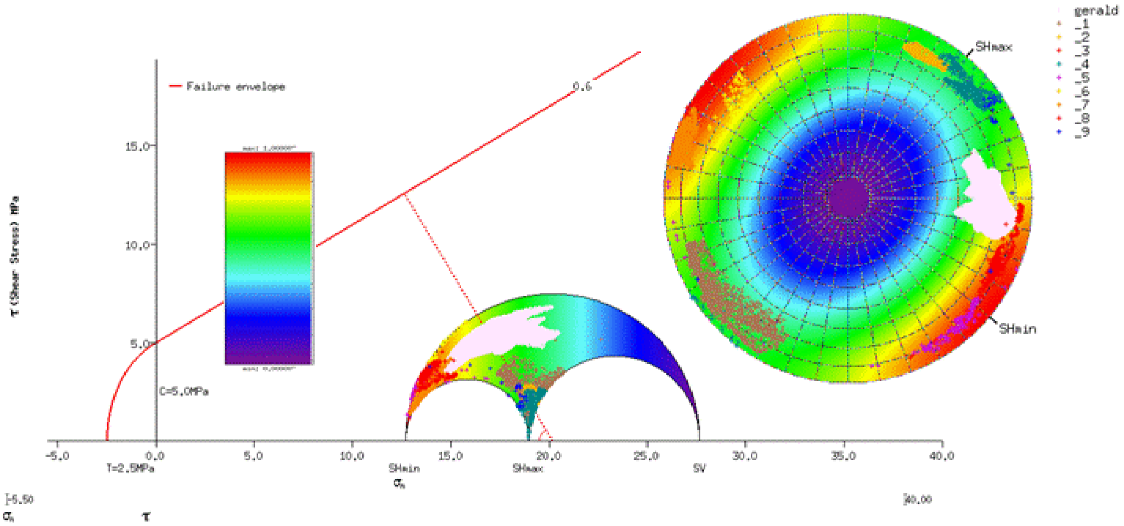

Figure 14: Dilation tendency for the Permian faults at 2275 m below elevation (including 1000 m of eroded sediments). The values on the stereonets (right) refer to the likelihood of dilation to occur; the same values are shown on the Mohr circle (left).

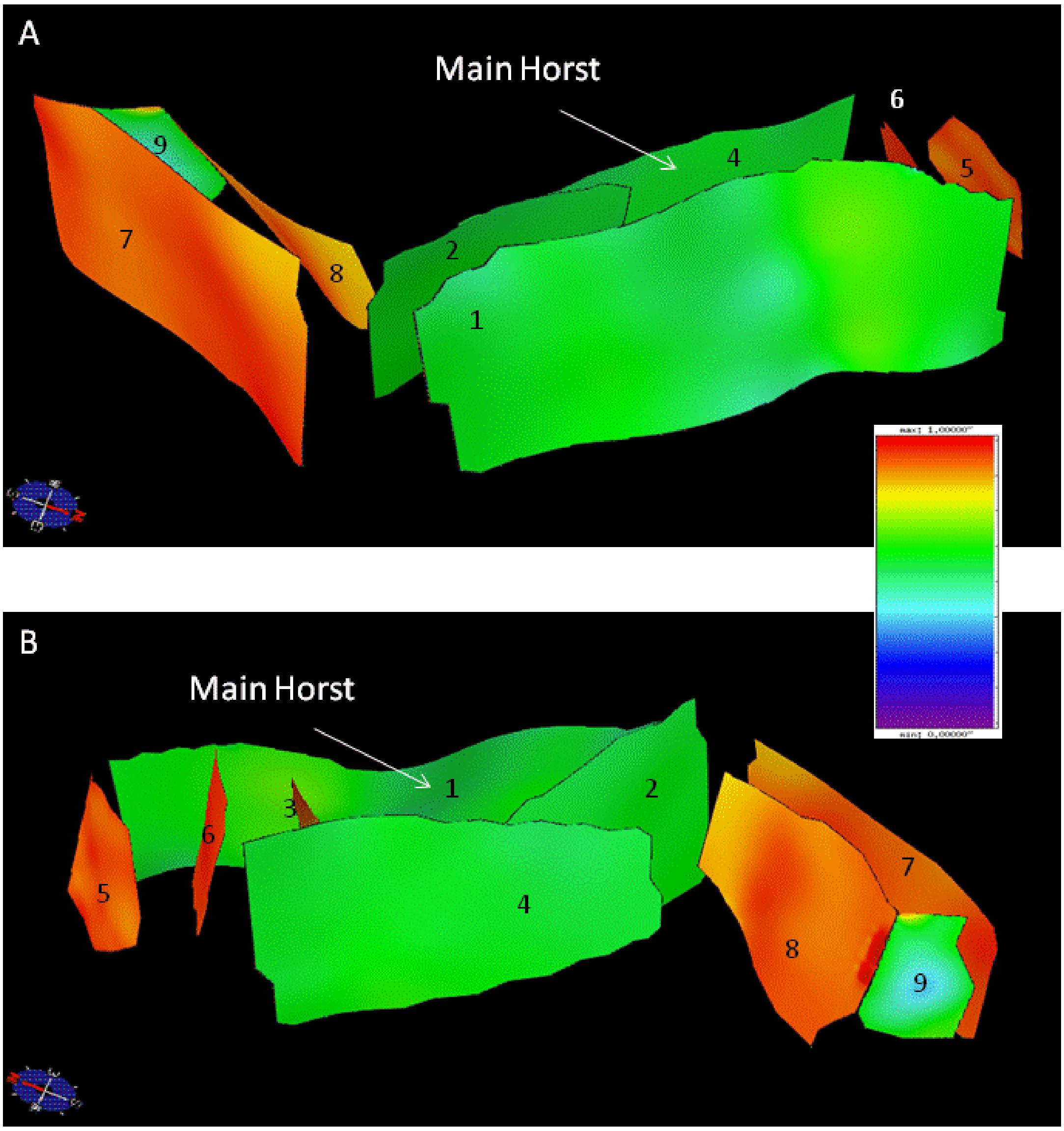

Figure 15: Dilation tendency distribution. Maximum dilation tendency is red and minimum dilation tendency is blue. (A) View from the east showing the higher tendency of NNE oriented faults and the low tendency of NW oriented faults. (B) View from the west.

3.2 Geomechanical deformation modelling – Cliff Head

The Cliff Head deformation model architecture, material properties and boundary conditions are described in sections 2.2.1, 2.2.2 and 2.2.3 respectively.

Due to the transparent seismic character of the Kockatea Shale, the fault interpretation within the top seal layer remains locally ambiguous. Three structural scenarios have been tested in order to investigate the impact of Mesozoic reactivation (Figure 16). These scenarios are based on an essentially similar overall structural interpretation, with differing distribution of the up- and down-dip fault tips:

- Scenario 1: the tips of the Permian and Mesozoic faults stop at the base and top of the modelled shale layer respectively.
- Scenario 2: the tips of the Permian faults intersect the modelled shale layer and propagate halfway through, while the tips of the Mesozoic faults stop at the top of the modelled shale layer.
- Scenario 3: the tips of the Permian faults intersect the modelled shale layer and stop at the top of the shale layer, while the tips of the Mesozoic faults stop at the top of the modelled shale layer.

There was no significant difference in the results of three modeled structural scenarios. This may be due to the identical fault-strike lengths in the three scenarios, with only a small difference in the depth levels of the fault tips. Scenario 1, with the shale layer unaffected by faults, is described herein as it enables it removes the ambiguity of fault interpretation in the top seal and helps to visualize potential linkage processes that may have occurred in the top seal both during and after deformation.

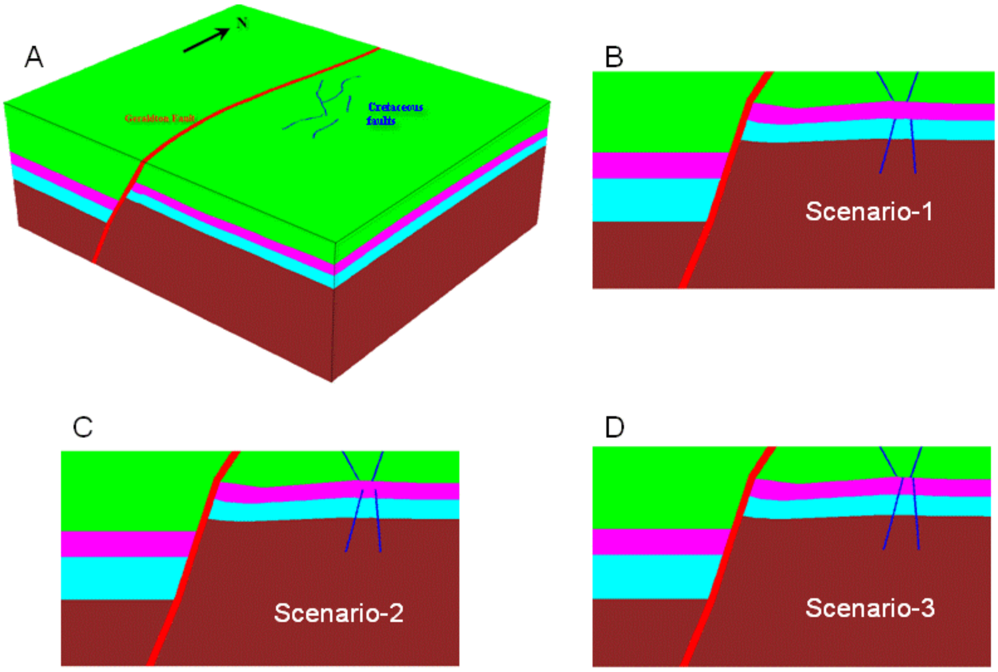

Figure 16: Structural scenarios used in the deformation modelling of the Cliff Head Field. (A) Model overview with mechanical layers, brown=basement, blue=sandstone/reservoir, purple=shale/top seal, green=sandstone/overburden. (B) Scenario 1. (C) Scenario 2. (D) Scenario 3.

3.2.1 STRAIN DISTRIBUTION

The modelling shows that fault size and orientation primarily influence the partitioning of reactivation shear and volumetric strains (Figure 18, Figure 19, Figure 20 and Figure 21). The Geraldton Fault accommodates most of the bulk strain, protecting all the smaller Permian and Mesozoic faults.

Among smaller Permian and Mesozoic faults, the strike orientation of the faults is the key factor governing strain partitioning. The NNE oriented fault planes (e.g. faults 7 and 8; Figure 19 and Figure 21) accommodate more shear and volumetric strain. This suggests they have a higher structural permeability risk and a higher risk of dip-linkage between Permian and Mesozoic faults. In latter case, high shear strain occurs at the ends of, and between, faults 8 and 15 which shows the potential for linkage and development of top seal bypass (Figure 18B).

Significantly, the NW oriented faults, which bound the Main Horst, are the least strain-accommodating structures (Figure 19). Small amounts of lateral variability in shear strain distribution are observed on the NW oriented faults, with higher strain focused near the tips of faults 1 and 2 (Figure 19B).

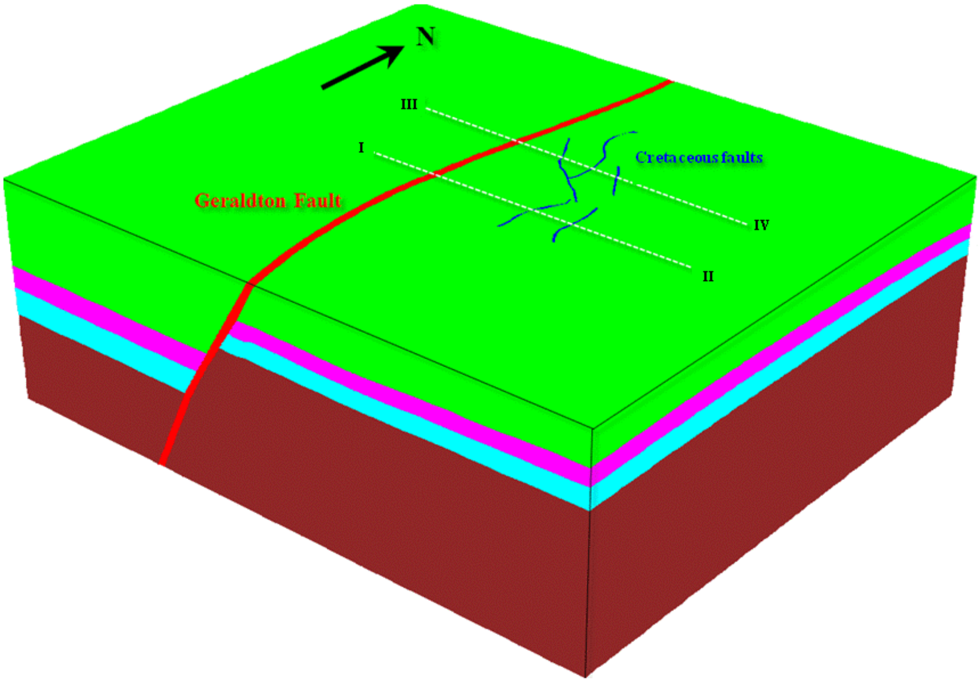

Figure 17: Location of cross-sections over the Cliff Head Field displayed in Figure 18 and Figure 20. I-II intersects the East Ridge and III-IV intersects the Main Horst.

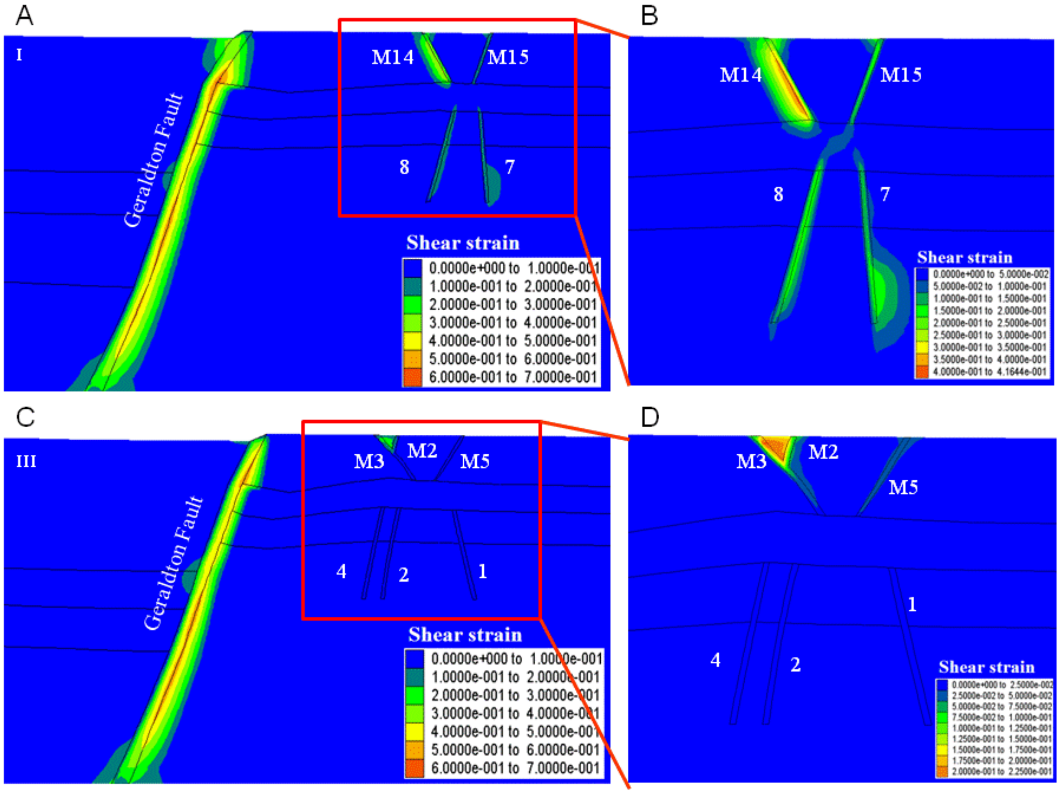

Figure 18: Shear strain distribution in section for structural scenario 1. The lower faults are the reactivated Permian reservoir faults and the upper faults are the Mesozoic faults. Maximum strain is red and minimum strain is blue. (A) Shear strain distribution for the East Ridge. (B) Detail shear strain distribution for the East Ridge. (C) Shear strain distribution for the Main Horst. (D). Detail shear strain distribution for the Main Horst

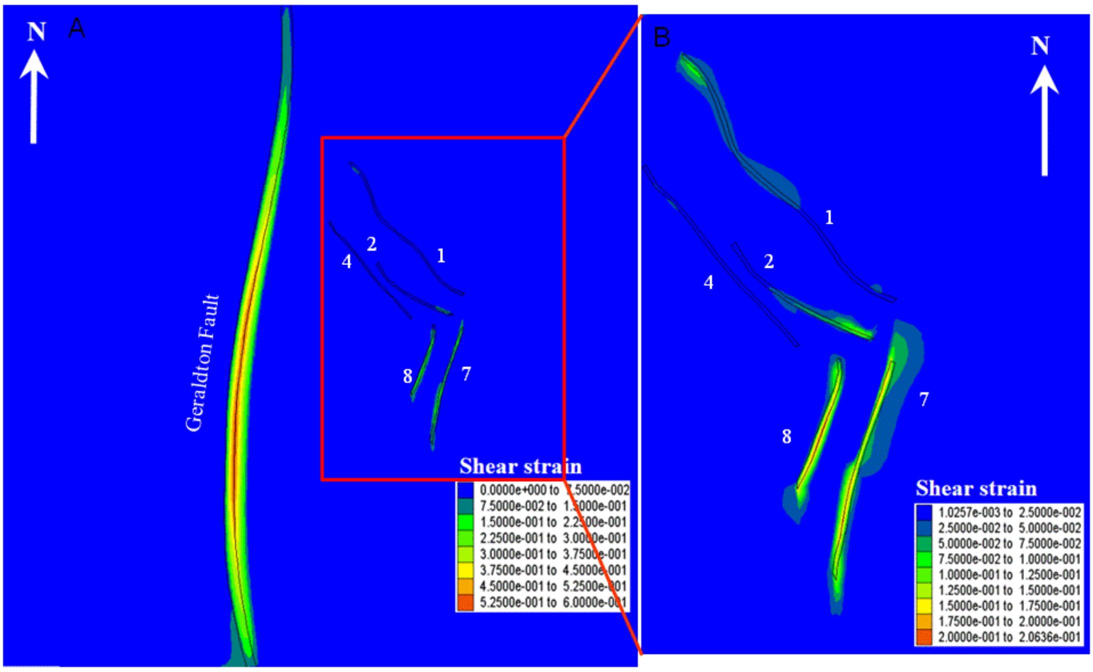

Figure 19: Shear strain distribution in plan view (intra reservoir horizon). Maximum strain is red and minimum strain is blue. (A) Shear strain distribution of the main Permian faults for the Cliff Head Field and the regional Geraldton Fault. (B) Detail shear strain distribution of the main Permian faults for the Cliff Head Field

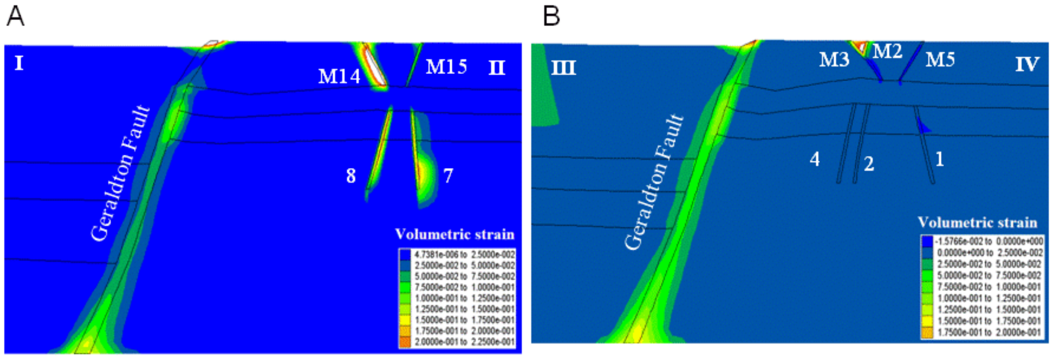

Figure 20: Volumetric strain distribution in section for structural scenario 1. The lower faults are the reactivated Permian reservoir faults and the upper faults are the Mesozoic faults. Maximum strain is red and minimum strain is blue. (A) Volumetric strain distribution for the East Ridge. (B) Volumetric strain distribution for the Main Horst.

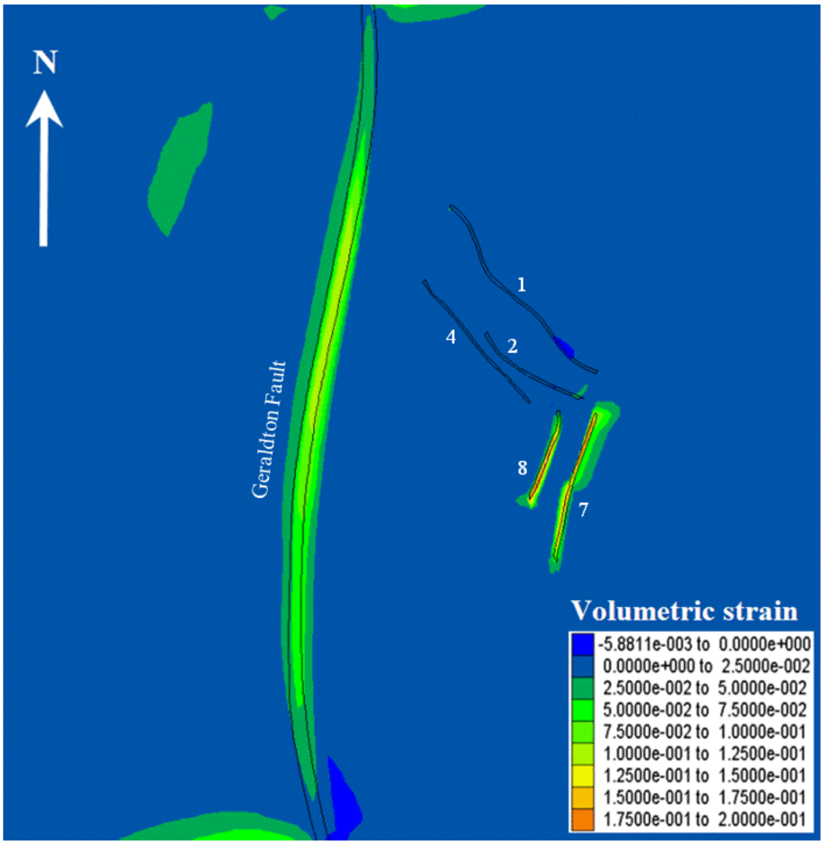

Figure 21: Volumetric strain distribution in plan view for the Cliff Head Field (intra reservoir horizon). Maximum strain is red and minimum strain is blue.

The evolution of shear strain with bulk extension (Figure 22) shows that the model predicts that the late Mesozoic faults accommodate more strain than the Permian trap bounding faults. This suggests that main risk for trap integrity in such structures that formed during distinct Permian and Jurassic-Cretaceous tectonic phases comes from the Jurassic-Cretaceous faults propagating downward and interacting with the top seal, that is potentially creating migration pathways.

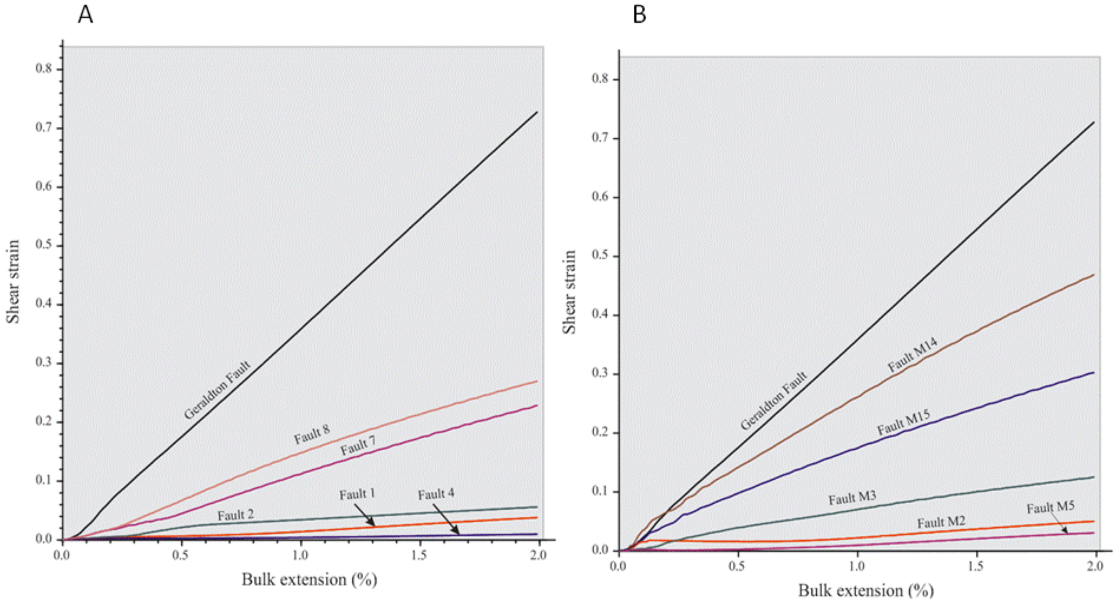

Figure 22: Shear strain vs. bulk extension. (A) Reactivated Permian trap-bounding faults. (B) Mesozoic faults.

3.2.2 STRESS DISTRIBUTION

Patterns of mean and shear stresses for a horizon within the reservoir rocks in the model for the Cliff Head field illustrate the post-failure stresses in a field during fault reactivation (Figure 23). The whole stress field is dominated by both lower mean and shear stresses within faults, in comparison with host rock domain. Faults with greater reactivation (Figure 22A; Geraldton Fault, 7 and 8 faults), which show greater shear strain and volumetric strains compared to other faults (Figure 18 to Figure 21), also display relatively lower stresses than other faults. This suggests an important stress release following fault failure. Areas near fault tips or areas between adjacent fault tips show higher shear stresses than the main segments of faults (Figure 23B). This implies the potential of fault growth toward higher shear stress locations. Asymmetric stress patterns around the P7 and P8 faults (i.e. the most reactivated faults within the population) are also consistent with the features expected for faulting with a strike-slip component.

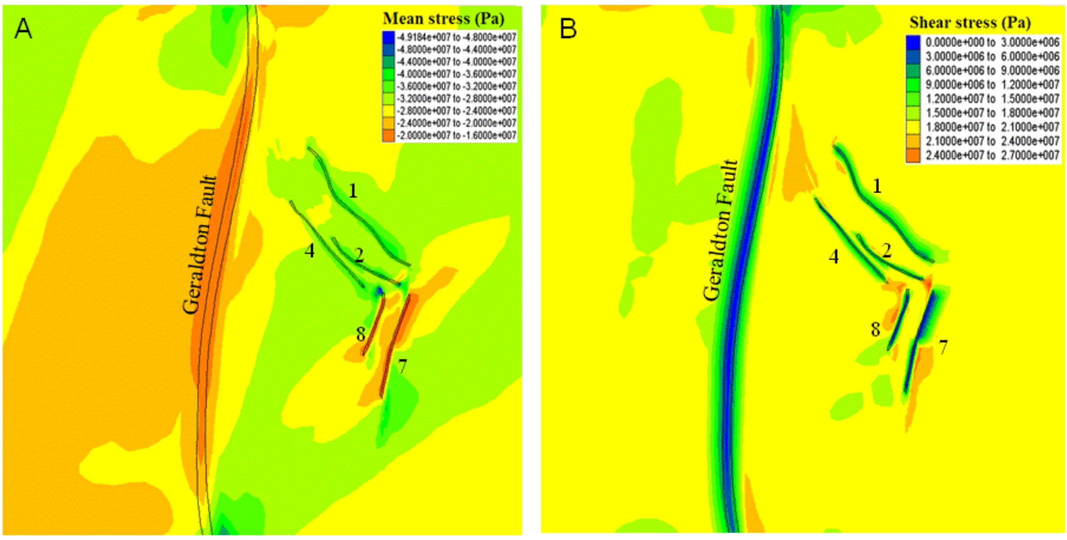

Figure 23: Plan-view stress patterns for a horizon within the reservoir rock in the model for the Cliff Head Field. (A) Mean stress. Values are all negative which indicate compressive stresses. (B) Shear stress.

3.3 Discussion - Cliff Head

The bulk of the oil in the Cliff Head field is trapped within the NW trending Main Horst above a field-wide OWC at 1260 mTVDSS (Figure 7and Figure 24). The Permian fault 1 is the most critical to this structure, as it bounds the crest of the closure to the north-east, and, like other similar NW-oriented faults, is consistently associated with a low risk of reactivation (Figure 24). Fault strike orientations to the NW are sub-parallel to the minimum Middle Jurassic to Early Cretaceous horizontal stress (Shmin) and this is likely the main factor preventing; (i) reactivation of the trap bounding fault, (ii) hard linkage with the overlying Mesozoic fault system and, (iii) the development of seal bypass. Geomechanical fault seal models consistently associate this NW orientation with high fracture and slip stabilities and low slip and dilation tendencies. Geomechanical deformation models show that, although some lateral variability of shear strain distribution occurs for the NW trend (i.e. locally at fault tips), the trap bounding faults typically accommodate low shear and volumetric strains.

The geomechanical deformation models also predict that the large Geraldton Fault accommodated most of the reactivation strain due to its orientation to the NNE and its size. This suggests that the overall Cliff Head structure (Main Horst and East Ridge) is partially *protected* by the large Geraldton Fault (Figure 25). The typical soft-linkage and/or disconnection between the Permian reservoir faults and the overlying Mesozoic fault systems is likely to be attributed to a locally reduced accommodation of strain. Shear strain values <0.025 and <0.05 are associated with the disconnected Permian and Mesozoic faults forming the Main Horst.

Figure 26 shows throw maxima on both the Permian and the Mesozoic faults. Throw maxima on the Permian faults are located near the top of the fault surface and represent the Late Palaeozoic fault movement; the throws rapidly decrease upwards as the surfaces die in the top seal. The Mesozoic fault planes above the Main Horst show well developed maxima near the top of the fault planes that decrease toward the base of their planes. This suggests fault nucleation at the top (in the Yarragadee and/or Cadda Formations; Figure 2) and a downward propagation of the fault. The rapidly decreasing throw that dies in the vicinity of the top seal (e.g. fault M4 on Figure 26) suggests that the reactivation strain is limited on the Mesozoic faults, which in turn limits its growth and its impact on the top seal. By comparison, the Mesozoic fault planes above the East Ridge show throw maxima that extend from the top to the base of the fault plane (e.g. fault M7 on Figure 26). This suggests that the reactivation strain is likely to be more pronounced on such NNE trending structures, which in turn would facilitate the downward propagation of the Mesozoic fault and linkage with the underlying Permian reservoir faults.

In summary the outcomes from the *geomechanical deformation* (section 3.1) and the *geomechanical fault seal prediction* (section 3.2) models suggest that the preservation of the hydrocarbons in the Main Horst of the Cliff Head oilfield is due to: (i) a favourable orientation of the NW-trending bounding faults being less prone to failure from the Middle Jurassic to Early Cretaceous stress regime and, (ii) the presence of the large N-trending Geraldton Fault that accommodates a large part of the reactivation strain and shields the overall Cliff Head structure.

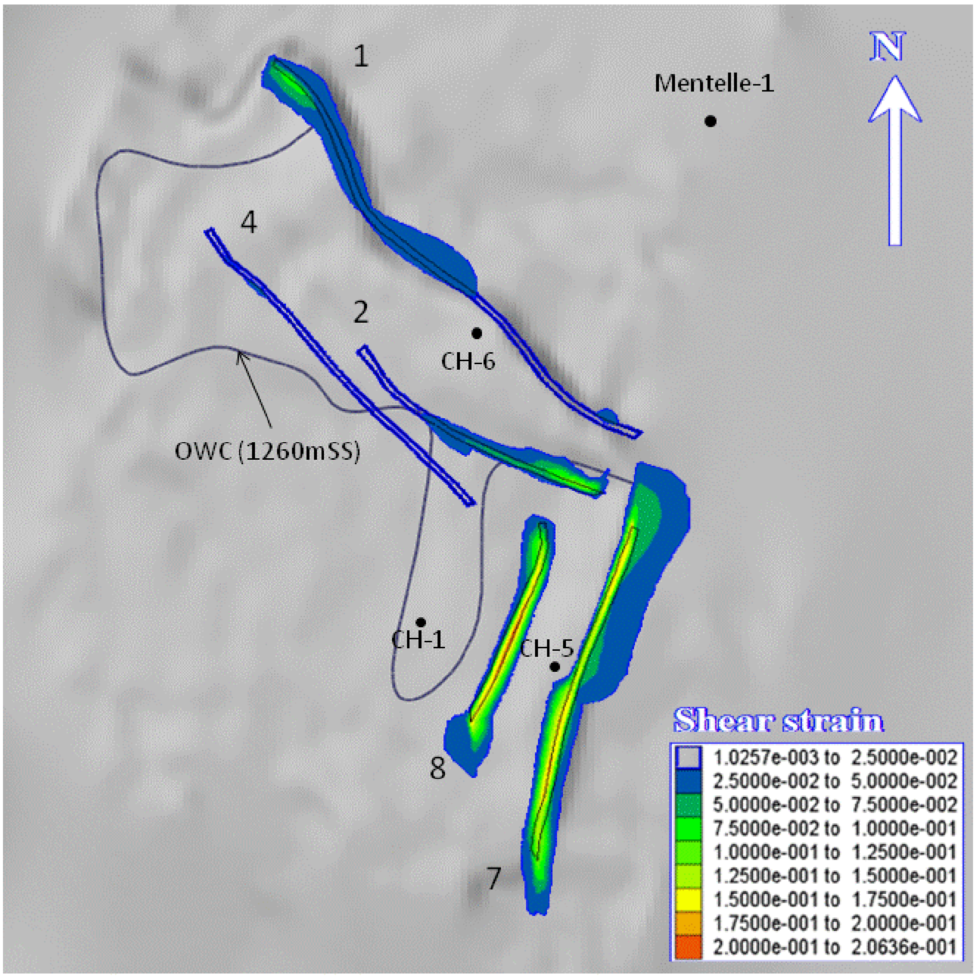

Figure 24: Current oil-water contact (OWC) superimposed on Permian fault shear strain distribution for the Cliff Head Field. Maximum strain is red and minimum strain is blue.

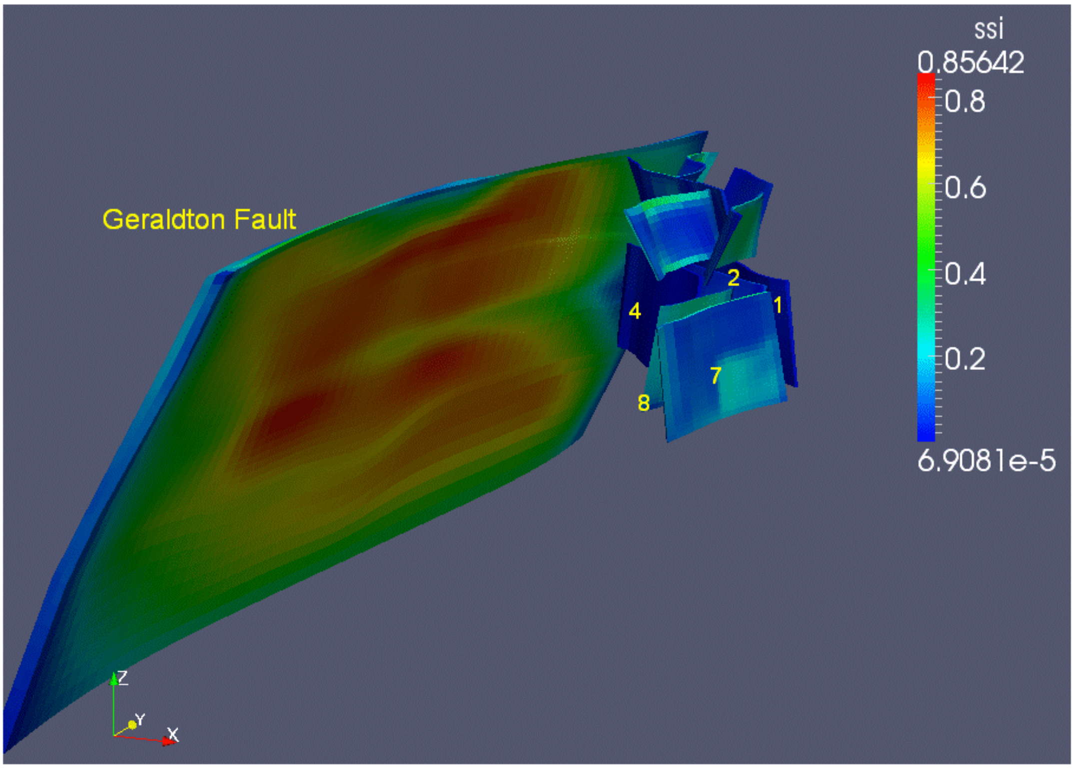

Figure 25: 3D shear strain distribution showing the shielding effect of the Geraldton Fault on the Cliff Head Field. The Y direction refers to the north, the X direction refers to the east. Maximum strain is red and minimum strain is blue.

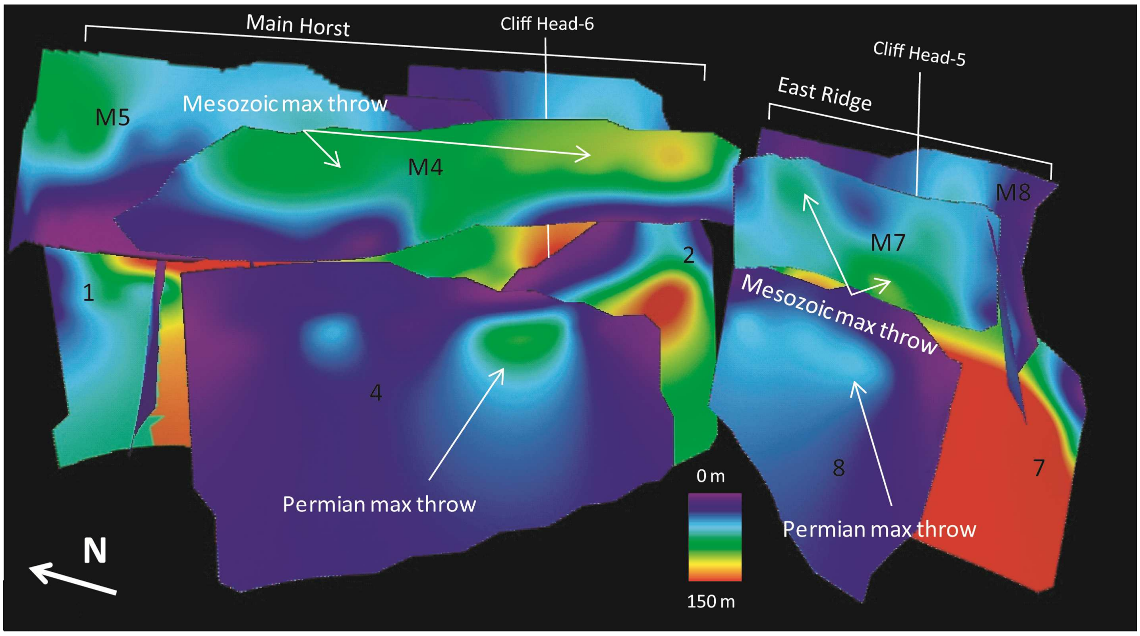

Figure 26: Throw distribution on the Permian and Mesozoic faults for the Cliff Head structure.

4 Dunsborough Oil/Gas Discovery and Lilac Breached Trap

Dunsborough-1 was drilled by Roc Oil (WA) Pty Limited in June 2007 to test the reservoir quality and hydrocarbon potential of the Dongara Sandstone and Irwin River Coal Measures within a north-south oriented, rotated fault block trap (Figure 27). Numerous oil and gas shows were observed in the lower Kockatea Shale, Dongara Sandstone and Irwin River Coal Measures. Fluorescence was observed from 1425 to 1539 mMD and shows in several SWCs between 1466.2 to 1518.2 mMD. Gas peaks were observed between 1465 and 1640 mMD (Roc Oil , 2008). There were no drill stem or production tests and the well was plugged and abandoned as a new oil and gas discovery.

Dunsborough-2 was drilled in March 2008 by Roc, approximately 1.7 km south of Dunsborough 1. The objective of the well was to appraise the extent of the hydrocarbon column discovered in Dunsborough-1 within the late Permian Dongara Sandstone and underlying Early Permian Irwin River Coal Measures (Roc Oil, 2009a). Dunsborough-2 was designed as a vertical well approximately 105 metres down-structure from Dunsborough-1. Dunsborough-2 was plugged and abandoned, having failed to intersect moveable hydrocarbons.

Lilac-1 was drilled by Roc Oil Ltd in February 2008 to test the reservoir quality and hydrocarbon potential of the Dongara Sandstone and Irwin River Coal Measures within a N-S oriented, rotated fault block trap. The closest well is Dunsborough-1, which is approximately 2.7 km to the west. Hydrocarbon fluorescence was encountered between 1330 and 1455 mMD in the lower Kockatea Shale, Dongara Sandstone and Irwin River Coal Measures (Roc Oil, 2009b). Gas peaks were observed through the same interval. Shows observed in sidewall cores from 1355.4 to 1421.5 mMD, were interpreted as residual non-moveable oil and the well was plugged and abandoned.

The fault displacements observed from seismic data indicate that the reactivated Permian reservoir faults and the Mesozoic faults connect across the top seal and form hard-linkages.

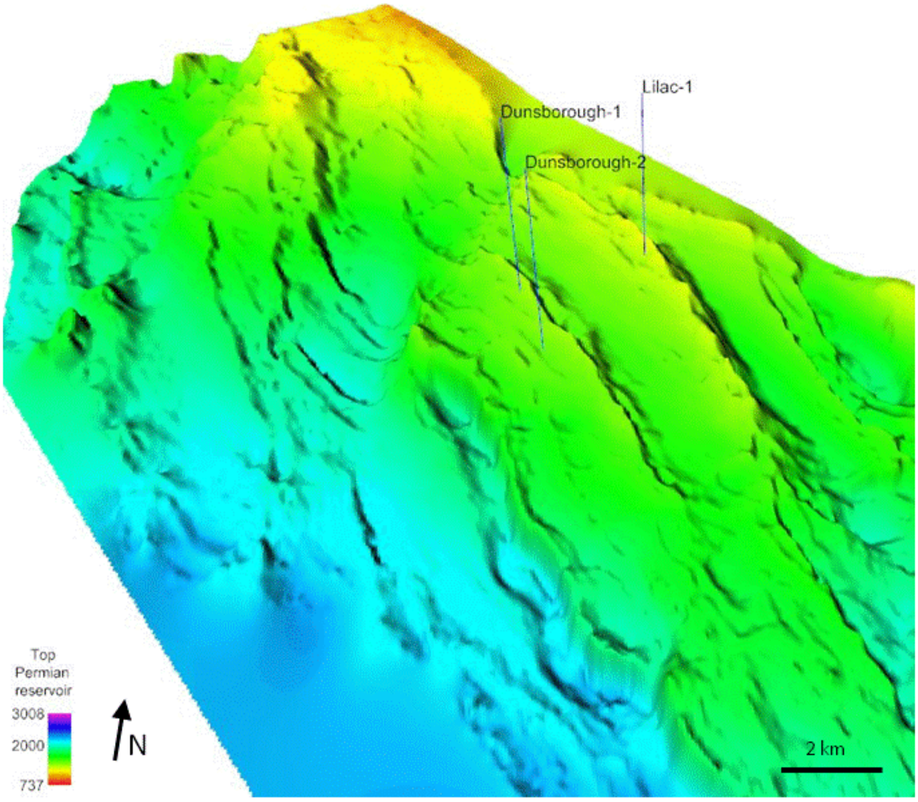

Figure 27: Dunsborough and Lilac structures. Base Kockatea Shale depth converted horizon.

4.1 Geomechanical fault seal prediction – Dunsborough and Lilac

The stress fields used in the modelling of the stress regime on the fault planes are described in section 2.1.5. Regional subsidence curves (Mory and Iasky, 1996) for neighbouring onshore wells (e.g. Casuarinas-1) suggest that up to 2000 m of Yarragadee Formation was eroded during the Valanginian breakup and the models here are based on fault seal attributes that relate to an extensional stress regime (Sv>SHmax>Shmin) associated with an extra 2000 m of overburden. This additional rock column does not affect the stress gradients described in section 2.1.5 (Sv=0.0235 MPa/m; SHmax=0.018 MPa/m and Shmin=0.016 MPa/m). However it does result in an increase in the stress state with Shmin=55 MPa, SHmax=64 MPa and Sv=78 MPa at the Permian reservoir level before the erosion occurs (i.e. 3400 m below palaeo-seabed). Rock and fault rock properties of the model are described in section 2.1.6.

The configuration of the faults used for the geomechanical fault seal prediction is shown in Figure 28. The main trap bounding faults for Dunsborough are fault 1 and fault 2; (i) fault 1 generally trends NNW, bounds the closure to the east and is at the crest of the structure while, (ii) fault 2 trends NNW, bounds the closure to the west and is down-dip of the trap crest. At Lilac the main trap bounding fault is L1; L1 generally trends NNW and bounds the closure to the east and is at the crest of the structure.

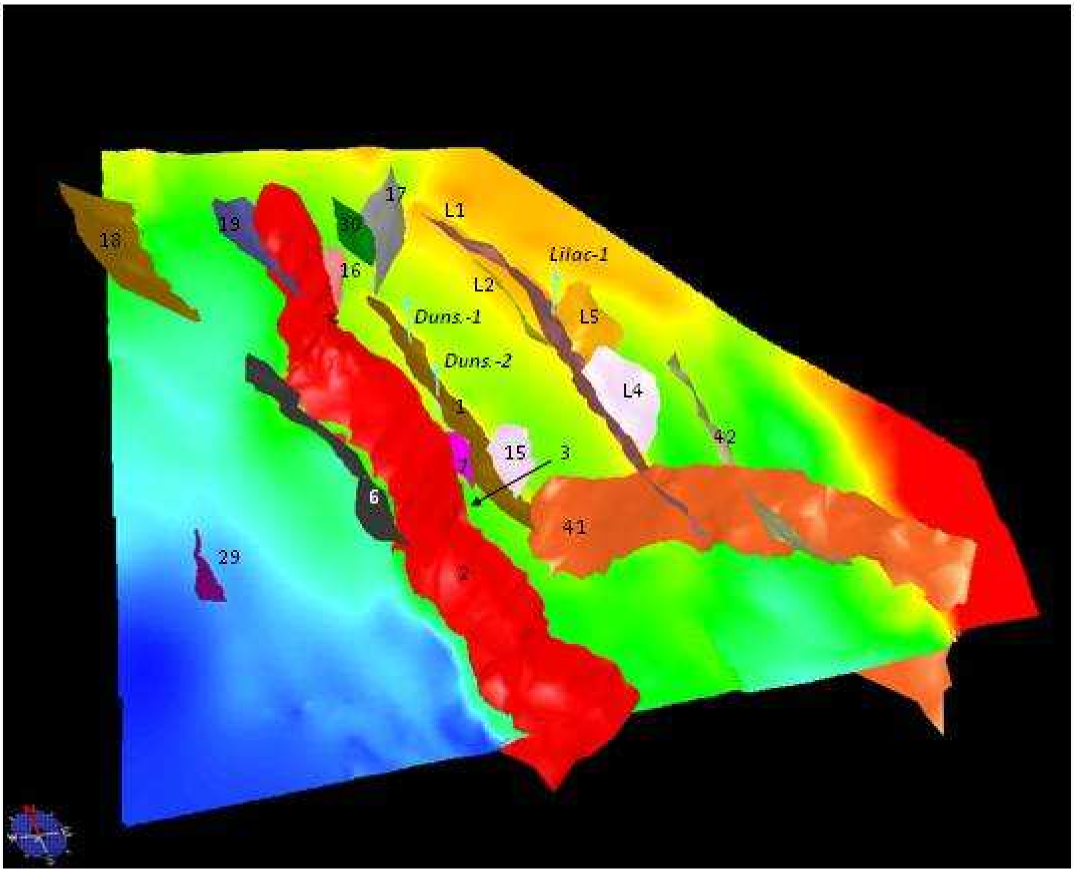

Figure 28: Permian faults for the geomechanical fault seal prediction and top reservoir structure. Fault labels refer to the geomechanical fault seal prediction (4.1); different labels are used for the geomechanical deformation modelling (4.2).

4.1.1 FRACTURE STABILITY

In the modelled stress regime for Dunsborough the overall fault trends have an average-high likelihood of fault shear failure for faults oriented in the NE direction and a low-average likelihood of fault shear failure for faults oriented in the NW direction (Figure 29). Using cohesive strength of 1 MPa and an internal coefficient of friction of 0.3 (i.e. the case for low rock strength and low internal coefficient of friction favouring failure; Figure 29A and Figure 30), the fluid pressure would need to be approximately 30-40% higher than the estimated pore pressure to induce failure on most of the NNW trending faults, including the main trap bounding faults, that is faults 1, 2 and L1 (black symbols in Figure 29A and Figure 30). However for this stress regime and using these fault rock properties (rather weak fault rock) some part of the main trap bounding faults trending to the north are predicted to fail or to be close to failure. Most of the fault elements, which are obtained from fault plane triangulation, are predicted to require additional fluid pressures between 5 and 15 MPa to be forced into failure.

Using a cohesive strength of 5 MPa and an internal coefficient of friction of 0.6 (i.e. the case for higher rock strength and higher internal coefficient of friction hindering failure; Figure 29B and Figure 31), the fluid pressure would need to be approximately 60-80% higher to induce failure on most of the NNW trending faults, including the main trap bounding faults: faults 1, 2 and L1 (black symbols in Figure 29B). Again, for this stress regime and using this fault rock properties (rather strong fault rock), some parts of the main trap bounding faults trending to the north show less stability but still require an increase of pore pressure between 40-60% to induce failure. Most of the fault elements are predicted to require additional fluid pressures between 20 and 30 MPa to be forced into failure.

The 3D fracture stability distributions are shown in Figure 30 (a cohesive strength of 1 MPa associated with an internal coefficient of friction of 0.3) and Figure 31(cohesive strength of 5 MPa associated with an internal coefficient of friction of 0.6). The fault plane orientation, like the Cliff Head model, appears to be the primary factor controlling the failure potential, with planes sub-parallel to SHmax most likely to fail due to an increase of pore pressure.

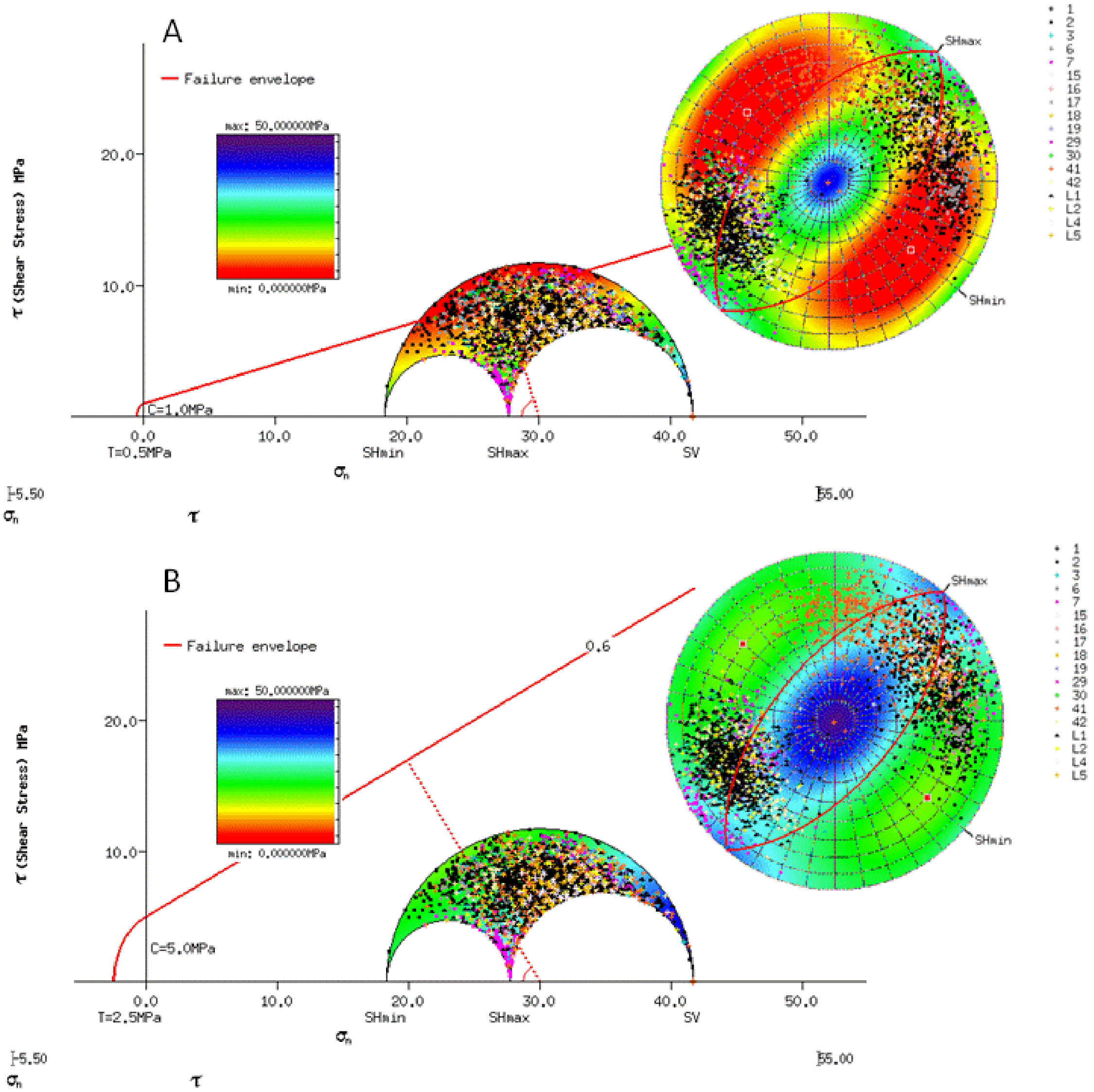

Figure 29: Fracture stability for the Permian faults at 3400 m below elevation (including 2000 m of eroded sediments; chosen as the approximate depth of the top Permian reservoir before erosion). The values on the stereonets (right) refer to the increase in pore pressure required to force the fault plane into failure; the same values are shown on the Mohr circle (left) with the failure envelope (red) defined by the fault rock properties. (A) Cohesive strength of 1 MPa and coefficient of internal friction of 0.3. (B) Cohesive strength of 5 MPa and coefficient of internal friction of 0.6.

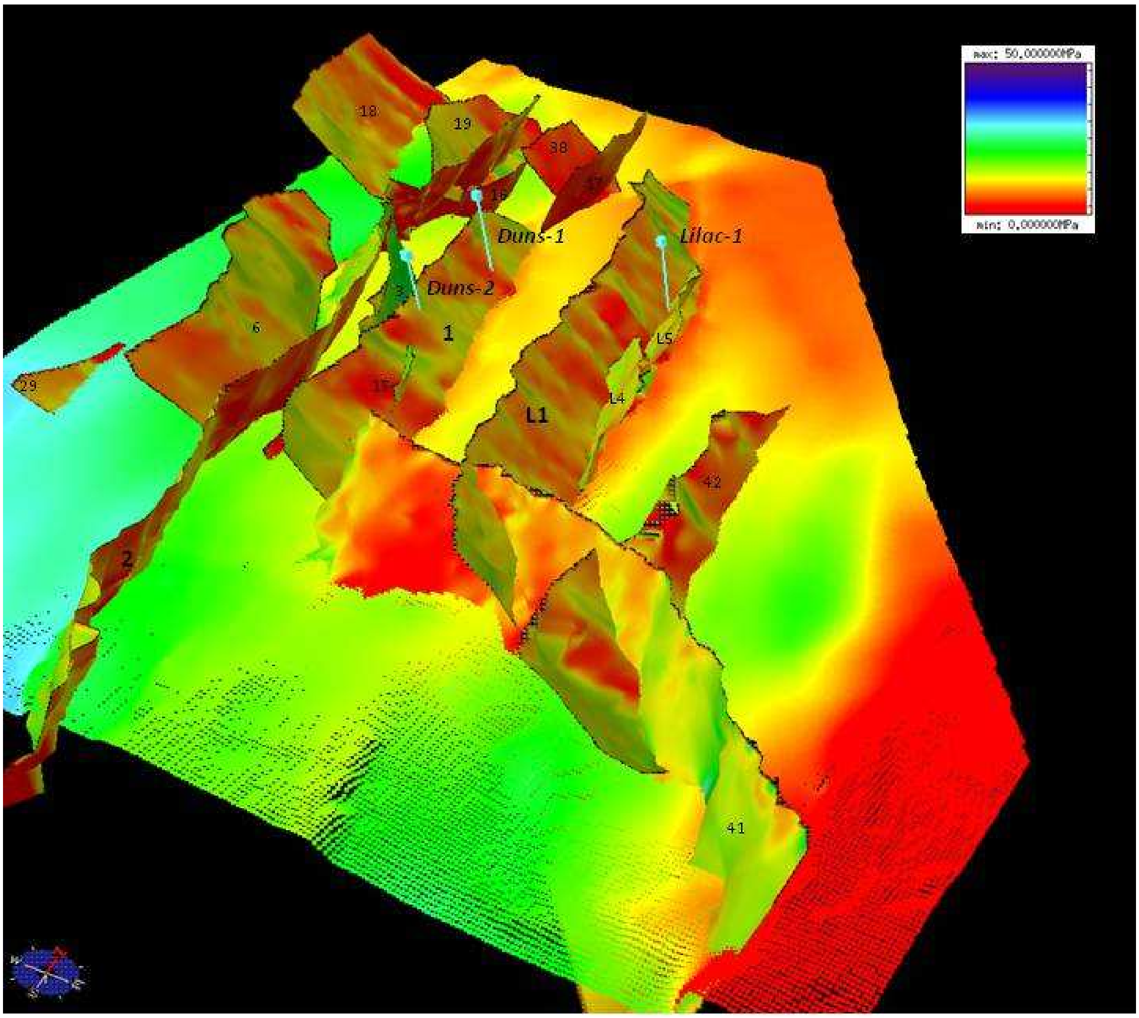

Figure 30: Fracture stability distribution (cohesive strength of 1 MPa and an internal coefficient of friction of 0.3). Maximum fracture stability is blue and minimum fracture stability red. The top reservoir surface is coloured for depth.

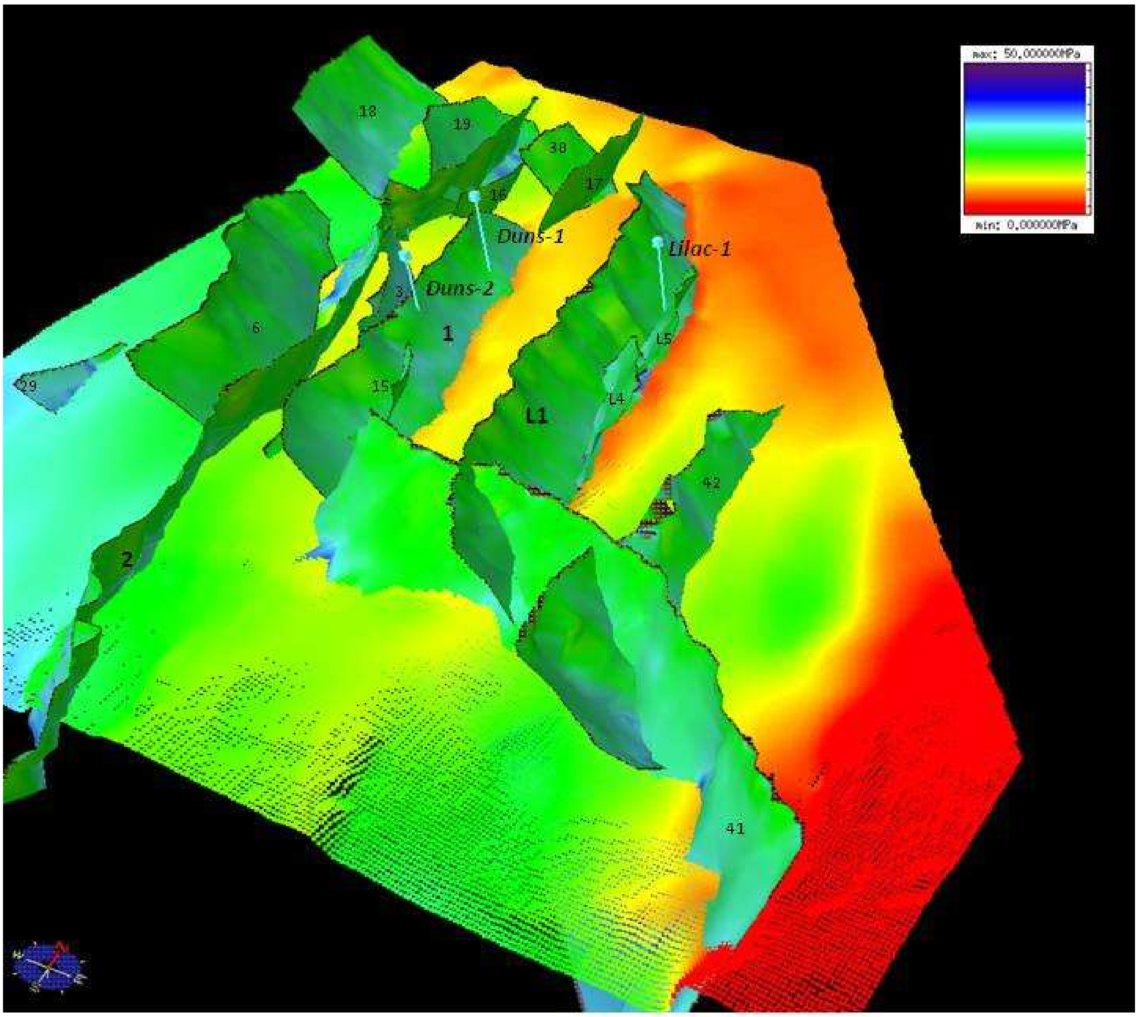

Figure 31: Fracture stability distribution (Cohesive Strength of 5 MPa and an internal coefficient of friction of 0.6). Maximum fracture stability is blue and minimum fracture stability red.The top reservoir surface is coloured for depth.

4.1.2 SLIP STABILITY

As with fracture stability, the slip stability shows that there is a higher likelihood of fault shear failure for faults oriented in the NE direction (Figure 32). With a coefficient of internal fiction of 0.48, most of the NNW trending faults would require a 40-50% increase in the fluid pressure to induce failure (an increase of at least 14-18 MPa). The faults trending to the north, however, including part of the main trap bounding faults 1, 2 and L1, are less stable and require an increase in pore pressure of around 3-12 MPa for failure to occur, that is between 8-12 MPa of pore pressure increase.

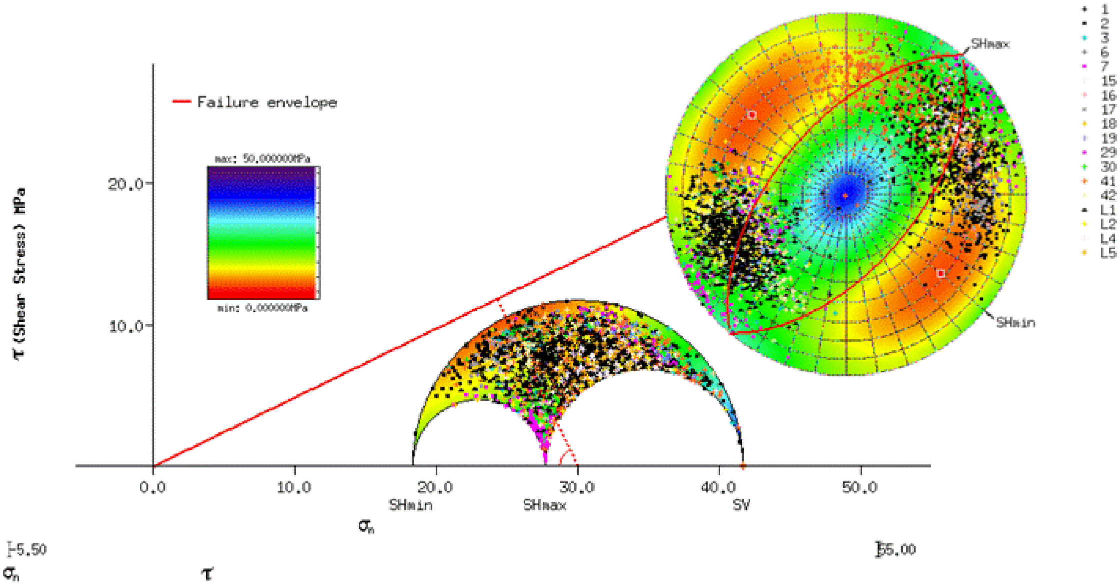

Figure 32: Slip stability for the Permian faults at 3400m below ground elevation (including 2000m of eroded sediments). Faults are cohesionless and coefficient of internal friction is 0.48. The values on the stereonets (right) refer to the increase in pore pressure required to force the fault plane into failure; the same values are shown on the Mohr circle (left) with the failure envelop (red) defined by the fault properties.

4.1.3 SLIP TENDENCY

As with the fracture and slip stability, the slip tendency shows that most of the NNE trending faults, including the main trap bounding faults (faults 1, 2 and L1; black symbols in Figure 33), are not optimally oriented to slip (average slip tendency value <0.25). However, under this stress regime, a higher slip tendency is expected for faults segments trending to the N and NE. For example faults 1 and L1 bounding the crest of the Dunsborough and Lilac structures, respectively, both include segments with increased slip tendency (c. 0.3-0.4; black arrows on Figure 34).

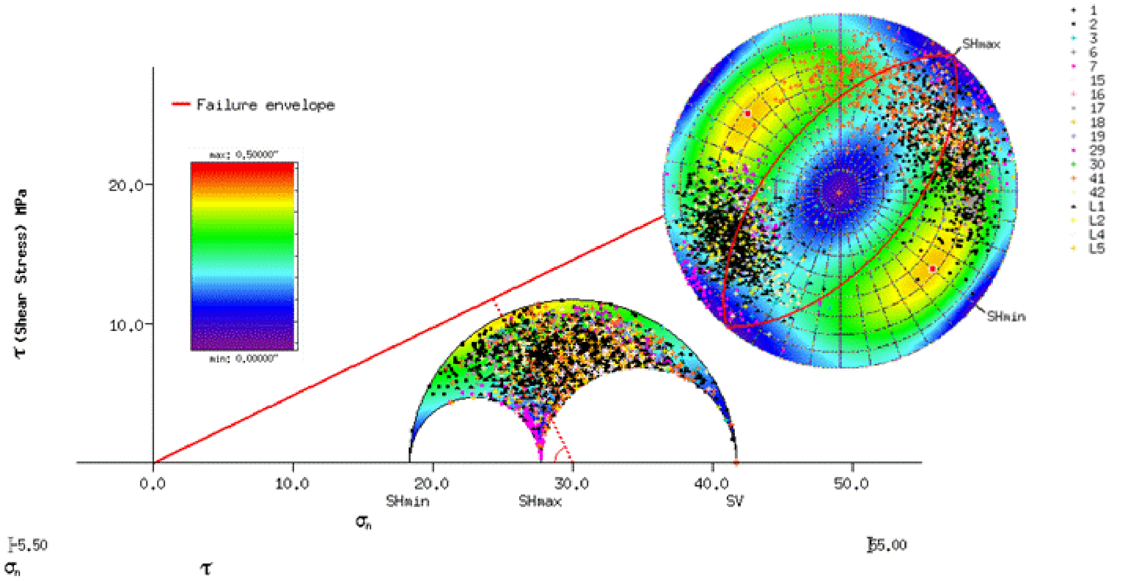

Figure 33: Slip tendency for the Permian faults at 3400m below ground elevation (including 2000m of eroded sediments). The values on the stereonets (right) refer to the likelihood of slip to occur; the same values are shown on the Mohr circle (left).

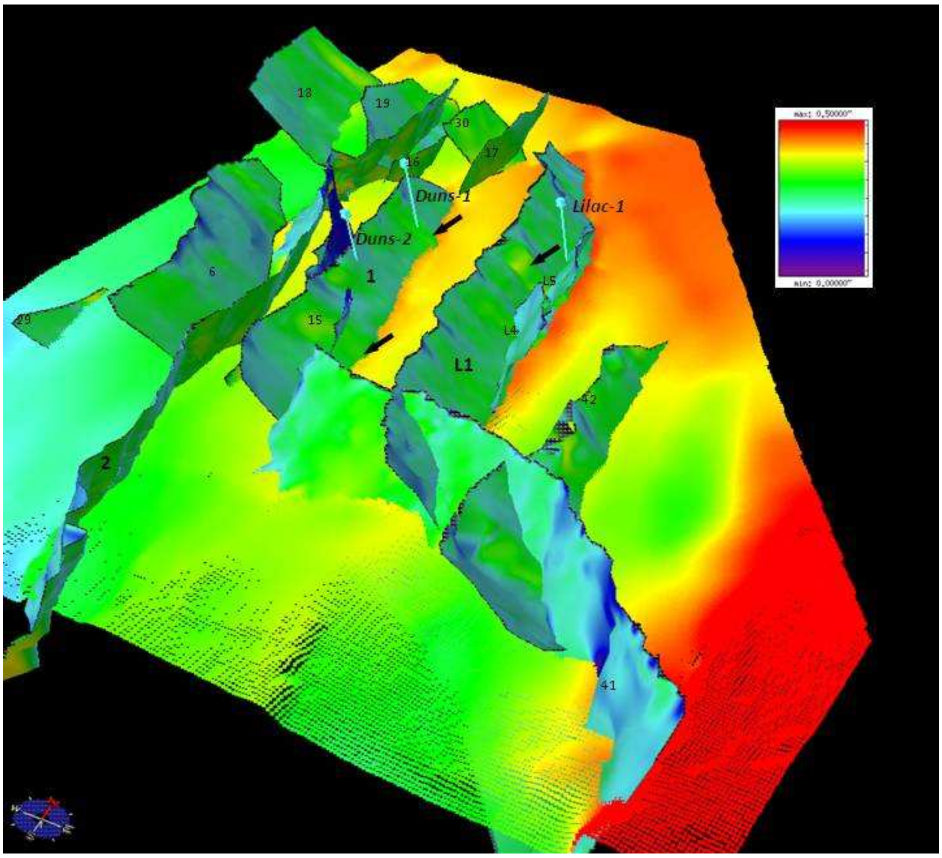

Figure 34: Slip tendency distribution. Areas of high slip tendency are present on the trap-bounding faults 1 (Dunsborough) and L1 (Lilac) (black arrows). Maximum slip tendency is red and minimum slip tendency is blue. The top reservoir surface is coloured for depth.

4.1.4 DILATION TENDENCY

Figure 35 and Figure 36 show the dilation tendency for the Permian faults Like the fracture/slip stability and the slip tendency, the most significant part of this analysis is that the dilation tendency is orientation dependent with the highest tendency values coinciding with steeply dipping NE oriented fault surfaces. However most of the NNW trending faults, including the main trap bounding faults, that is faults 1, 2 and L1 (black symbols in Figure 35) have a dilation tendency >0.5 suggesting a risk of dilation and up-fault fluid flow.

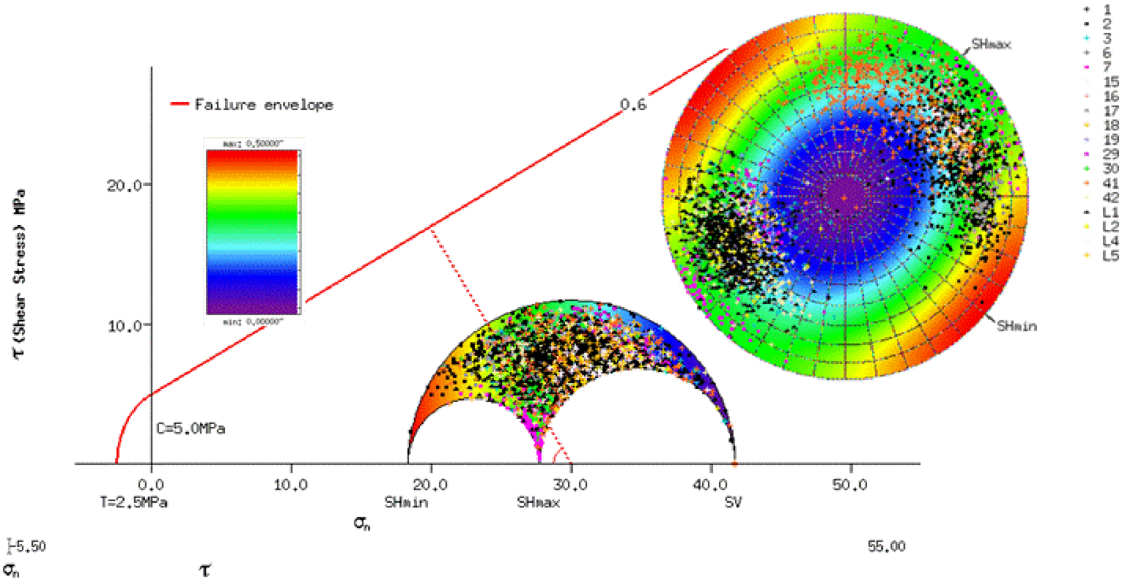

Figure 35: Dilation tendency at 3400m below ground elevation (including 2000m of eroded sediments). The values on the stereonets (right) refer to the likelihood of dilation to occur; the same values are shown on the Mohr circle (left).

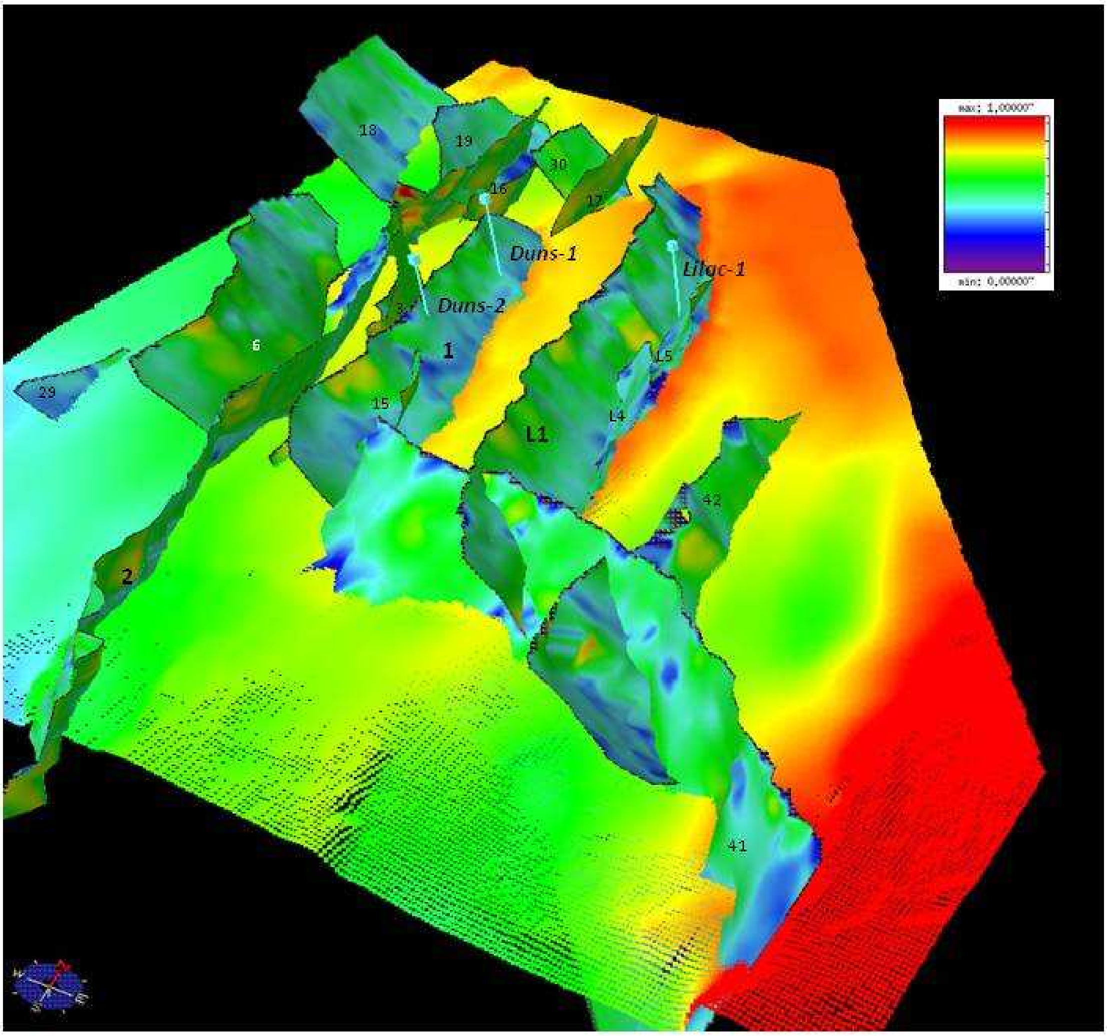

Figure 36: Dilation tendency distribution. Maximum dilation tendency is red and minimum dilation tendency is blue. The top reservoir surface is coloured for depth.

4.2 Geomechanical deformation modelling – Dunsborough and Lilac

The Dunsborough and Lilac deformation model architecture, material properties and boundary conditions are described in sections 2.2.1, 2.2.2 and 2.2.3 respectively.

4.2.1 STRAIN DISTRIBUTION

The modelling shows that fault size and orientation primarily influence the partitioning of reactivation shear and volumetric strains (Figure 37, Figure 38, Figure 39, Figure 40, Figure 41 and Figure 42). While longer faults are still more important strain-accommodating structures than shorter faults, heterogeneous strain distribution occurs (mostly lateral but also vertical) and correlates with the variation in fault strike orientation.

Faults F1 and F4, that bound both the Dunsborough and Lilac structures, accommodate most of the reactivation strain, but both show local shear strain values <0.05 and volumetric strain <2%. Both these faults have segments that divert from the general NNW trending orientation toward the west (red arrows on Figure 38C and Figure 39C). Consequently smaller faults located next to F1 and F4 show local increase in shear and volumetric strains (yellow arrows on Figure 38C and Figure 39C).

Vertical variation of strain is also observed (Figure 40 and Figure 41) and appears to be governed by the mechanical properties of the rock layers, with higher reactivation strains typically located within the shallower overburden unit. This may also be influenced by mechanical pressures (normal stresses on faults), which decrease at shallower levels and hence promote mechanical failure and dilation. Like the Cliff Head model, fault tips (e.g. F1) are associated with locally higher volumetric strains.

Fault growth and lateral interaction between faults F3 and F2 is reflected by high strains localized at the fault tips (Figure 38A and B and Figure 39A and B). This suggests a higher potential for fracture development.

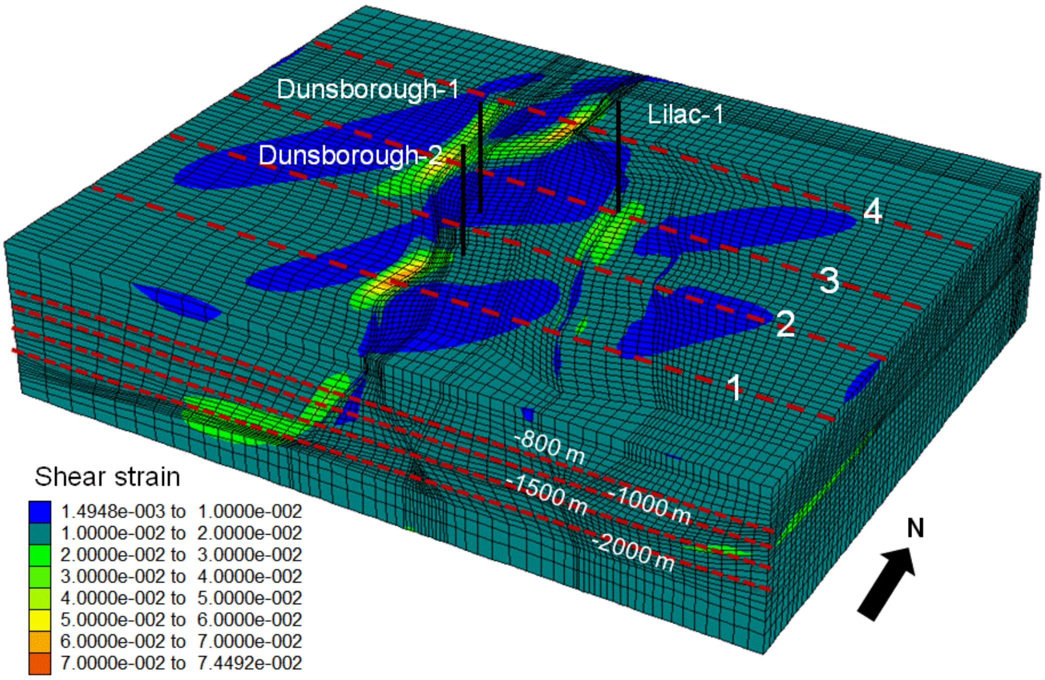

Figure 37: 3D shear strain distribution and location of cross-sections and plan views. Maximum strain is red and minimum strain is blue.

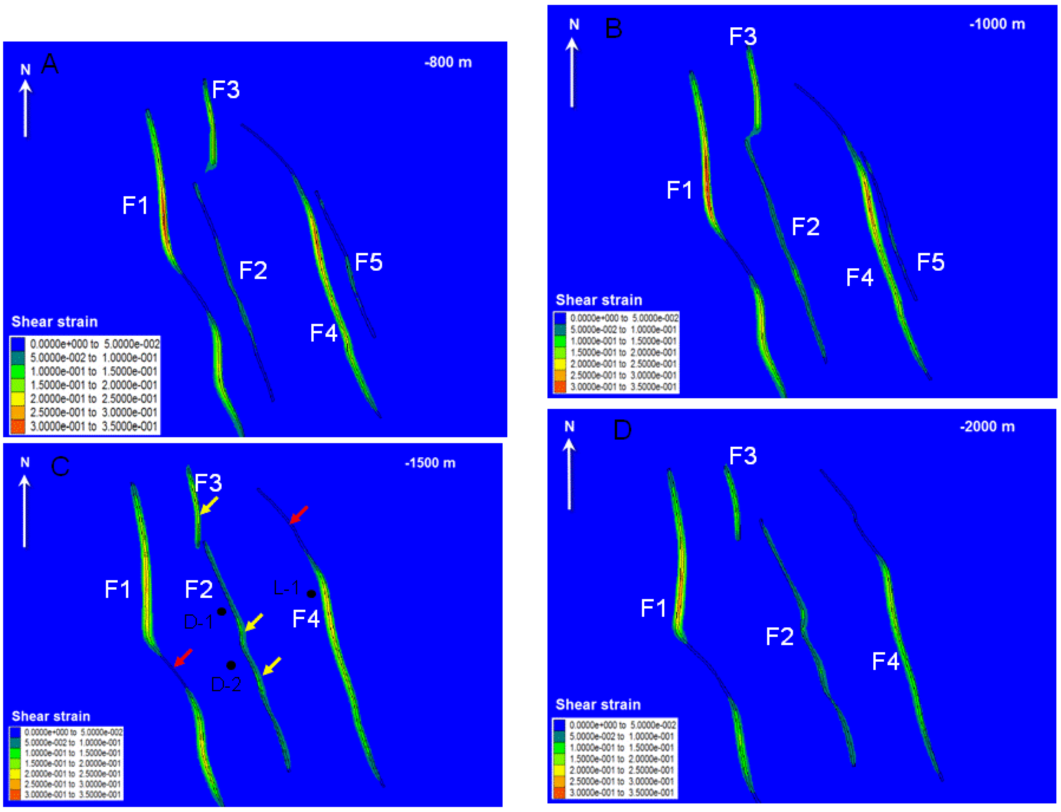

Figure 38: Shear strain distribution in plan view after 2% extension. Maximum strain is red and minimum strain is blue. (A) Horizontal slice at 800m below seabed. (B) Horizontal slice at 1000m below seabed. (C) Horizontal slice at 1500m below elevation, i.e. near top reservoir level. The red arrows show local decrease in shear strain accommodation on NW oriented segments. Yellow arrows show local increase in shear strain accommodation on NNW oriented segments adjacent to low strain segments. (D) Horizontal slice at 2000m below seabed.

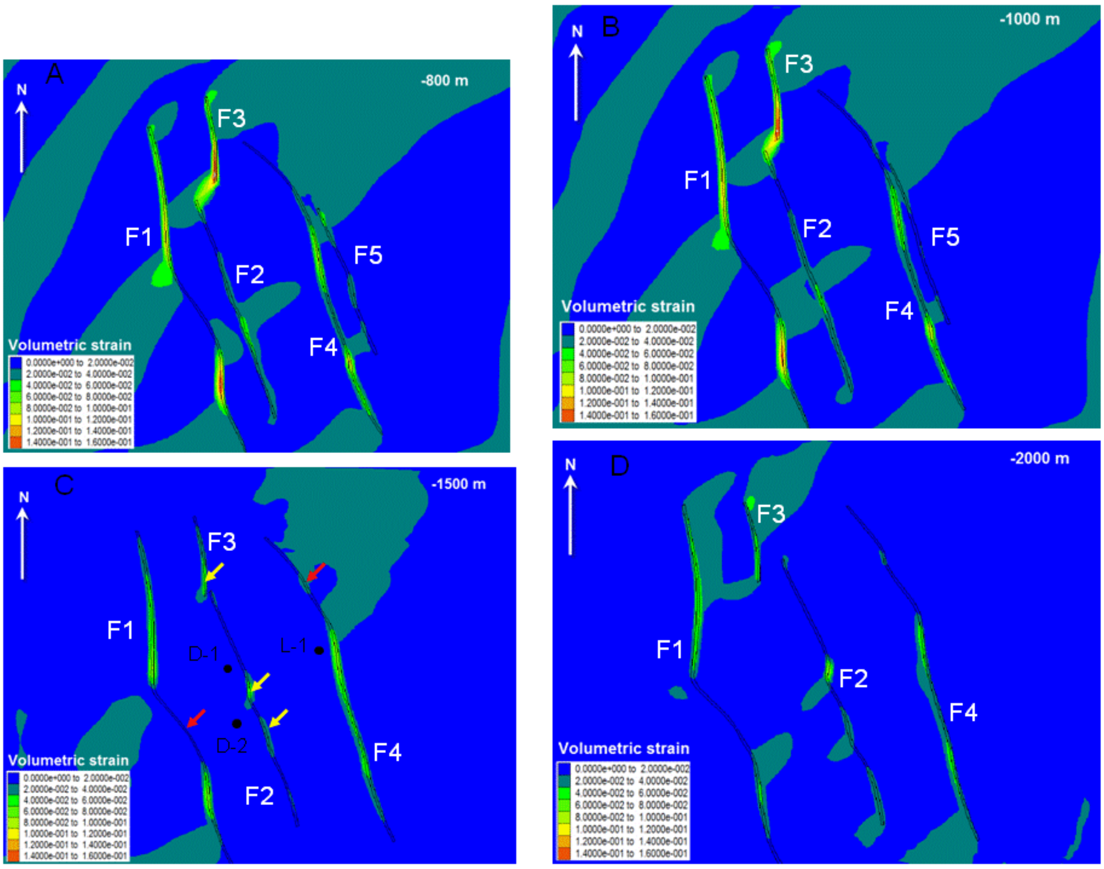

Figure 39: Volumetric strain distribution in plan view after 2% extension. Maximum strain is red and minimum strain is blue. (A) Horizontal slice at 800m below seabed. (B) Horizontal slice at 1000m below seabed. (C) Horizontal slice at 1500m below seabed, i.e. near top reservoir level. The red arrows show local decrease in shear strain accommodation on NW oriented segments. Yellow arrows show local increase in volumetric strain accommodation on NNW oriented segments adjacent to low strain segments. (D) Horizontal slice at 2000m below seabed.

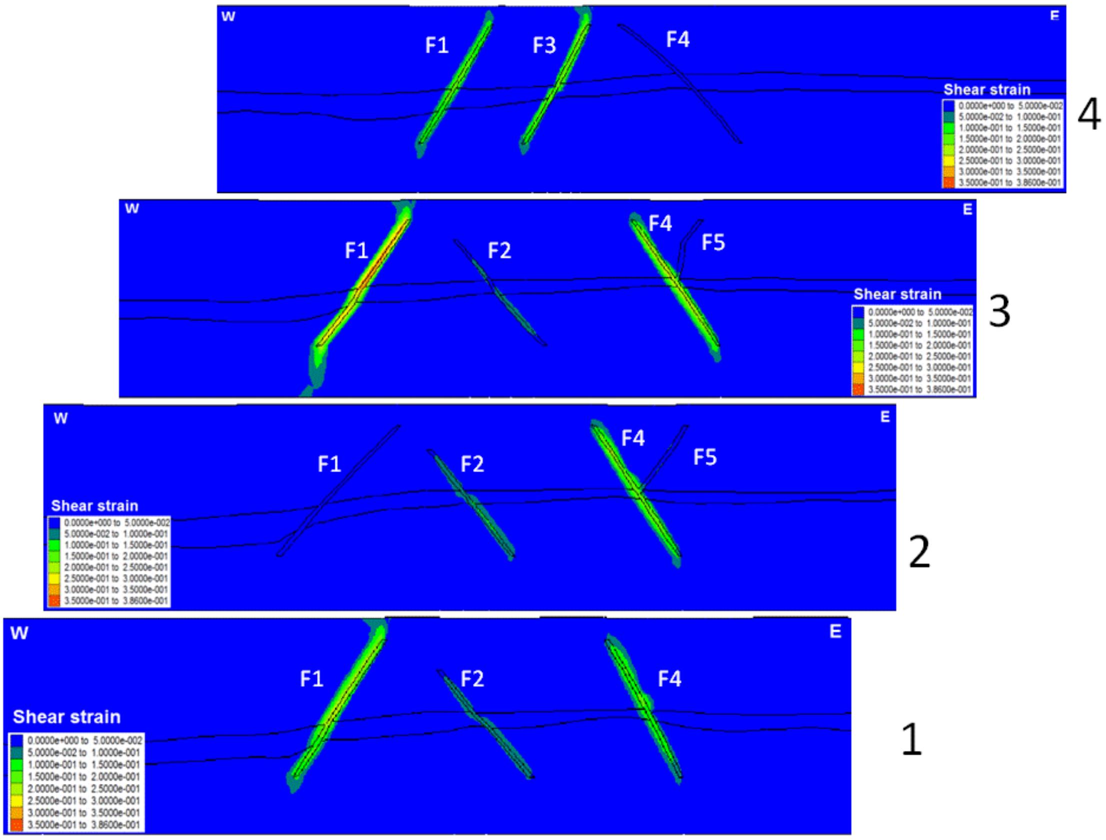

Figure 40: Shear strain distribution in cross-section view after 2% extension. Maximum strain is red and minimum strain is blue.

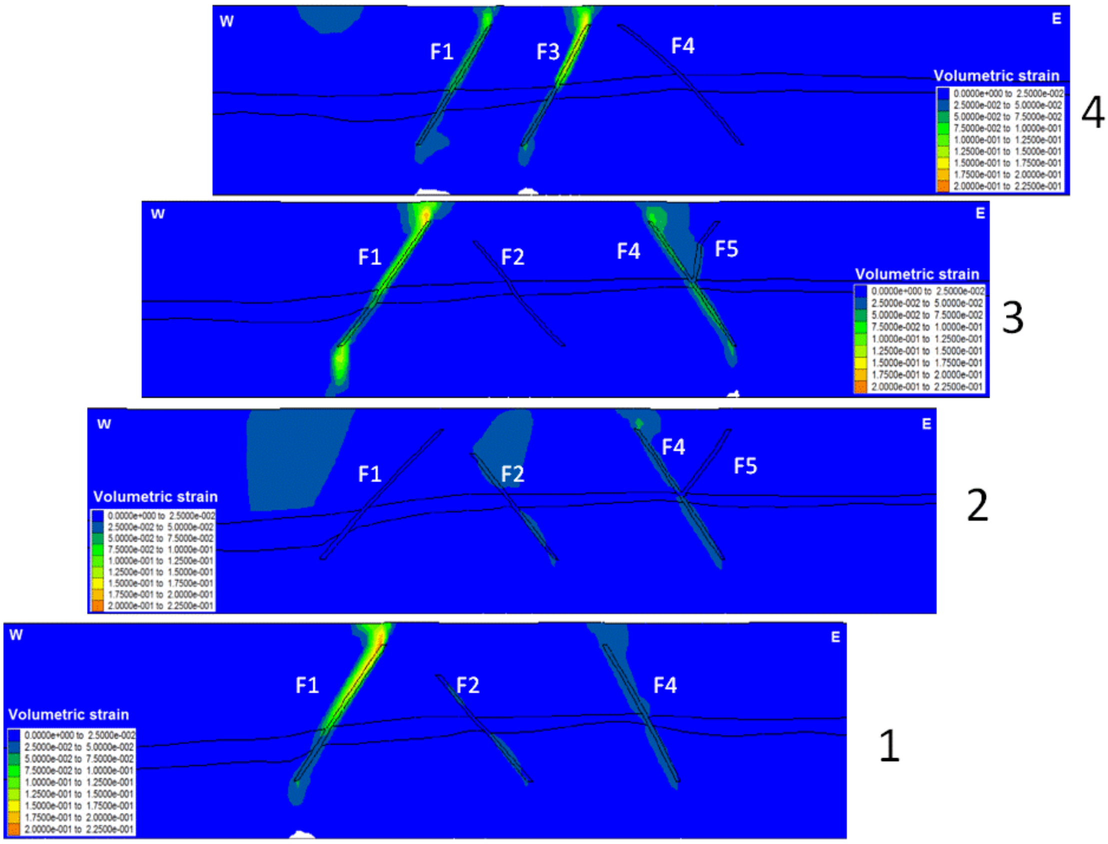

Figure 41: Volumetric strain distribution in cross-section view after 2% extension. Maximum strain is red and minimum strain is blue.

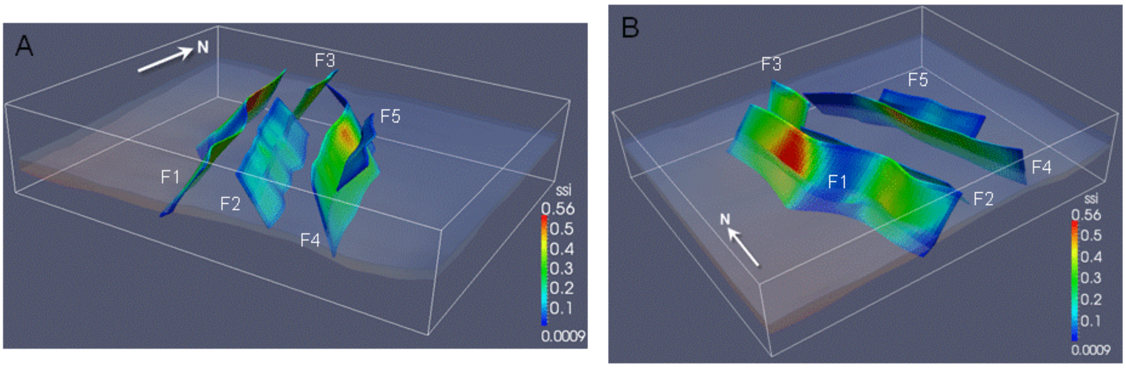

Figure 42: 3D shear strain distribution after 2% extension. Maximum strain is red and minimum strain is blue. (A) South-east view. (B) South-west view showing the lateral variation in shear strain distribution for fault F1.

4.2.2 STRESS DISTRIBUTION

Plan and section-view patterns of mean stress and shear stress distribution are shown in Figure 43 to Figure 45. Their characteristics are generally consistent with those for the Cliff Head model, such as lower mean and shears stress within reactivated fault zones and higher shear stress near fault tips or between adjacent fault tips. In addition, the current models for the Dunsborough Field and Lilac structure also highlight the presence of lower mean stresses and shear stresses in the hanging-wall side of faults (note that the Cliff Head model also has this features as expressed by lower mean stress in the hanging-wall side of the Geraldton Fault (see Figure 23A). Section plots of stresses (Figure 44 and Figure 45) show that lower mean stresses and shear stress at the hanging-wall side of faults predominantly occur around the upper section of faults near top fault tips.

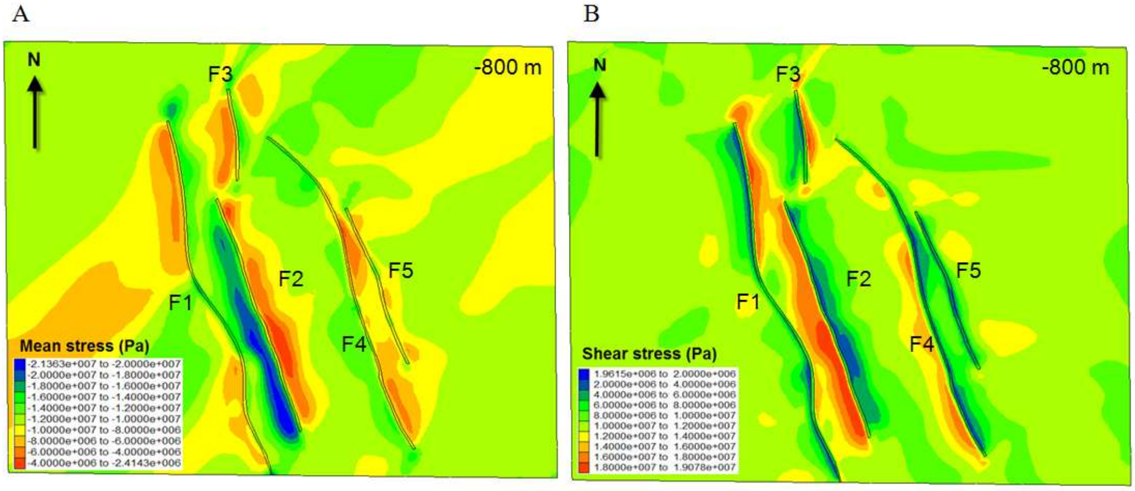

Figure 43: Plan-view stress patterns for a horizon at the 800m level in the model for the Dunsborough Field and Lilac structure. (A) Mean stress. (B) Shear stress. For mean stresses, negative values denote compressive stresses. Shear stresses all have positive values.

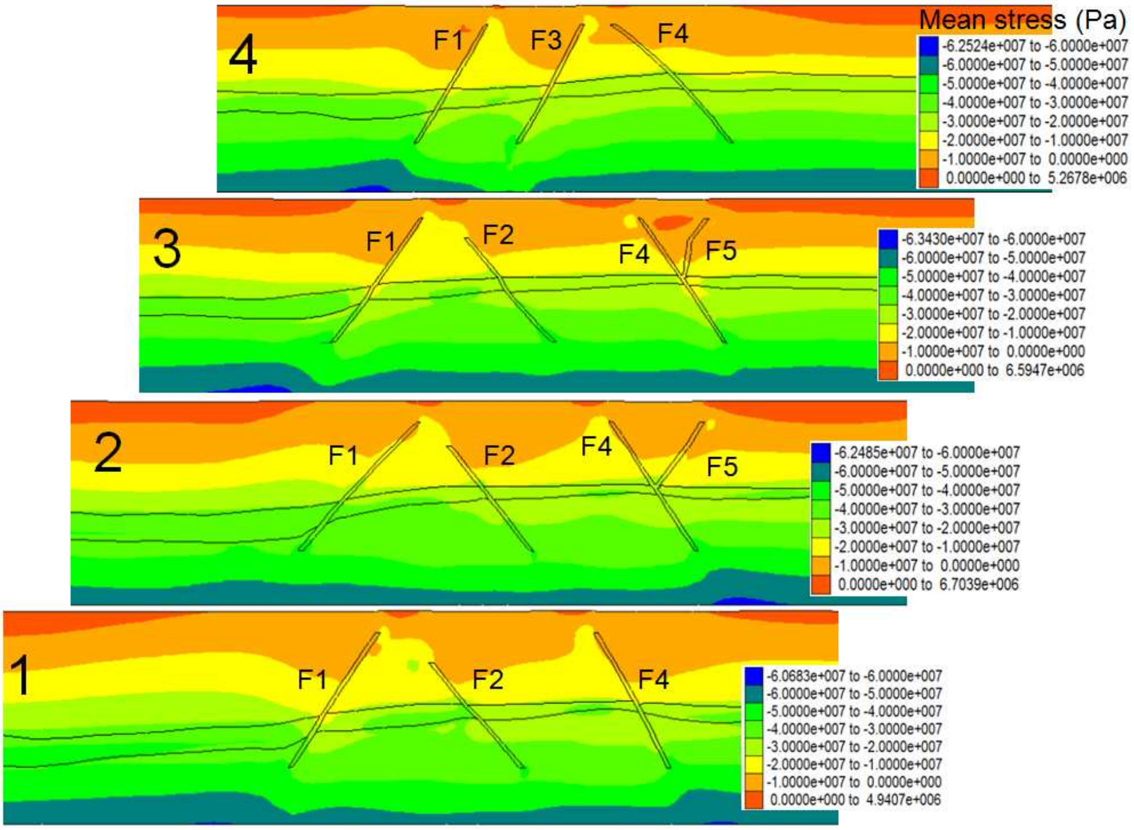

Figure 44: Plots of mean stress patterns for 4 cross-sections in the model for the Dunsborough Field and Lilac structure. Negative values denote compressive stresses. Cross-section locations are shown in Figure 37.

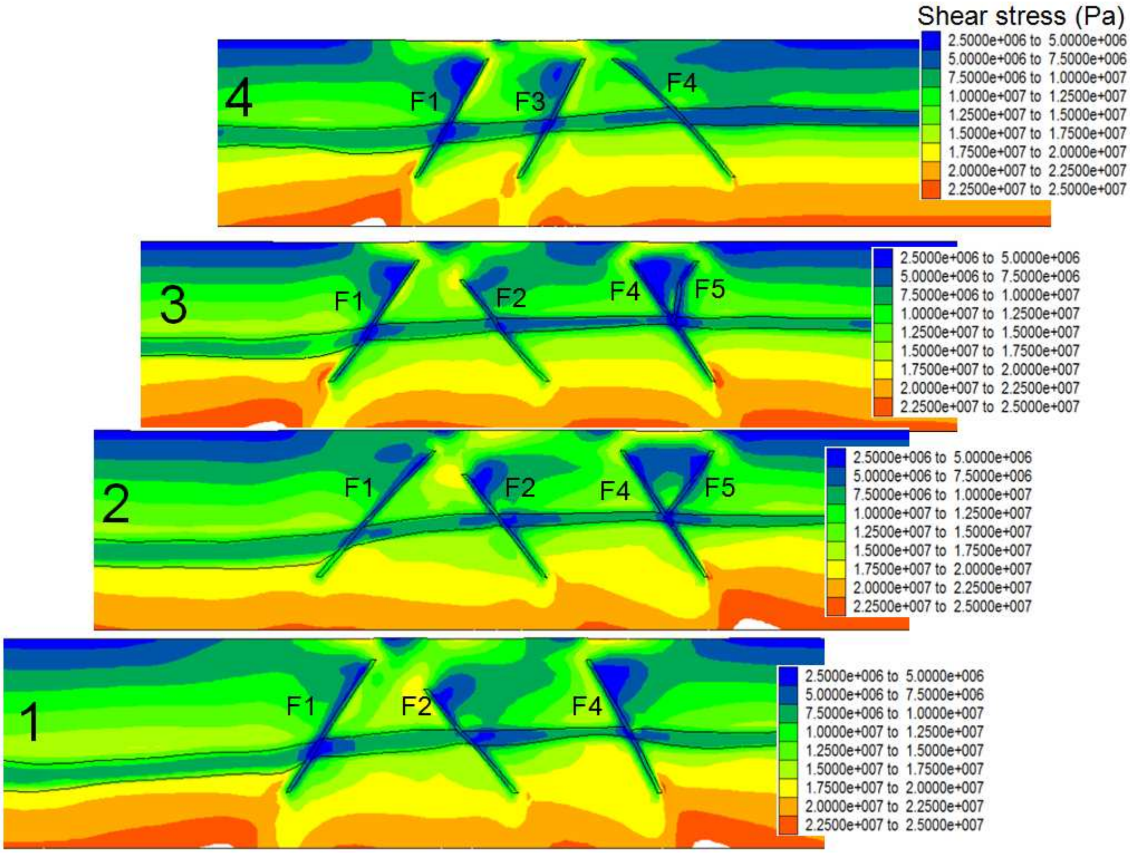

Figure 45: Plots of shear stress patterns for 4 cross-sections in the model for the Dunsborough Field and Lilac structure. Cross-section locations are shown in Figure 37.

4.3 Discussion – Dunsborough/Lilac

The Dunsborough trap currently has an oil column below a gas cap. Based on the depth to top seal (Kockatea Shale) at 1466 mMD, a 13 m gross gas column (ROC Oil ASX release 2007) extends down to 1479 mMD, below which the oil leg extends down to 1491 mMD (giving a 25 m gross column).A large 52 m gross palaeo-oil column was identified in the Permian Dongara Sandstone and Irwin River Coal Measures from fluid inclusion data (Kempton et al., 2011a; Figure 71). Lilac-1 was later drilled to test an equivalent fault block trap to the east and failed to find movable hydrocarbons. A large 35.5 m gross palaeo-oil column, however, was identified in the same Permian Formations (Figure 72). Although both traps are located on a north-south oriented, rotated fault block, with faults hard-linked through the top seal, these data suggest that the Dunsborough trap experienced only partial leakage, while the Lilac trap was totally breached.

The geomechanical deformation models are consistent with this overall charge history with:

- the Dunsborough crest-bounding fault (F2 in Figure 38 and Figure 39), partly protected from strain by the large fault F1(Figure 38), suggests a lower risk of up-fault fluid flow; and
- the Lilac crest-bounding fault, associated with high shear and volumetric strains (F4 in Figure 38 and Figure 39), suggests a higher risk of up-fault fluid flow.

4.3.1 DUNSBOROUGH AND LILAC PALAEO-ACCUMULATION

The palaeo-charge history of the Dunsborough Field is well constrained at the time fluid inclusions were trapped in both quartz cement and a later phase of carbonate, but the subsequent fill and spill history, associated with loss of oil and gas charge, is uncertain. The palaeo-charge reconstruction data, detailed in Appendix A and Figure 71, suggest:

- a palaeo-oil column in Dunsborough-1 of at least 52 m in height below the Kockatea Shale seal (3.8% GOI at 1518 mRT) and is unconstrained below this in a finer/shaly section of the reservoir. The highest known palaeo-water zone is indicated at 1545 mRT (0.1% GOI; Figure 46B),
- a palaeo-oil column in Dunsborough-2 of at least 16 m in height below the Kockatea Shale seal (27.2% GOI at 1531 mRT) and unconstrained down to a maximum depth of 1545 mRT (highest known palaeo-water zone; 0.4% GOI; Figure 46A). A possible larger palaeo-oil column down to 1573 m is based on fluid inclusions in a later phase of carbonate cement and is consistent with oil shows.

The extent of the palaeo-accumulation in the Dunsborough trap is required in order to evaluate the effect of the reactivation strain on the trap-bounding fault. We present here two scenarios that honour the charge data.

The first scenario is relies primarily on the GOI data (Figure 71). A palaeo oil-water contact (P-OWC1a in Figure 46A) was present in Dunsborough-2 somewhere between 1531 mRT (palaeo oil down to or P- ODT) and 1545 mRT. A palaeo oil-water contact (P-OWC1b in Figure 46B) can be defined in Dunsborough-1 between 1518 mRT (P- ODT) and 1545 mRT (i.e. within the finer/shaly section of the reservoir). Therefore a palaeo-oil-water contact common to both wells could be present between 1531 mRT and 1545 mRT (P-OWC1 in Figure 46). This relates to palaeo-oil charge at the time quartz cement crystallised and at a time before charge scenarios that include inclusions in carbonate cement and the oil shows in Dunsborough-2 between 1540 mRT and 1571 mRT.

The second scenario takes into account the inclusions in a later carbonate cement in Dunsborough-2, that are coincident with conventional oil shows, and suggest the palaeo oil-water contact (P-OWC2 in Figure 46A) in this well deepened to 1571 mRT (well constrained on sample spacings). However the P-OWC2 in Dunsborough-2 is currently 25 m deeper than the deepest known palaeo oil-water contact in Dunsborough-1 (D-POWC2 at 1545 mRT, Figure 46B) based on GOI and the absence of oil shows in sandy reservoir below 1545 mMD; this suggests a post-charge rotation of the fault block to the south that would bring Dunsborough-2 to its current position (Figure 46C).

Charge data for the Lilac trap (Figure 72; Appendix A) indicates a 42 m palaeo-oil column with a P-OWC bracketed at 1420 mRT by successive samples.

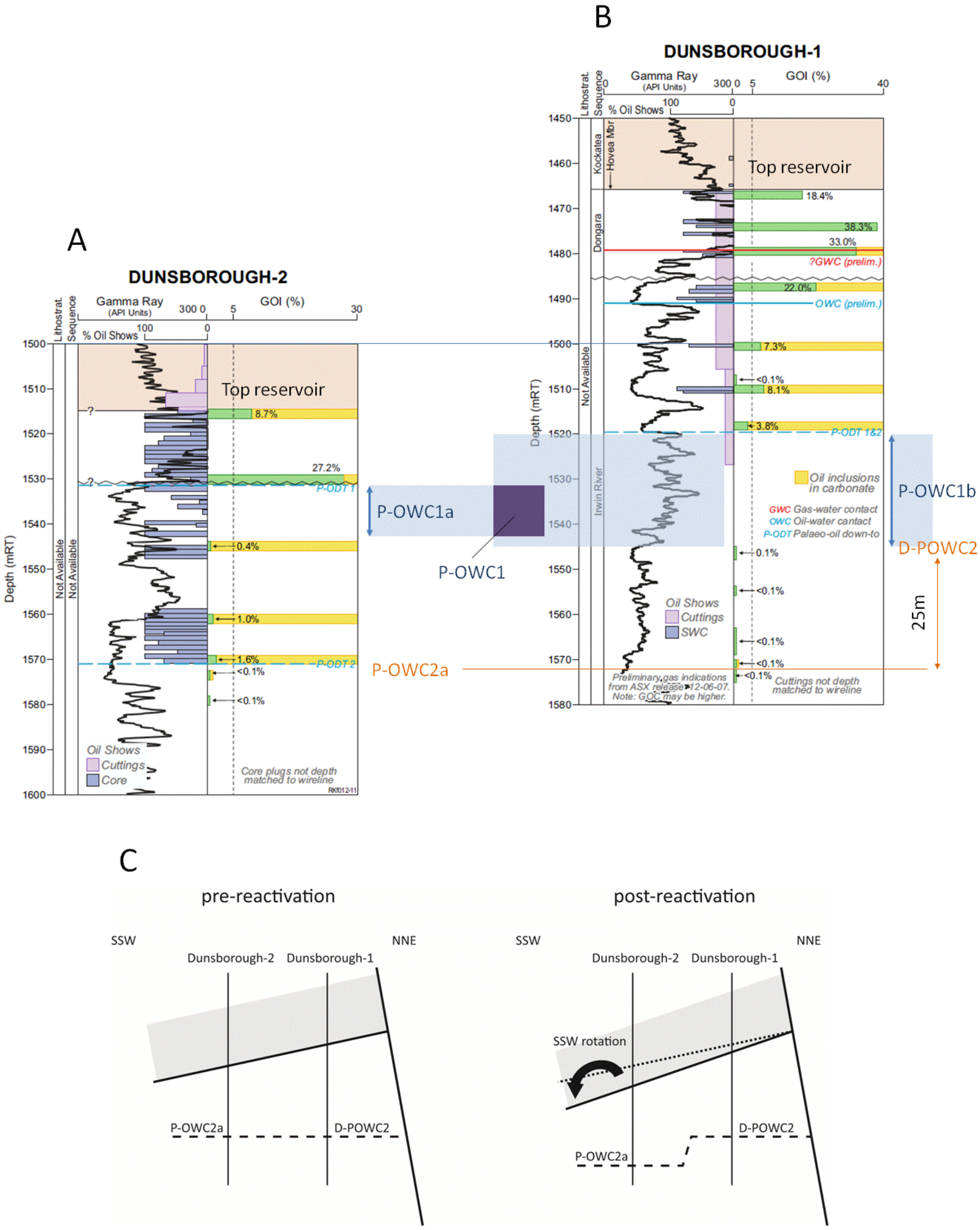

Figure 46: Palaeo-charge scenarios for the Dunsborough Field. (A) Dunsborough-2 well with GOI data and oil shows. P-OWC1a is the palaeo-oil-water contact for the first charge scenario based on the GOI data. P-OWC2a is the palaeo-oil-water contact for the second charge scenario based on the GOI data and oil shows. P-OWC1 is the common depth range for both P-OWCs defined in Dunsborough-1 and -2 for the first charge scenario. (B) Dunsborough-1 well with GOI data and oil shows. P-OWC1a is the palaeo-oil-water contact for the first and second charge scenario based on the GOI data and oil shows. D-POWC2 is the deepest palaeo-oil-water contact based on the GOI data located 25 m above P-OWC2a (see text for discussion). (C) A post charge block rotation, coeval with the Middle-Jurassic to Early Cretaceous reactivation could be responsible for the depth of P-OWC2a in Dunsborough-2.

4.3.2 GEOMECHANICAL MODELS AND PALAEO-ACCUMULATIONS

The geomechanical fault seal prediction and the deformation model show that fault segments trending to the NNW are more likely to reactivate under the Middle Jurassic to Early Cretaceous stress field than the segments trending to the NW. This phenomenon is explained by the relationship between the fault plane geometry and the horizontal stress orientations that governs the lateral distribution of reactivation strain (e.g. Figure 38C).

The deformation model suggests that the strain partitioning between the main faults forming the Dunsborough structure (fault F1 and F2) is directly affected by the lateral variation of strain accommodated by fault F1 (Figure 47). Local strain loci are predicted on the fault F2 (i.e. fault bounding the Dunsborough trap to the East), within the present-day closure (Figure 47A). They coincide with a decrease in strain accommodation on F1 where the fault locally bends to the NW. The slip tendency model also shows a potential local increase for the fault segment adjacent to Dunsborough-1 (Figure 34).

The comparison between the modelling outcomes and the palaeo-accumulation suggests a possible mechanical interpretation for the present-day OWCs and P-OWC distribution in Dunsborough-1 and -2 (Figure 46).

Prior to the reactivation, the palaeo-accumulation covered most of the Dunsborough block (Figure 47B). At the time of reactivation, local volumetric and shear strain loci are modelled on the central part of the Permian crest-bounding fault F2 with shear strain values around 0.15 (Figure 38 and Figure 39). Similar modelling in the Timor Sea (Langhi et al., 2010) suggests that reactivation shear strain values around 0.2 are sufficient to allow temporary migration pathways to develop through approximately 1000 m of shaly cap rock. Therefore, we propose that the shear deformation and dilation could be sufficient to trigger migration pathways to develop through the 250 m thick top seal at Dunsborough and to sustain temporary high structural permeability. This top seal bypass is likely to have developed under continuing oil charge (that is the Late Jurassic to Early Cretaceous main pulse of hydrocarbon generation and migration, Jones et al., 2011). Subsequent hydrocarbon loss may have been controlled by the difference between the rate of leakage from the reservoir and the rate of charge to the reservoir.

Figure 47C shows the present-day oil-water contact (OWC) as defined earlier at approximately 1490 mRT. The reactivation shear strain loci are located on the present-day sealing crest-bounding fault F2. This suggests fault close-up (self-healing) following the reactivation climax. A similar process has been proposed from geomechanical models and charge history data in the Timor Sea— with the initial fault-leakage pathways able to close following the climax of tectonic reactivation with possible residual “soft-bleeding” occurring later on.

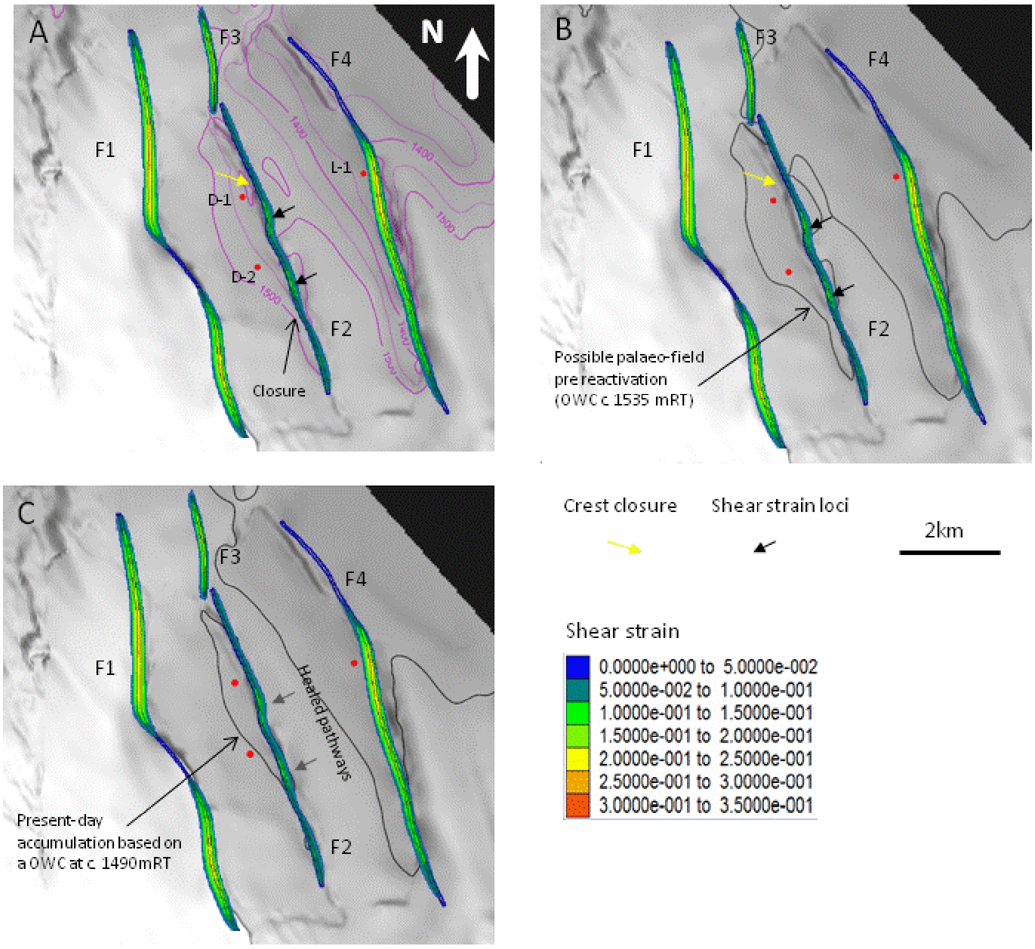

Figure 47: Relationship between shear strain distribution and charge history for the Dunsborough trap. . Top reservoir depth in m SS. (A) Shear strain distribution and present-day structure. (B) Shear strain distribution and possible palaeo-oil column down to c. 1535 mRT (c. 1505 mSS). (C) Shear strain distribution and present-day oil column.

Shear strain values on fault F4, bounding the Lilac structure, are greater on average than in Dunsborough (>0.2; Figure 48A). On the basis that there is no oil in the Lilac structure, this high deformation values may indicate a critical increase in structural permeability creating open conduit without subsequently closing-up. Figure 48B shows the palaeo oil-water contact (P-OWC) at 1420 mRT, as defined from charge data (Figure 72, Appendix A).

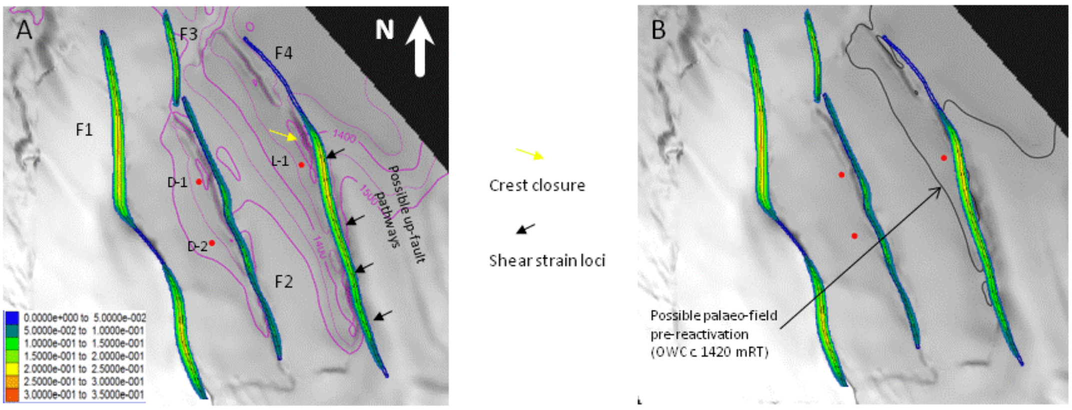

Figure 48: Relationship between shear strain distribution and charge history for the Lilac trap. Top reservoir depth in mSS. (A) Shear strain distribution and present-day structure. (B) Shear strain distribution and palaeo-oil column down to c. 1420 mRT (c. 1390 mSS).

4.3.3 FAULT SLIP HISTORY – DUNSBOROUGH AND LILAC

Although the fault surfaces bounding the Dunsborough and Lilac traps are interpreted from seismic data as continuous planes, that is, offsetting Permian to Cretaceous sediments, throw data (Figure 49A) shows two distinct levels of throw maximum (Permian and Middle Jurassic). This throw distribution on fault F4 (bounding the Lilac trap, Figure 49) suggests that the surface results from the dip-linkage of: (i) upper segments nucleating in the Yarragadee and/or Cadda formations and propagating downward and, (ii) Permian segments reactivated during the Late Jurassic to Early Cretaceous extension and propagating upward. The Mesozoic fault segments overlying the Lilac structure shows high throw values >80 m extending down to the close vicinity of the top seal, which reflects the extensive downward growth of the Mesozoic segments due to high strain accommodation and the consequent high likelihood of leakage pathway development in the top seal.

The throw distribution on fault F2 (bounding the Dunsborough trap, Figure 49B) shows high throws (>100 m) at the Permian level, but restricted maxima (<50 m) at the Middle Jurassic level. This suggests that, although hard-linkage is interpreted from seismic data, the connectivity through the top seal is likely to be lower than for the Lilac fault F4, being the result of less downward fault growth. This scenario could explain the efficient fault self-healing (post reactivation close-up) and the present-day sealing potential of fault F2. Furthermore, although shear strain accommodated by fault F2 (locally >0.15; Figure 47) could ensure a temporary bypass of the top seal, this appears to be insufficient to sustain a long term pathway from the reservoir to the overburden.

As the Kockatea Shale thickness remains locally constant (245-250 m) over the Dunsborough and Lilac structures one can propose: (i) a minimal empirical throw threshold on Jurassic-Cretaceous faults of <50m for short-lived pathway development (i.e. F2) and (ii) a minimal empirical throw threshold on Jurassic-Cretaceous faults of >80 m for long-lived pathway development.

In summary the outcomes from the *geomechanical deformation* (4.1) and the *geomechanical fault seal prediction* (4.2) models suggest that the charge history for the Dunsborough structure could be adequately explained by the partition of reactivation strain on the trap-bounding faults. While the trap crest bounding fault (i.e. F2 in Figure 39) is smaller than the neighbouring faults F1 and F4 (Figure 39), it shows local increase in shear and volumetric strain accommodation due to local bends and decrease in strain accommodation by the *shielding* fault F1 (Figure 39). We propose that this framework could contribute to the development of temporary critically-stressed fault segments acting as short-lived conduits. The models suggest that the crest of the Lilac structure is bounded by a high strain accommodating fault that was likely to have leaked during the Middle Jurassic to Early Cretaceous reactivation.

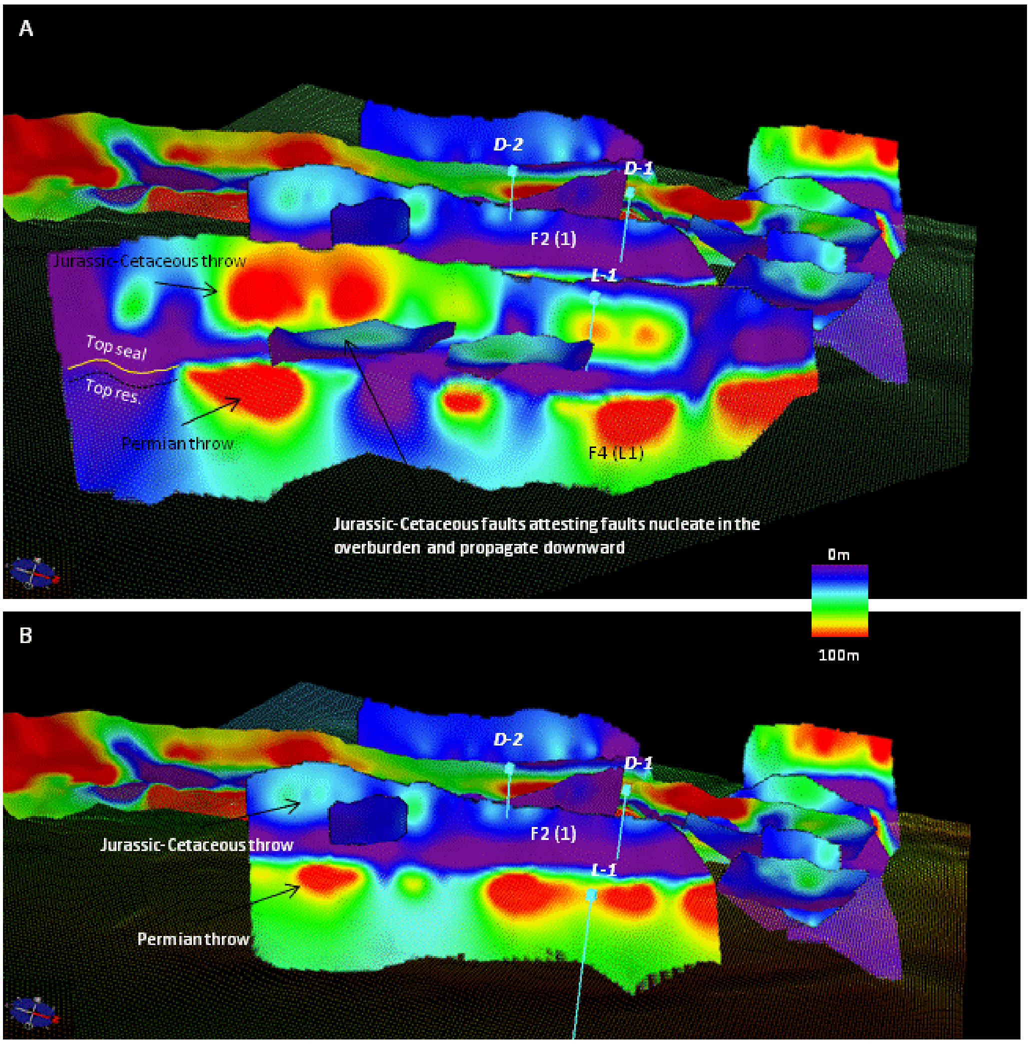

Figure 49: on the Permian and Mesozoic faults for the Dunsborough and Lilac structures. (A) Throw distribution with the Lilac bounding-fault F4 in the foreground. (B) Throw distribution with the Dunsborough bounding-fault F2 in the foreground.

5 Morangie Breached trap

Morangie-1 was drilled in October 2002 by Origin Energy Developments Pty Ltd within the Wittecarra Terrace of the Abrolhos Sub-basin. The well tested a tilted horst with dip closure to the south and was fault bounded in all other directions. Good hydrocarbon shows ranging from 30% to 100% fluorescence were recorded from 2109 to 2134 mMD in the Wagina Formation (Origin Energy Developments Pty Ltd, 2003). Log analysis interprets 58 m of net good quality reservoir with only 3.3 m of net pay. Morangie-1ST1 was sidetracked from Morangie-1 at 840 mRT to test the oil shows, however, MDT data failed to indicate a moveable oil gradient suggesting the existence of a residual oil column in the Morangie structure. Morangie-1 and Morangie-1ST1 were plugged and abandoned.

The fault displacements observed from seismic data indicate that the reactivated Permian reservoir faults and the Mesozoic faults connect across the top seal and form hard-linkages.

5.1 Geomechanical fault seal prediction – Morangie

The stress fields used in the modelling of the stress regime on the fault planes are described in section 2.1.5.

Gorter and Deighton (2002) suggested that up to 300 m of Yarragadee Formation was eroded during the Valanginian breakup and the models here are based here on the fault seal attribute related to an extensional stress regime (Sv>SHmax>Shmin) associated with an extra 300 m of Yarragadee overburden. This additional rock column does not affect the stress gradients described in section 2.1.5 (Sv=0.0235 MPa/m; SHmax=0.018 MPa/m and Shmin=0.016 MPa/m). However, it does result in an increase in the stress state at the Permian reservoir level before the erosion occurs (i.e. 3400 m below palaeo-elevation), with Shmin=55 MPa, SHmax=64 MPa and Sv=78 MPa.

Rock and fault rock properties of the model are described in section 2.1.6.

The configuration of the Permian faults used for the geomechanical fault seal prediction is shown in Figure 50. The main trap bounding faults are F1 and F3; (i) the F1 fault generally trends NNW, bounds the closure to the west and is down-dip of the trap crest while, (ii) the F3 fault trends NW, bounds the closure to the east and is at the crest of the structure.

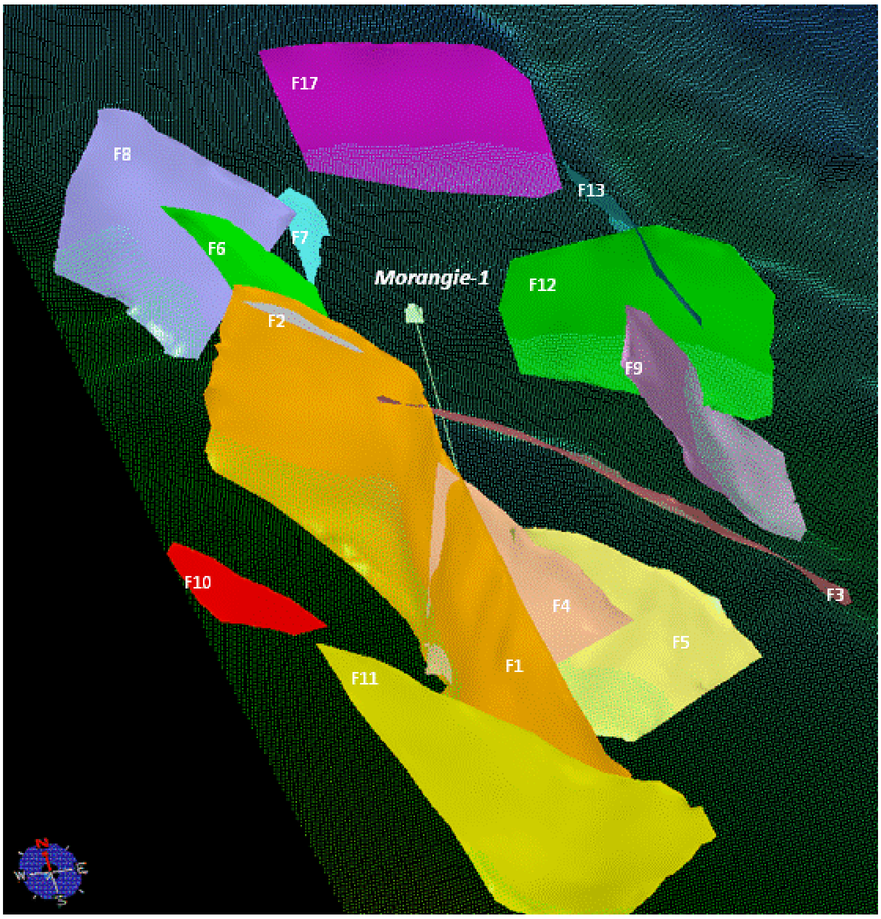

Figure 50: Permian faults for the geomechanical fault seal prediction and top reservoir structure. Fault labels refer to the geomechanical fault seal prediction (5.1); different labels are used for the geomechanical deformation modelling (5.2).

5.1.1 FRACTURE STABILITY

In the modelled stress regime the overall trends reflect an average-high likelihood of fault shear failure for faults oriented in the NE direction and a low-average likelihood of fault shear failure for faults oriented in the NW direction (Figure 51). Using a cohesive strength of 1 MPa and an internal coefficient of friction of 0.3 (i.e. case of low rock strength and low internal coefficient of friction favouring failure, Figure 51A and Figure 52), the fluid pressure would need to be approximately 35-50% higher than the estimated pore pressure to induce failure on most of the NW trending faults, including the main trap bounding fault (fault F3; black crosses in Figure 51A). This represents an increase of 8 to 11 MPa. Fault F1, bounding the reservoir to the west, shows a decrease in fracture stability in the vicinity of the Morangie closure (black arrow in Figure 52B).

Using a cohesive strength of 5 MPa and an internal coefficient of friction of 0.6 (i.e. case of higher rock strength and higher internal coefficient of friction hindering failure, Figure 51B and Figure 53), the fluid pressure would need to be approximately 90-100% higher to induce failure on most of the NNW trending faults, including the main trap bounding fault F3 (black crosses in Figure 51B). Most of the faults in the model that are oriented NW require a similar range of pore pressure increase, between 15-22 MPa, to be forced into failure. Therefore the fracture stability for such rock properties and stress regime is mostly influenced by the depth (Figure 53).

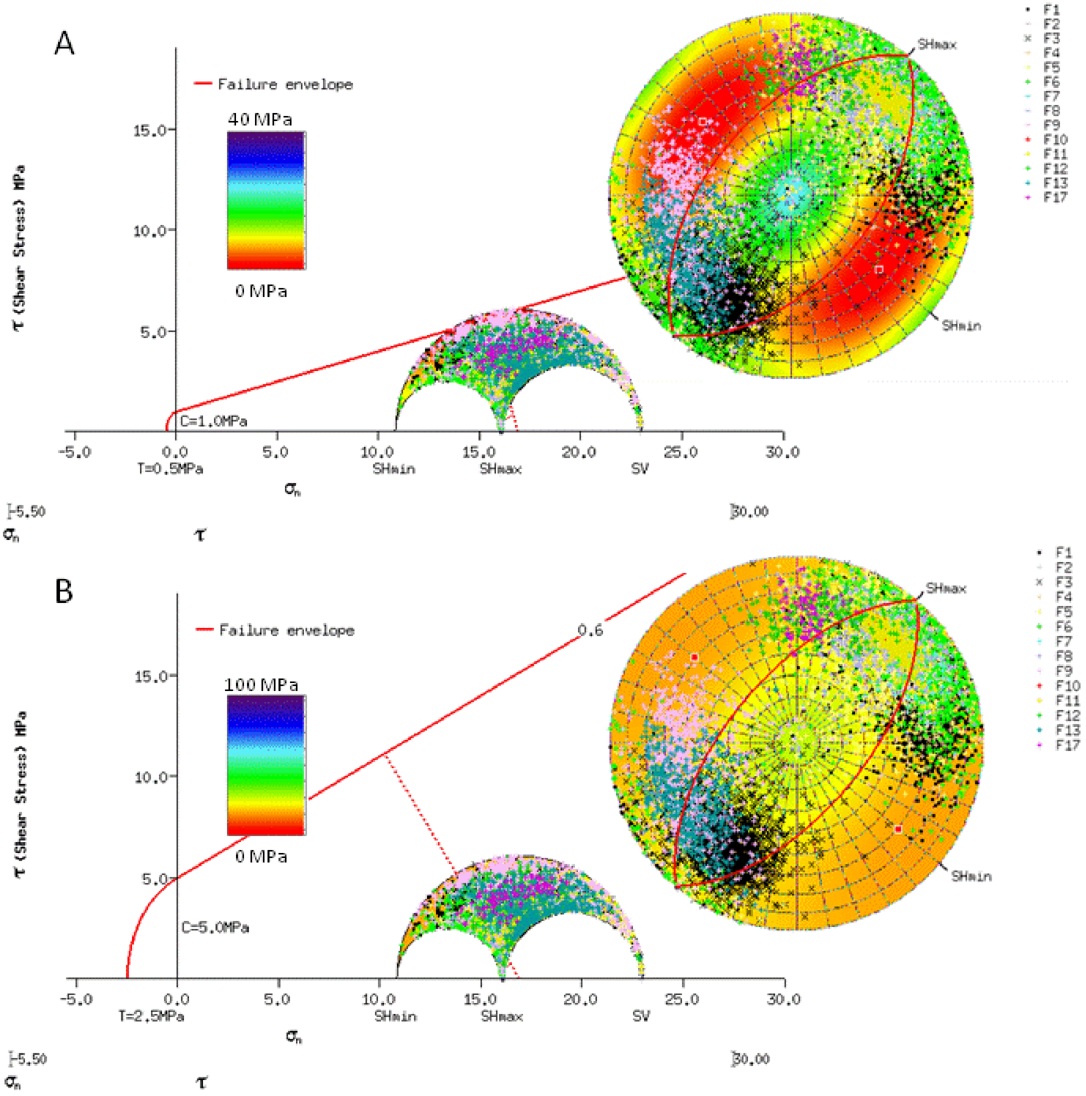

Figure 51: Fracture stability for the Permian faults at 1900 m below ground elevation (including 300 m of eroded sediments; chosen as this is the approximate depth of the top Permian reservoir during Middle Jurassic to Early Cretaceous extension and prior to Early Cretaceous erosion). The values on the stereonets (right) refer to the increase in pore pressure required to force the fault plane into failure; the same values are shown on the Mohr circle (left) with the failure envelop (red) defined by the fault rock properties. (A) Cohesive strength of 1 MPa and coefficient of internal friction of 0.3. (B) Cohesive strength of 5 MPa and coefficient of internal friction of 0.6.

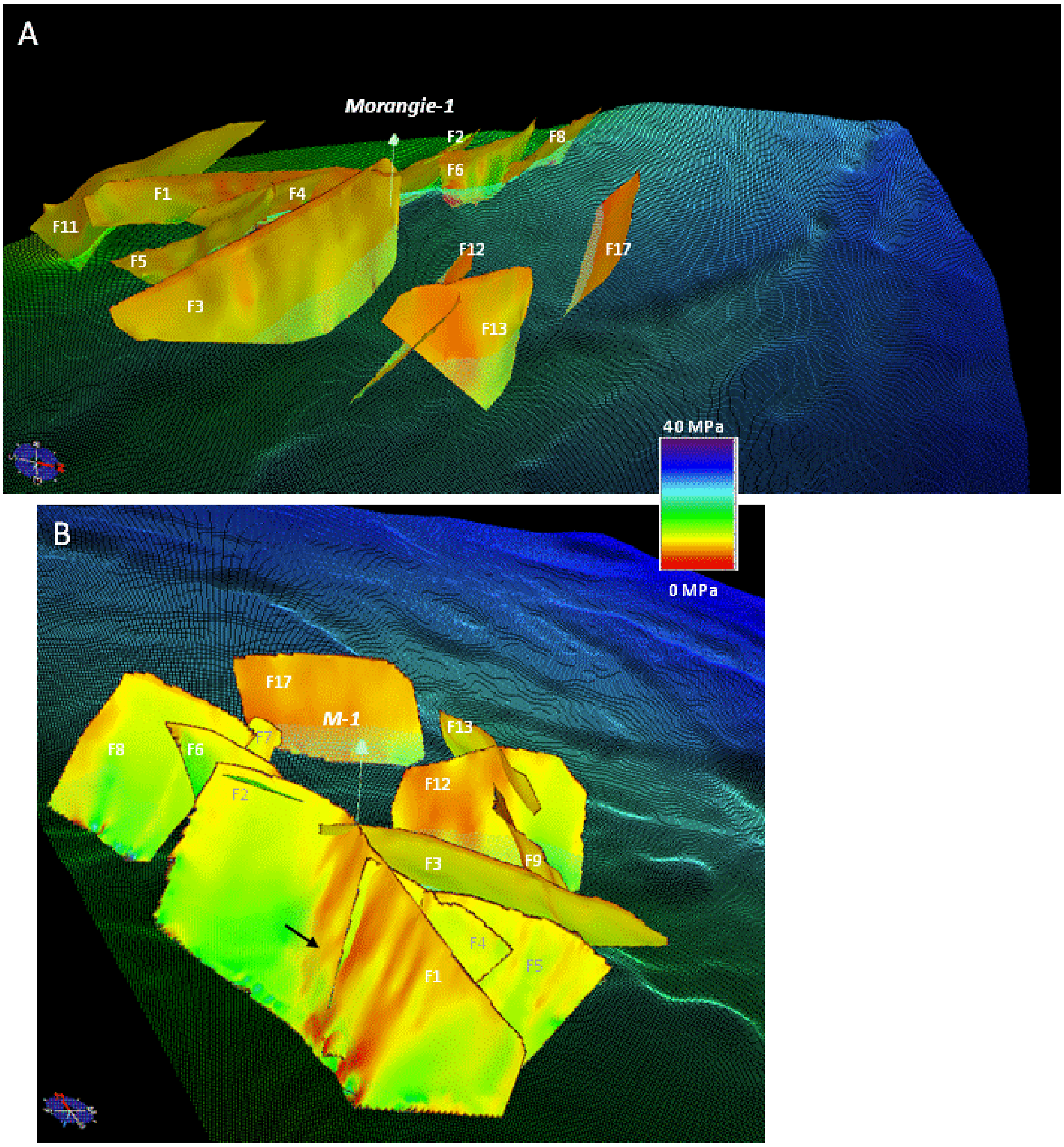

Figure 52: Fracture stability distribution for a (cohesive strength of 1 MPa and an internal coefficient of friction of 0.3). Maximum fracture stability is blue and minimum fracture stability red. The top reservoir surface is coloured for depth. (A) View from the east. (B) View for the south-west, the black arrow shows a decrease of fracture stability near Morangie-1.

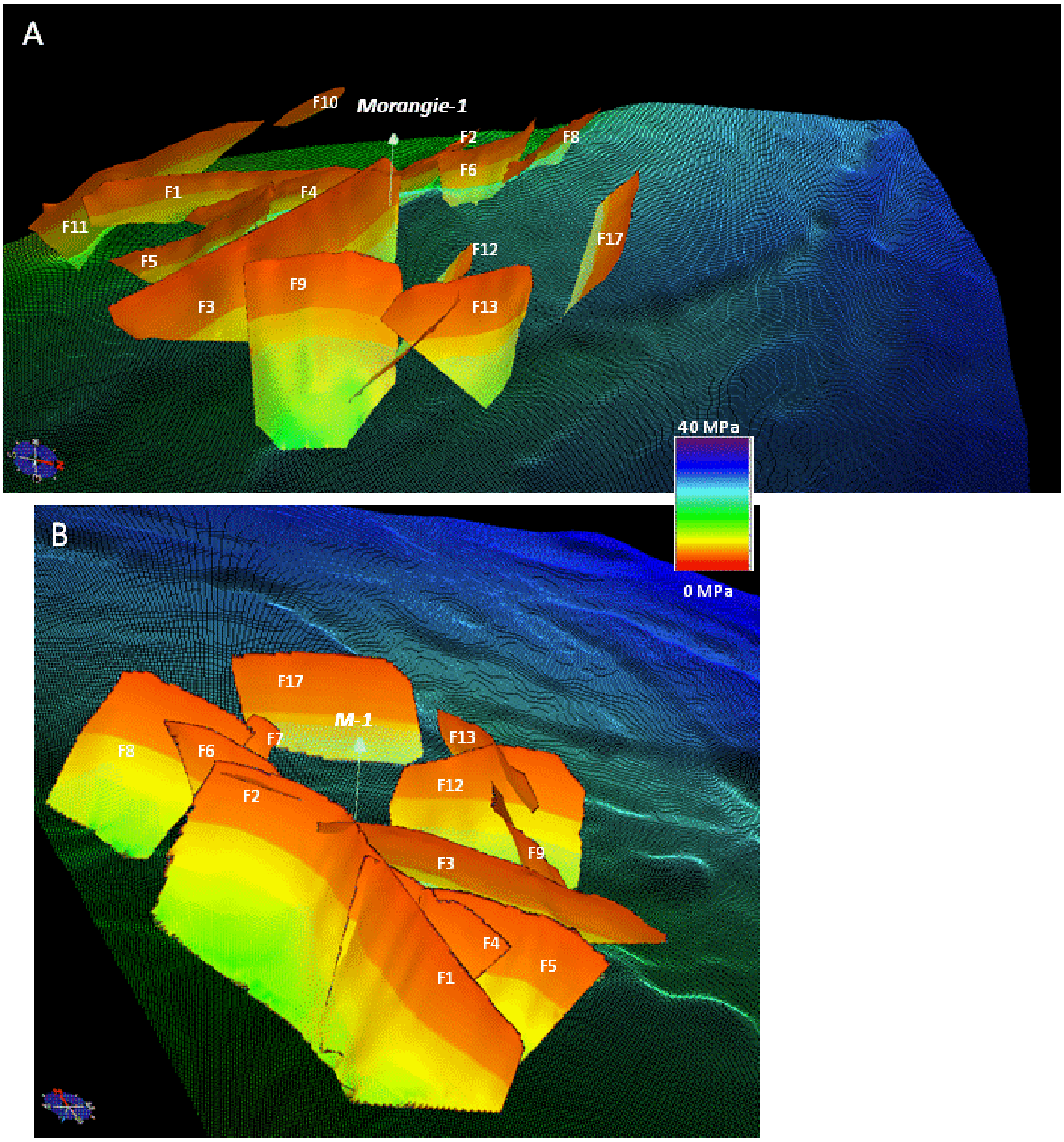

Figure 53: Fracture stability distribution (cohesive strength of 5 MPa and an internal coefficient of friction of 0.6). Maximum fracture stability is blue and minimum fracture stability red. The top reservoir surface is coloured for depth. (A) View from the east. (B) View for the south-west.

5.1.2 SLIP STABILITY

As with fracture stability, the slip stability shows that there is a higher likelihood of fault shear failure for faults oriented to the NE (Figure 54). With a coefficient of internal fiction of 0.48 most of the NNW trending faults would require a 50% increase in the fluid pressure to induce failure. That is, the pore pressure would need an increase of about 10 MPa on these faults. While the F1 fault bounding the closure to the west (i.e. down-dip of the trap crest) includes several segments with high likelihood of reactivation, the F3 fault at the crest of the structure is mostly associated with an intermediate likelihood of reactivation (Figure 54).

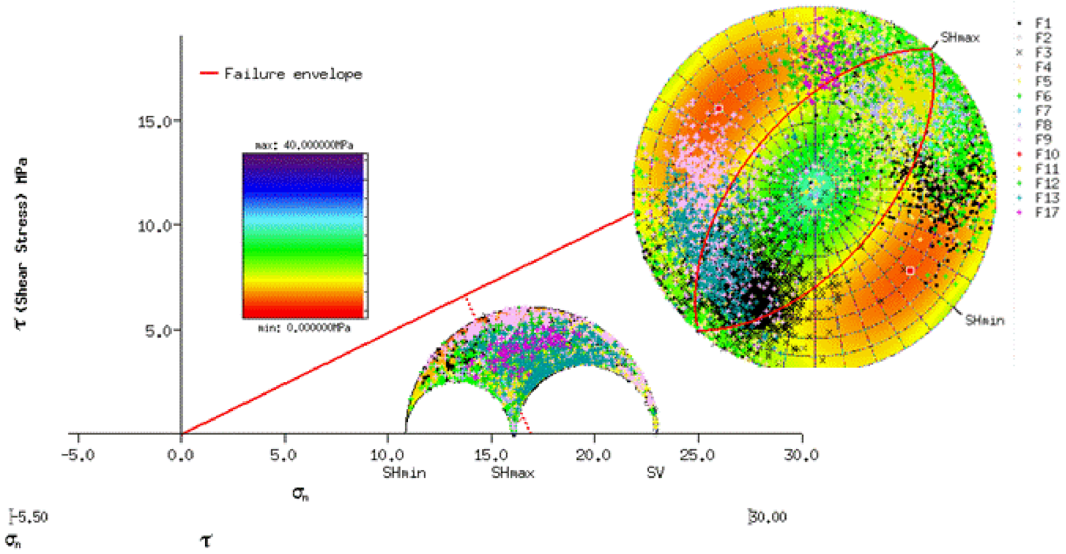

Figure 54: Slip stability for the Permian faults at 1900 m below ground elevation (including 300 m of eroded sediments). Faults are cohesionless and coefficient of internal friction is 0.48. The values on the stereonets (right) refer to the increase in pore pressure required to force the fault plane into failure; the same values are shown on the Mohr circle (left) with the failure envelop (red) defined by the fault properties.

5.1.3 SLIP TENDENCY

Like the fracture and slip stability, the slip tendency shows that most of the NE trending fault segments are not optimally oriented to slip (average slip tendency value <0.2; Figure 55). However, under this stress regime a higher tendency is expected for faults segments trending more to the north and the east. Faults F1 and F3, that bound the Morangie trap, include segments with increased slip tendency (c. 0.25-0.6; white arrows on Figure 56).

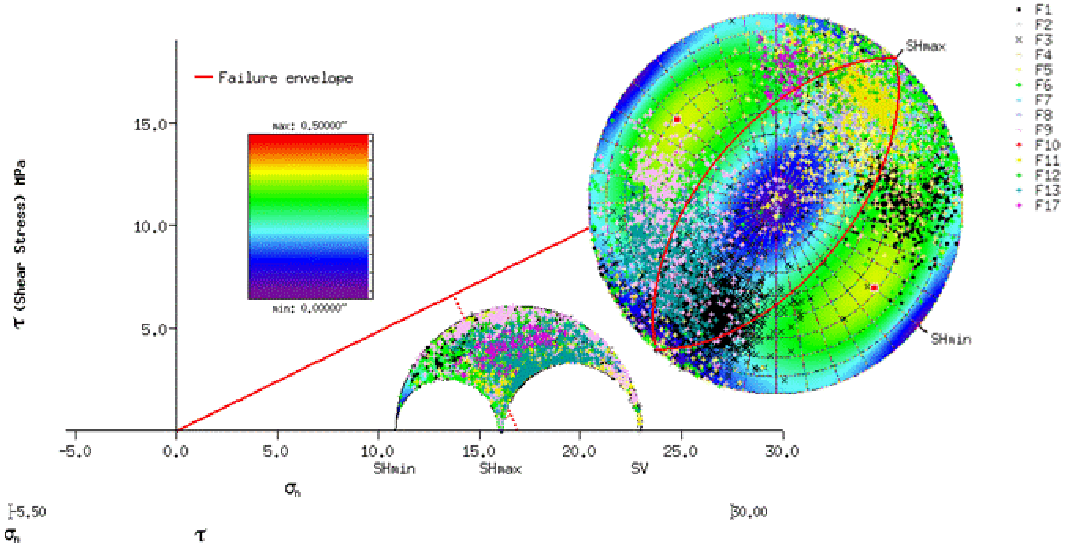

Figure 55: Slip tendency for the Permian faults at 1900 m below ground elevation (including 300 m of eroded sediments). The values on the stereonets (right) refer to the likelihood of slip to occur; the same values are shown on the Mohr circle (left).

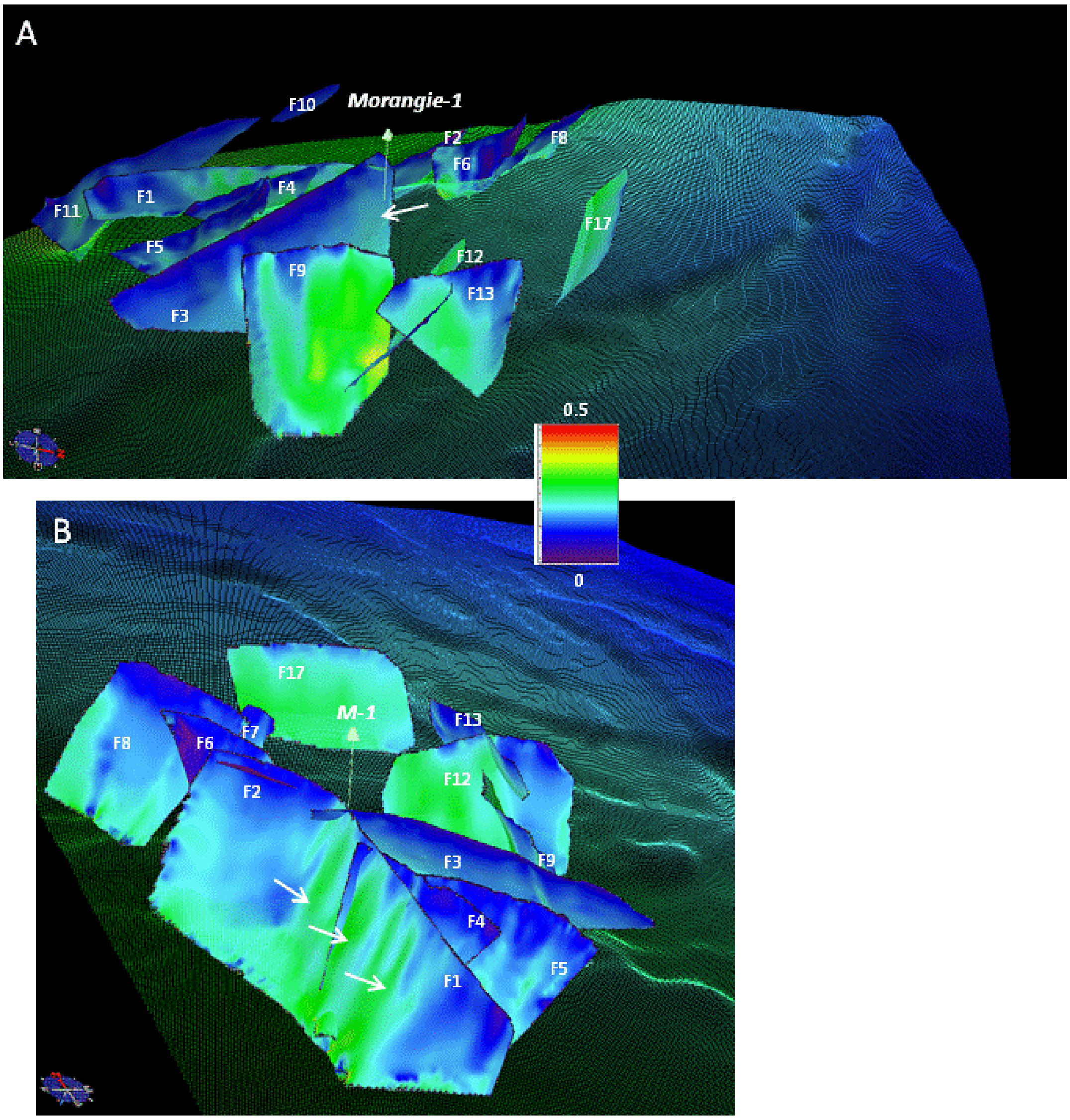

Figure 56: Slip tendency distribution. Maximum slip tendency is red and minimum slip tendency is blue. The top reservoir surface is coloured for depth. Areas of higher slip tendency (white arrows) are present on the trap-bounding faults F3 (at the trap crest) and F1 (down-dip of the trap crest). The top reservoir surface is coloured for depth. (A) View from the east. (B) View from the south-west.

5.1.4 DILATION TENDENCY

Like the fracture/slip stability and the slip tendency the most significant part of this analysis is that the dilation tendency is orientation dependent with the highest tendency values coinciding with steeply dipping NE oriented fault surfaces (Figure 57 and Figure 58). Parts of the trap bounding faults in the vicinity of the Morangie-1 have higher dilation tendencies. F1 dilation tendency is above 0.7 where it trends N (black dots on Figure 57 and white arrows on Figure 58B), indicating an important risk of dilation and up-fault flow; F3 dilation tendency is around 0.6 where it tends WNW (black crosses on Figure 57), indicating an average risk of dilation and up-fault flow.

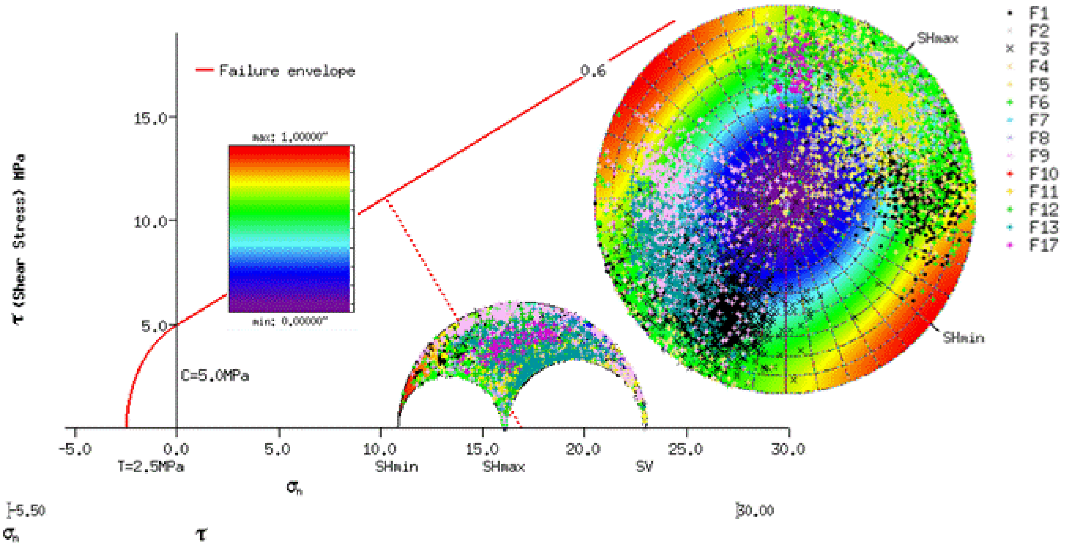

Figure 57: Dilation tendency distribution. The values on the stereonets (right) refer to the likelihood of dilation to occur; the same values are shown on the Mohr circle (left).

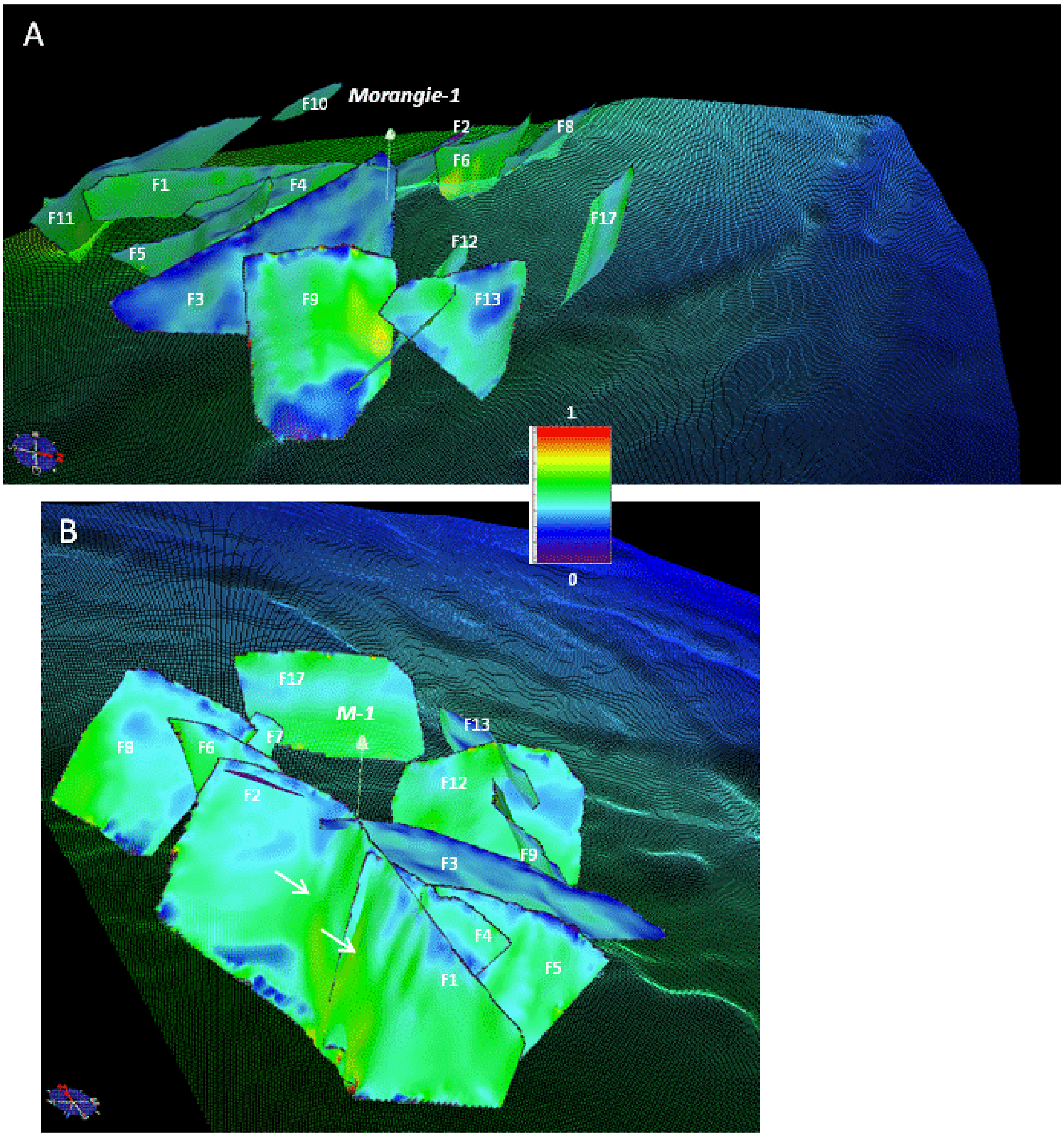

Figure 58: Dilation tendency distribution. Maximum dilation tendency is red and minimum dilation tendency is blue. The top reservoir surface is coloured for depth. (A) View from the east. (B) View from the south-west.

5.2 Geomechanical deformation modelling – Morangie

The Morangie deformation model architecture, material properties and boundary conditions are described in sections 2.2.1, 2.2.2 and 2.2.3, respectively.

5.2.1 STRAIN DISTRIBUTION

The modelling shows that fault size, strike, orientation and lateral fault connection relationship primarily influence the partitioning of reactivation shear and volumetric strains (Figure 59 and Figure 60). While longer faults are still more important strain-accommodating structures than shorter faults, there is heterogeneous strain distribution and this generally correlates with variation of fault strike orientation and with fault intersections.

Fault F1 (Figure 59 and Figure 60) accommodates most of the reactivation strain due to its size and its orientation to the NNW. However shear and volumetric strain loci develop at the triple junctions between faults F1 and F2 and F1 and F3, suggesting fault intersections are generally associated with strong strain localization. Shear and volumteric strain loci associated with the junction of F1 and F3 directly affect the Morangie structure with shear strain >0.15 on F3 in the close vicinity of the trap crest and volumetric strain >2.5%. The part of the F1fault bounding the Morangie structure to the west (down-dip of the trap crest) also shows similar high shear and volumteric strain values (Figure 61). It needs to be noted that F3 is overall a weakly reactivated fault with low strain due to its NW strike orientation (unfavorable for reactivation), except for its NW portion that is affected by its intersection with F1.

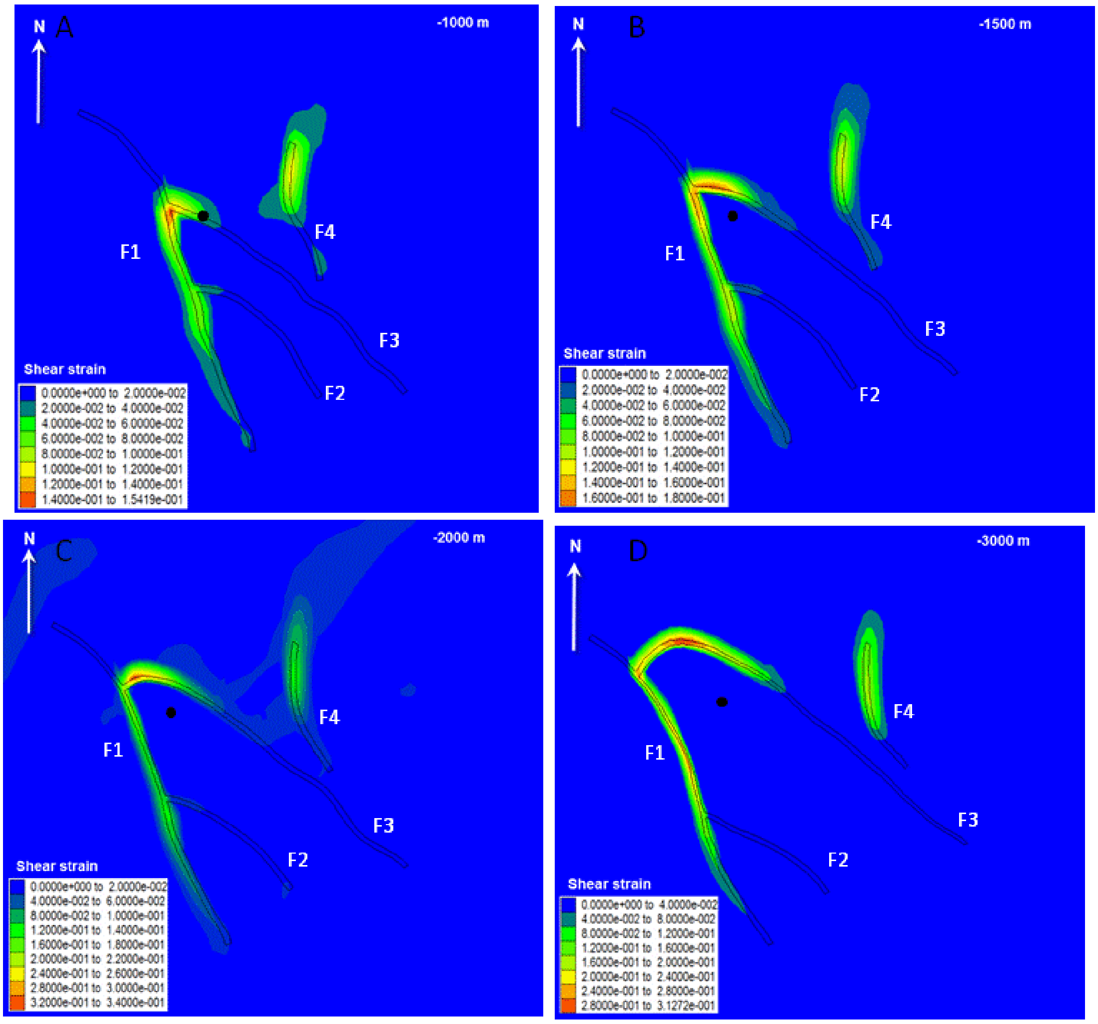

Figure 59: Shear strain distribution in plan view after 2% extension. Maximum strain is red and minimum strain is blue. (A) Horizontal slice at 1000 m below ground elevation. (B) Horizontal slice at 1500 m below elevation. (C) Horizontal slice at 2000 m below elevation, i.e. near top reservoir level. (D) Horizontal slice at 3000 m below ground elevation. Black dot is Morangie-1 location.

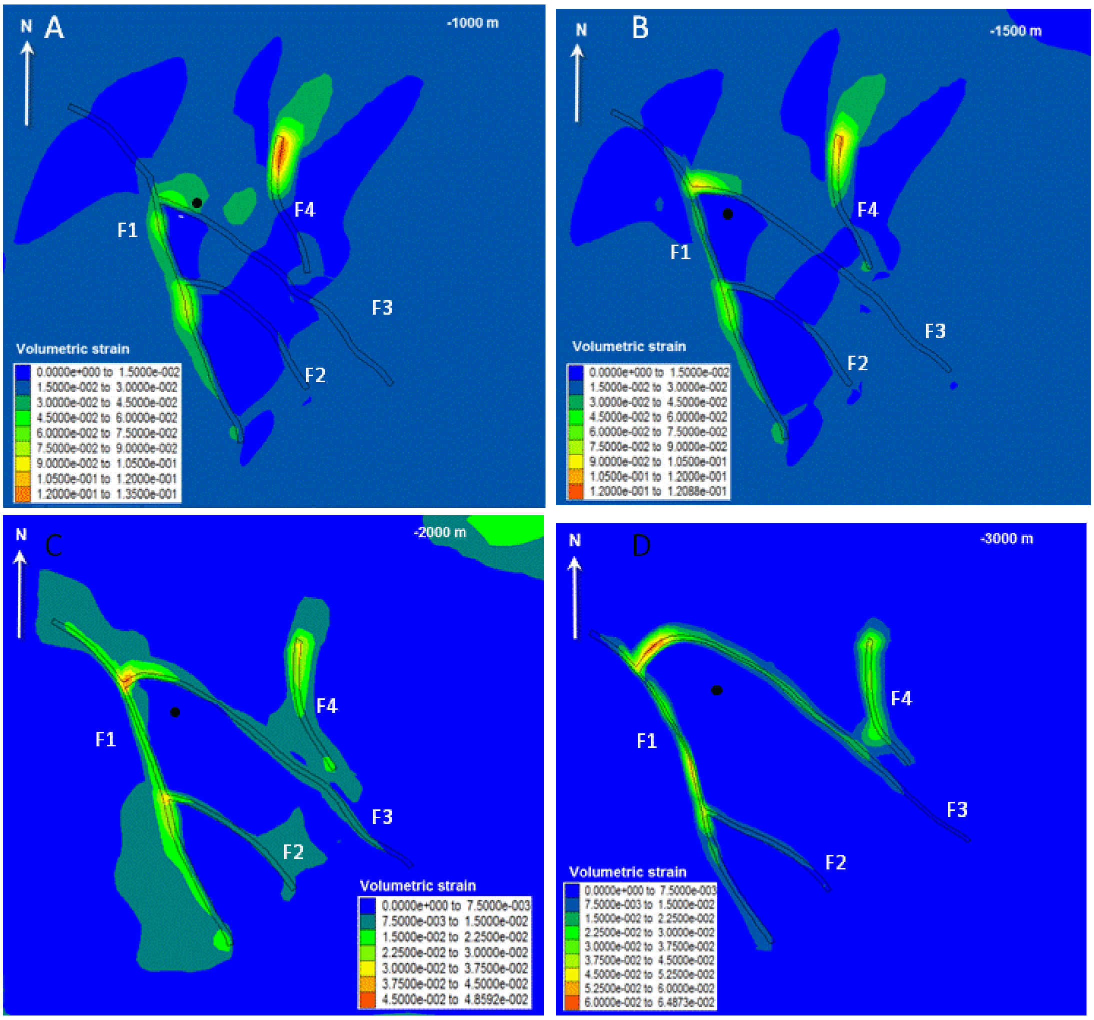

Figure 60: Volumetric strain distribution in plan view after 2% extension. Maximum strain is red and minimum strain is blue. (A) Horizontal slice at 1000 m below ground elevation. (B) Horizontal slice at 1500 m below ground elevation. (C) Horizontal slice at 2000 m below ground elevation, i.e. near top reservoir level. (D) Horizontal slice at 3000 m below ground elevation. Black dot is Morangie-1 location.

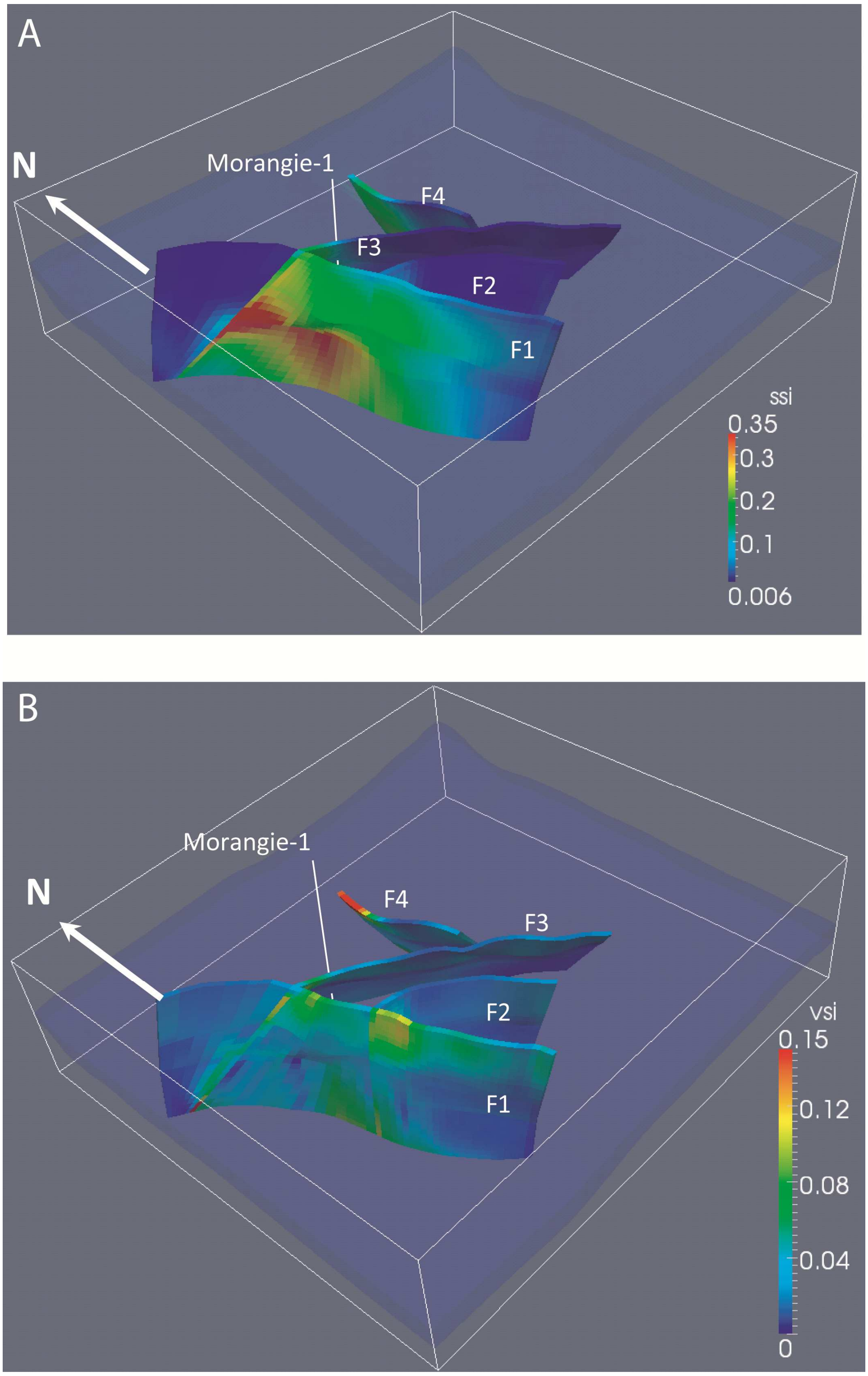

Figure 61: 3D distribution of shear strain (A) and volumetric strain (B). Maximum strain is red and minimum strain is blue.

5.2.2 STRESS DISTRIBUTION

Patterns of mean stresses and shear stresses at 1500 m below ground elevation are shown in Figure 62. The stress patterns are broadly consistent with those for the Cliff Head and Dunsborough/Lilac models. Lower mean and shears stresses generally develop within and around reactivated fault zones, with higher shear stresses found near fault tips (Figure 62B). The Morangie model roughly shows the presence of lower mean stresses and shear stresses in the hanging-wall side of faults. However, fault intersection and fault interaction perturbs the stress distribution. Taking fault F1 , for example, lower mean stresses developed in the central-south section of F1's hanging-wall areas, but this pattern changes toward the location of its intersection with F3, where lower mean stresses occur at the hanging-wall side of F3 near its intersection with F1 (Figure 62A). The shear stress pattern along F1 also reflects the influence of, and interaction with, faults F2 and F3.

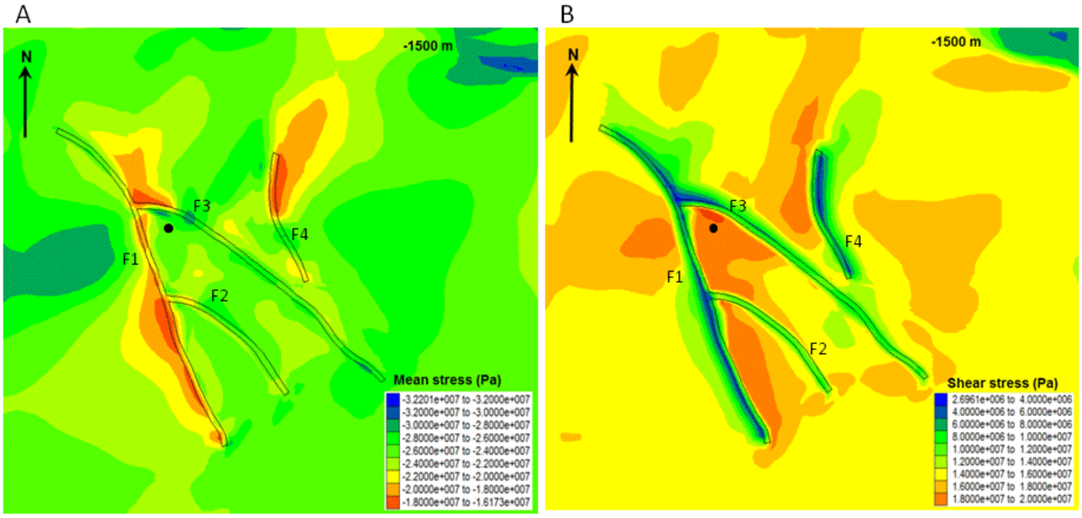

Figure 62: Plan-view stress patterns for a horizon of -1500 meter depth in the model for the Morangie field. (A) Mean stress. (B) Shear stress. F1-F4 denotes fault traces. For mean stresses, negative values denote compressive stresses. Shear stresses all have positive values. Black dot is Morangie-1 location.

5.3 Discussion – Morangie

The palaeo-charge reconstruction data show that the Morangie structure hosted at least a 52 m palaeo-oil column (Appendix A and Figure 73). The crest of the trap is bounded by fault F3 to the east and north-east (Figure 63A). A schematic palaeo-field reconstruction, based on the present-day trap geometry (Figure 63B), shows that the F1 fault also supports a part of the palaeo-accumulation. The development of leakage along faults F1 and F3 due to the accommodation of shear and volumetric reactivation strains of >0.15% and >2.5%, respectively, could adequately explain the total loss of hydrocarbon in the structure. This mechanical behaviour is likely driven by the size of the F1 fault and the presence of the triple junction between F1and F3 that concentrates deformation and structural permeability during the Middle Jurassic to Early Cretaceous reactivation.

The geomechanical fault seal prediction models (see 5.1) do not show major evidence of failure likelihood for the northern end of F3 fault, although a slight increase in slip tendency is recorded (Figure 56A). The part of F1 supporting the palaeo-accumulation shows slip tendency values >0.3 (Figure 56B) and dilation tendency values >0.6 (Figure 58B), further suggesting the likelihood of structural permeability increase and up-fault leakage at this location.

In summary the outcomes from the *geomechanical deformation* (5.1) and the *geomechanical fault seal prediction* (5.2) models suggest that the loss of the hydrocarbon accumulation in the Morangie structure is due to (i) the strain accommodated by the NNW-trending F1 fault and (ii) the fault intersection in the vicinity of the Morangie structure resulting in a concentration of shear deformation and dilation.

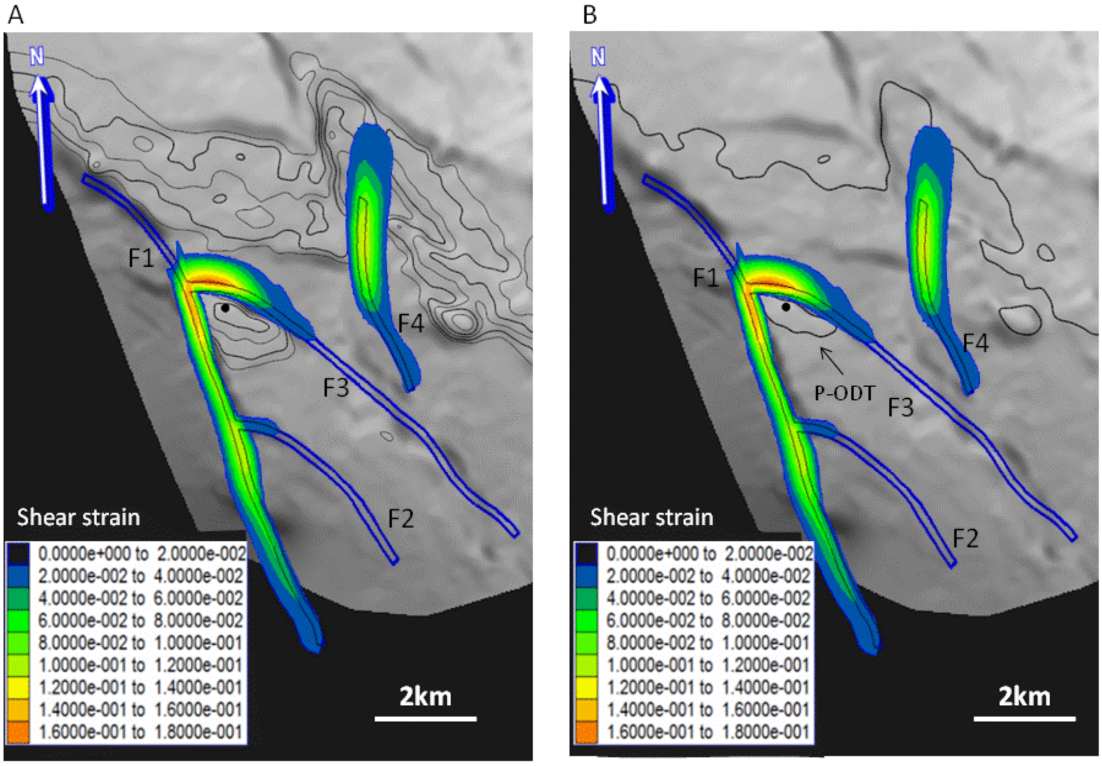

Figure 63: Relationship between shear strain distributions, geometry and charge history for the Morangie structure. Maximum strain is red and minimum strain is blue. (A) Shear strain distribution and present-day structure. Isolines are form 2050 mSS to 2250 mSS. (B) Shear strain distribution and palaeo-oil column down to c. 2160 mRT (c. 2130 mSS). Black dot is Morangie-1 location.

6 TRAP INTERGITY RISK FACTORS IN THE NORTHERN PERTH BASIN

Assessment of up-fault fluid flow is aimed at identifying the potential for a hydrocarbon trap's top seal to have been breached, either by large-scale faulting, during fault reactivation, or by associated fracture permeability. Active faults intersecting a caprock are often cited as zones of critical, fracture network permeability whereas inactive or non-critically stressed faults are thought to act as barriers to fluid flow (e.g. Sibson, 1987; Muir-Wood and King, 1993; Anderson et al., 1994; O'Brien et al., 1999; Sanderson and Zhang, 1999; Wiprut and Zoback, 2000; Wilkins and Naruk, 2007).

The geomechanical models presented in this study suggest that the main geometric factor controlling the accommodation of reactivation strain along faults is the fault orientation. Fault planes and segments with orientations between NNW (~340°) and ESE (~100°) are more likely to be forced into failure under the NW extensional stress field modelled for the Middle Jurassic to Early Cretaceous, while faults that trend NW are more prone to seal. This relationship in the distribution of fault seal risk, based on fault orientation inferred from the modelling results, is shown in Figure 64. In addition to the structures modelled in this report, the orientation of trap bounding faults in 12 other drilled prospects in the offshore northern Perth Basin are shown in Figure 65: 6 with inferred breach - red dots; 4 with no oil shows - orange dots and 2 with present-day gas and palaeo oil column suggesting either a sealing or healed fault - green/red dots. Six breach traps fall within the "high risk" or "transition" zones (Morangie, Livet, Hadda, Leander Reef, Vindara, Lilac and Geelvink). Flying Foam is the only breach trap whose bounding fault orientation is within the "low risk zone"; however the fault includes a NNE-trending jog (Flying Foam jog on Figure 65) adjacent to the closure that might represent a leak point. The "transition zone", which covers the main regional fault orientation (NW to NNW, or 320° - 340°), includes either dry and breach prospects or discoveries. This suggests that additional factors, other than the fault orientation alone (e.g. fault length triggering strain partitioning, fault intersections), have a bearing on fault sealing potential.

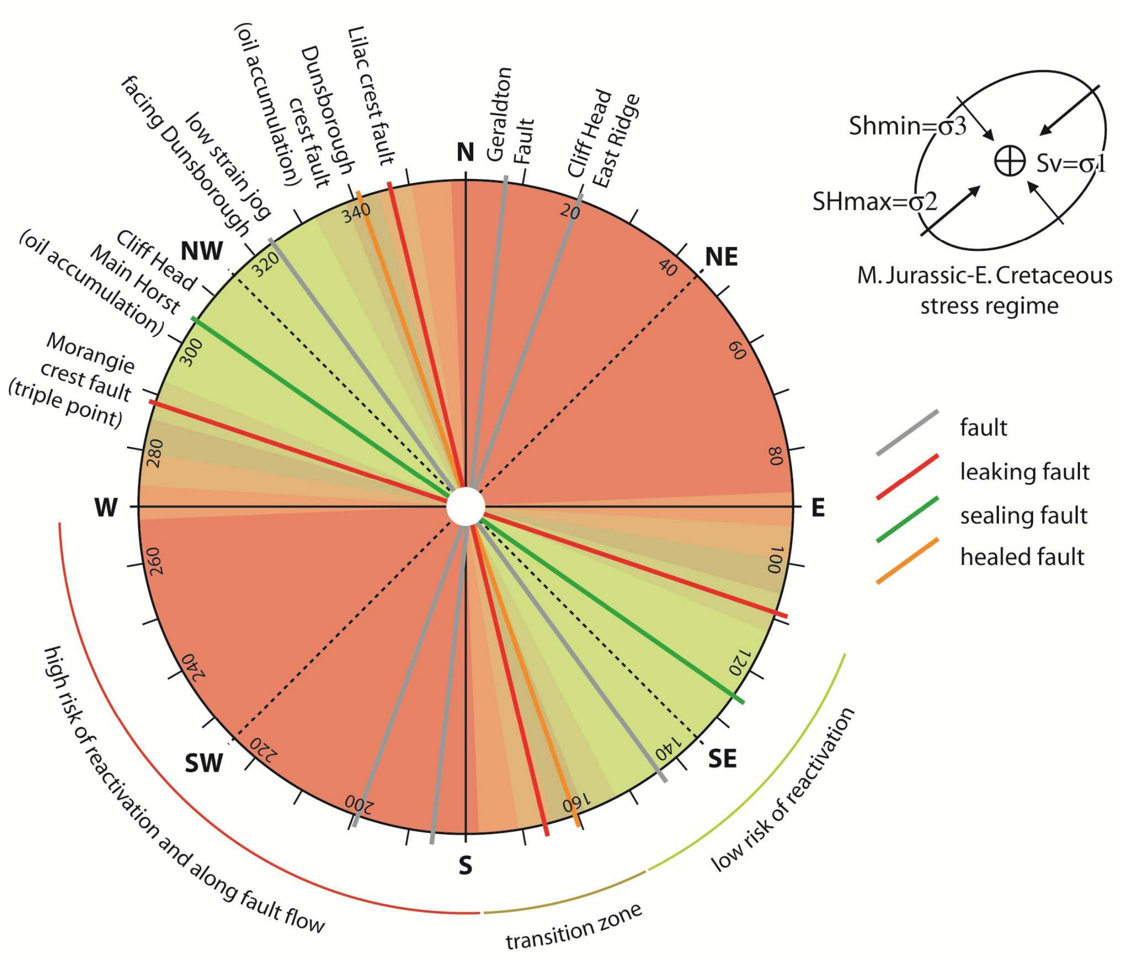

Figure 64: Fault seal risk based on fault orientation for the fields and prospects modelled. Integrated geomechanical fault seal prediction, geomechanical deformation models and charge data suggest that fault planes oriented between the NNW (~340°) and ESE (~100°) are likely to reactivate under the Middle Jurassic to Early Cretaceous stress regime (upper right) and allow fluid flow. Sealing and leaking faults from the modelled areas are plotted (green and red respectively). Note that the WNW oriented segment of the fault bounding the dry Morangie structure lies within the low risk area although along fault leakage was possible. In this case the intersection of fault planes (and not the fault orientation) was probably the driving factor for fault reactivation and top seal bypass.

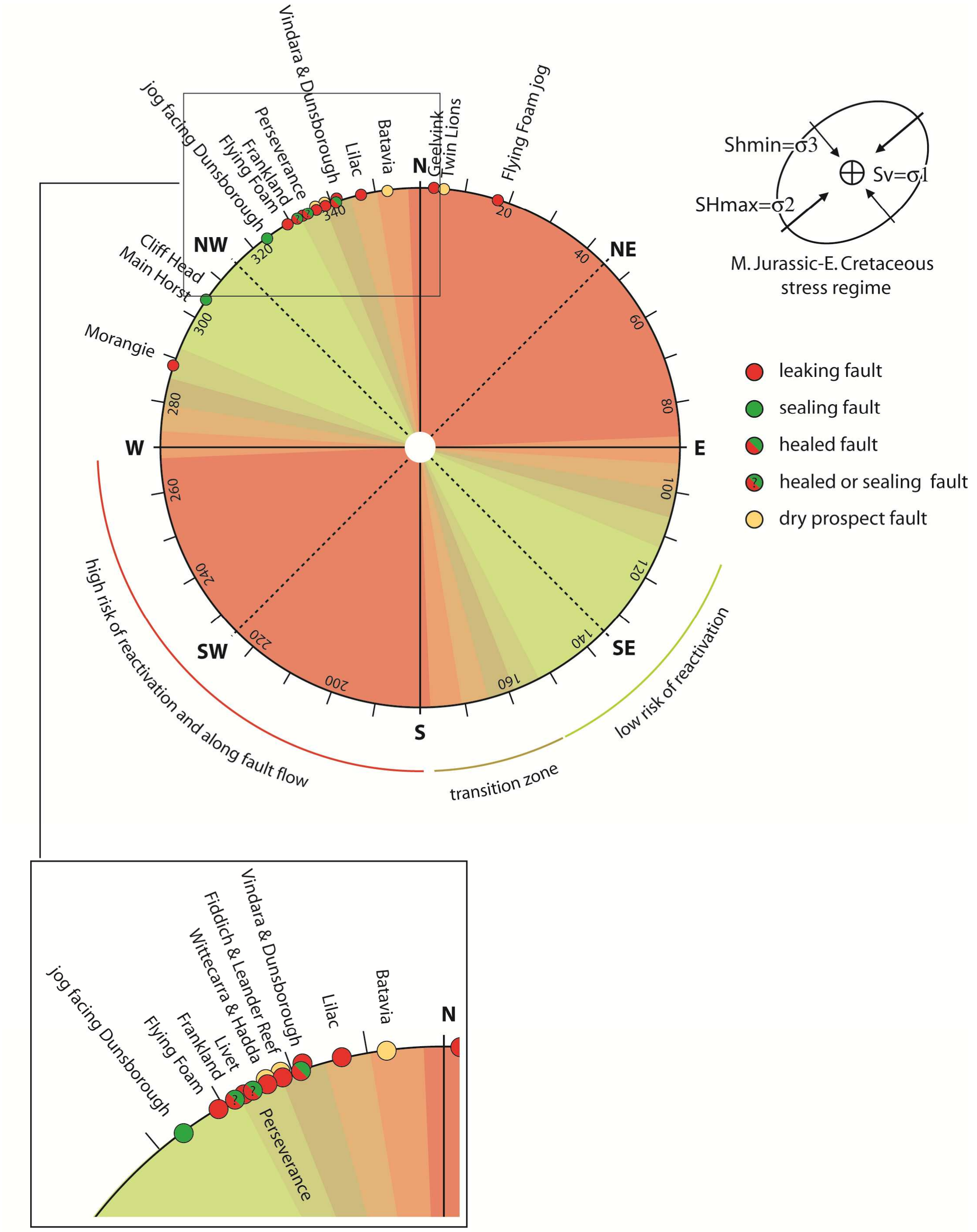

Figure 65: Comparison between the fault seal risk and the orientation of trap bounding faults in the offshore northern Perth Basin. The main trap bounding faults are identified by their orientation. Green dots refer to faults bounding current accumulations (i.e. sealing fault); red dots refer to faults that offset the top seal and bound dry structures with a palaeo accumulation (i.e. top seal bypass and along fault fluid flow is the suggested cause of leakage), red/green dot refers to faults with indication of leakage and currently holding a hydrocarbon column (healed fault), orange dots refer to faults bounding dry structure with no oil show (lack of charge or undetected migration pathway?), red/green dots with question mark refer to faults bounding a gas accumulation with a palaeo oil column resulting either from oil displaced by gas or oil leaked along the fault plane. Note the leaking faults are mostly orientated between the NNW (335°) and the NNE (20°), which correlates with the

risk prediction form the geomechanical models. Faults oriented to the NNW (i.e. 330° - 340°) in the transition zone between high and low reactivation risk - can either seal or leak. Faults oriented to the NW are likely to seal.

The partitioning of strain on trap bounding faults during the Middle Jurassic to Early Cretaceous extension represents a key factor for the prediction of top seal breach and the risk to trap integrity due to up-fault leakage. The models show a strong correlation between the initial fault strike length and the predicted amount of accumulated strain, with longer faults predicted to accommodate more strain. This behaviour creates “shielded areas”, where prospect faults that are optimally oriented for failure do not accommodate critical strain because a neighbouring larger fault preferentially accommodates the bulk of deformation (e.g. fault F2, bounding the Dunsborough Field, shielded by fault F1 to its west; Figure 38 and Figure 39). Similar behaviour has been reported from the Timor Sea (Meyer et al., 2002; Langhi et al., 2010), where reactivation strain tends to progressively localize onto the largest faults over time. The Cliff Head Field also represents an example of a structure shielded by the Geraldton Fault.

Although primarily controlled by the fault length, strain partitioning can be affected by other parameters such as local variations in the fault orientation. The deformation modelling of the Dunsborough Field suggests that the presence of a NW-trending kink on fault F1 (Figure 38), results in a strong local decrease in shear and volumetric strain accommodation. This, in turn, results in increased shear and volumetric strain loci developing on the F2 fault opposite this NW segment, which potentially compromises its fault sealing potential.

The modelling results of the Morangie structure suggest that the intersection of trap bounding faults represents a key risk factor if it delimits the closure of an oil column. Here, the trap crest is bounded by a NW-trending fault segment with low-average risk of reactivation (Figure 65). However, the fault intersects a NNW-trending fault (Figure 50) which corresponds with a zone of high shear deformation and dilation (see 5.2). Similar fault architecture from the Skua oil field (Bonaparte Basin) is associated with a long-lived fluid conduit (Gartrell et al., 2004). Three out of six breach prospects lying in or near the “transition zone” between low and high risk of reactivation (Figure 65) show fault intersections along their trap crest bounding faults (i.e. Hadda, Flying Foam and Livet). This suggests that the shear deformation and dilation associated with fault intersection could locally facilitate the development of top seal bypass and result in trap breach despite individual fault orientations potentially being at a low risk of reactivation.

The distributions of shear and volumetric strains on the trap bounding faults for the Cliff Head, Dunsborough, Lilac and Morangie structures suggest that thresholds can be defined to differentiate between sealing and leaking faults (0.1 and 0.05 for shear and volumetric strain respectively; Figure 66). Values lower than the thresholds correlate with lower fault breach risk and higher fault sealing potentials; values higher than the thresholds correlate with higher fault breach risk and lower fault sealing potentials. Faults with shear and volumetric strain values around the thresholds might induce short term fault breach followed by fault self healing process as proposed for Dunsborough. Although these threshold values could be used locally for first order structural integrity predictions, cautions need to be taken if these predictions are to be applied to other areas with different stratigraphic architecture, pore pressure gradient and tectonic settings (i.e. bulk deformation, stress field orientation).

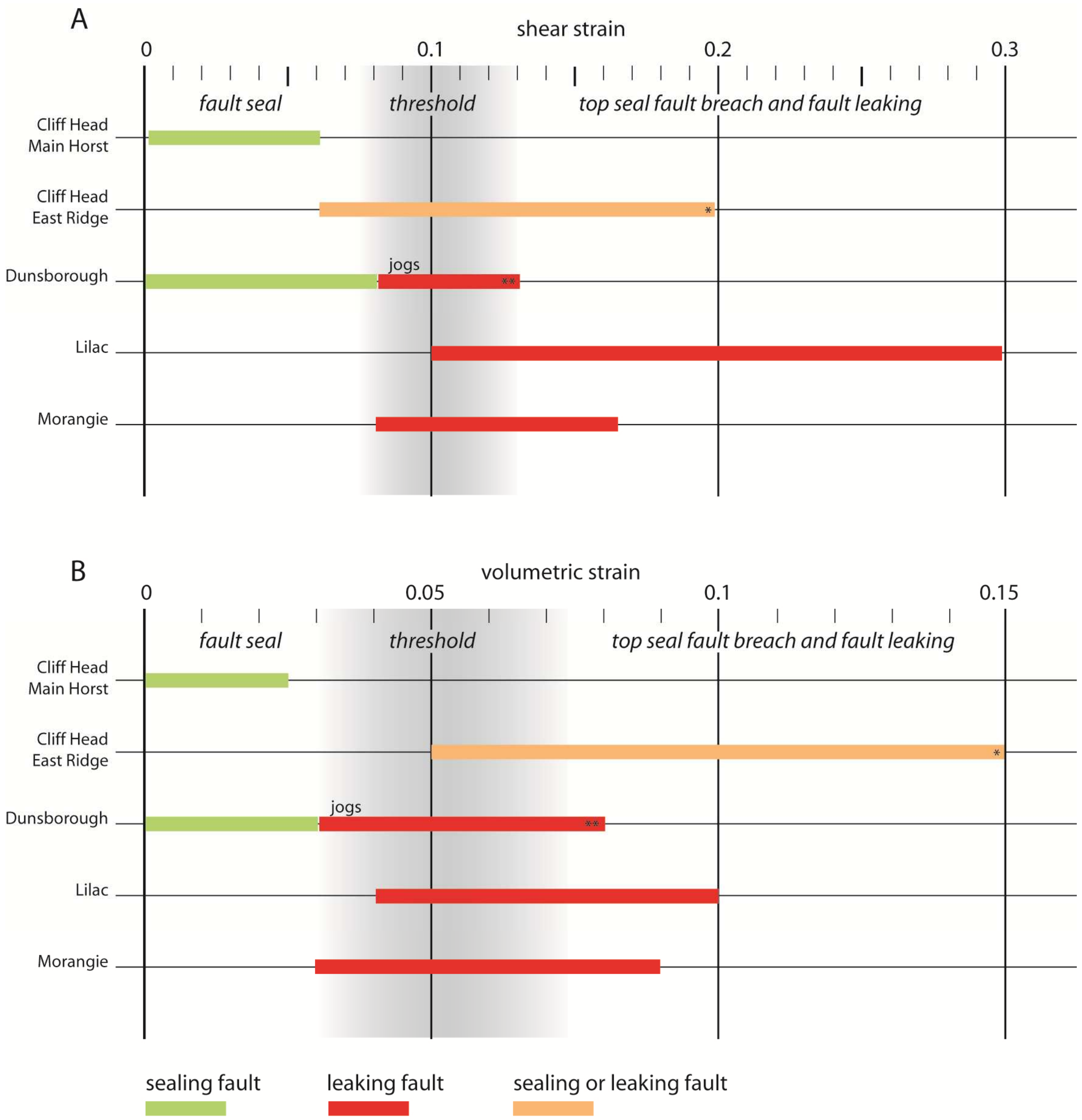

* It is unclear if the East Ridge was not charged or was charged and experienced later leakage.
** it is inferred that the jogs present on the Dinsborough trap bounding faults acted as pathways for leakage.

Figure 66: Strain distribution on trap bounding faults. (A) Shear strain from the trap bounding faults for the Cliff Head, Dunsborough, Lilac and Morangie structures. A threshold around 0.1 is proposed to differentiate between sealing faults and leaking fault breaching the top seal. Shear strain value near the threshold might induce short term fault breach followed by fault self healing process. (B) Volumetric strain from the trap bounding faults for the Cliff Head, Dunsborough, Lilac and Morangie structures. A threshold around 0.05 is proposed to differentiate between sealing faults and leaking fault breaching the top seal. Shear strain value near the threshold might induce short term fault breach followed by fault self healing process.

The fault growth history, derived from the fault throw distribution for the Cliff Head and Dunsborough/Lilac areas, suggests that Middle Jurassic to Early Cretaceous extension results in the nucleation of new sets of faults in the Late Jurassic sediments and the reactivation of the

Permian reservoir faults (Figure 26 and Figure 49). During deformation, Mesozoic faults propagate downward toward the top seal and the Permian faults reactivate and propagated upward within the top seal. This structural evolution can result in:

- Disconnected or soft-linked Mesozoic and Permian fault systems, as seen in Cliff Head (Figure 26) resulting in high trap integrity. The reactivation strain accommodated by both systems is not sufficient for the faults to propagate through the top seal; however deformation associated with fault tips may create complex subseismic deformation zones and, thereby increase vertical permeability through it.
- Hard-linked Mesozoic and Permian fault systems as seen in the Dunsborough/Lilac area (Figure 49), potentially resulting in lower trap integrity. The reactivation strain accommodated by both systems is sufficient for the faults to propagate through the top seal. The throw decreases locally near the top seal, where the Mesozoic and Permian faults link. This scenario could result in the development of a migration pathway if the fracture network is critically-stressed.

The evolution of shear strain and bulk extension for the Cliff Head faults shows that the Mesozoic faults accommodate more reactivation strain than the trap-bounding Permian faults. This suggests that–for that location at least–the risk of top seal breach is primarily related to the downwards propagation of the shallow Mesozoic faults. Therefore, the location of the nucleation sites for the Mesozoic faults plays a role for top seal bypass development. The greater the distance between the nucleation sites and the top of the seal, the more reactivation strain is required for the fault to propagate downward and affect the top seal.

The transition between soft- and hard-linkage is dictated by the ability of the top seal to accommodate strain by ductile processes and distributed fracture networks up to a certain threshold, beyond which brittle failure and formation of discrete fault planes begin to dominate. This process is partly controlled by the distribution of strain, which can be influenced by top seal thickness and geomechanical properties (i.e. a thicker and more ductile or incompetent seal would accommodate more strain before failing).

There are minimal variations in the thickness of the Kockatea Shale top seal in the offshore northern Perth Basin (Figure 67) –mostly between 250 m to 350 m thick in well intersections– and this does not appear to be a key risk factor for the development of hard-linked top seal bypass. Furthermore, those breached prospects with hard-linkage through the seal show no positive correlation with a thinner top seal (Figure 68). The top seal thicknesses over the existing discoveries are ~250-300 m (Cliff Head-1, -4, Dunsborough-1 and Perseverance-1) and ~140 m (Frankland-1), while the top seal thicknesses over the dry prospects with palaeo-accumulations range between ~250 m (Lilac-1) and ~370 m (Lilac-1 and Leander Reef-1) with an average of ~310 m. However, most of these breach structures show crest trap faults with either (i) a high risk of reactivation due to their orientations, and/or (ii) intersection of fault planes (Hadda, Flying Foam, Morangie, Livet).

In consideration of the geomechanical properties of the top-seal, the uniaxial compressive strength (UCS) and the brittleness index (BRI) were computed for Cliff Head-1 (oil discovery with soft-linkage through the seal), Dunsborough-2 (used as a proxy for the oil discovery in Dunsborough-1with hard-linkage through the seal), Perseverance-1 (gas discovery with hard-linkage through the seal), Lilac-1 (breach oil prospect with hard-linkage through the seal) and Flying Foam-1 (breach oil prospect with hard-linkage through the seal; Figure 69).

The top seal UCS is computed from sonic logs (Δt in μs/ft) using an empirical correlation given by Horsrud (2001);

$$UCS = 0.77(304.8/\Delta t)^{2.93}$$

the higher the UCS the more competent the facies. The BRI is defined as the ratio of the calculated UCS and the UCS of a normally consolidated rock derived from the in-situ effective pressure (Horseman, 1986); for BRI>2 the risk of embrittlement increases with increasing BRI. The results of this analysis show that there is no correlation between more competent/brittle facies and the development hard-linked seal bypass. At the Cliff Head oilfield, soft-linkage occurs into the Kockatea Shales seal although the UCS and the BRI are equal or higher than other locations where hard-linkage exists. These data suggest that structural parameters are the primary risk factors for the development of seal bypass rather than shale thickness or geomechanical properties.

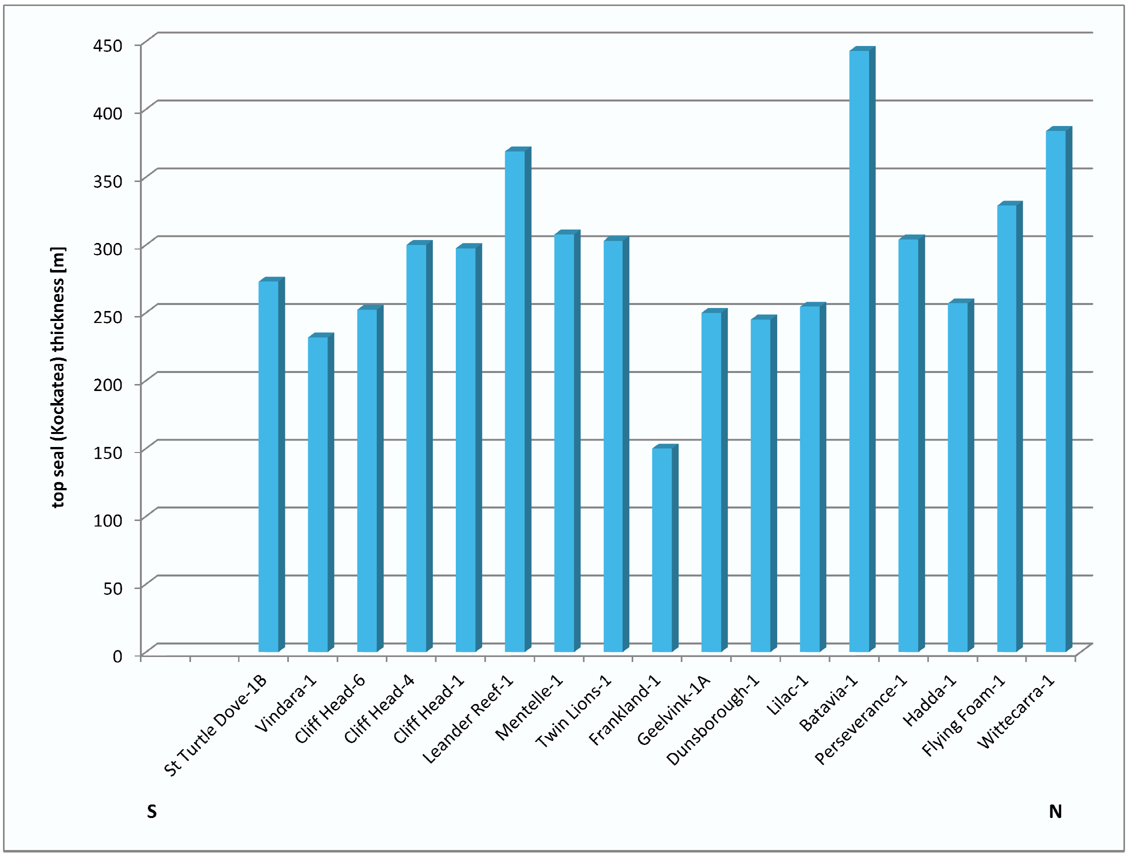

Figure 67: Top seal (Kockatea Shale) thickness in the offshore northern Perth Basin.

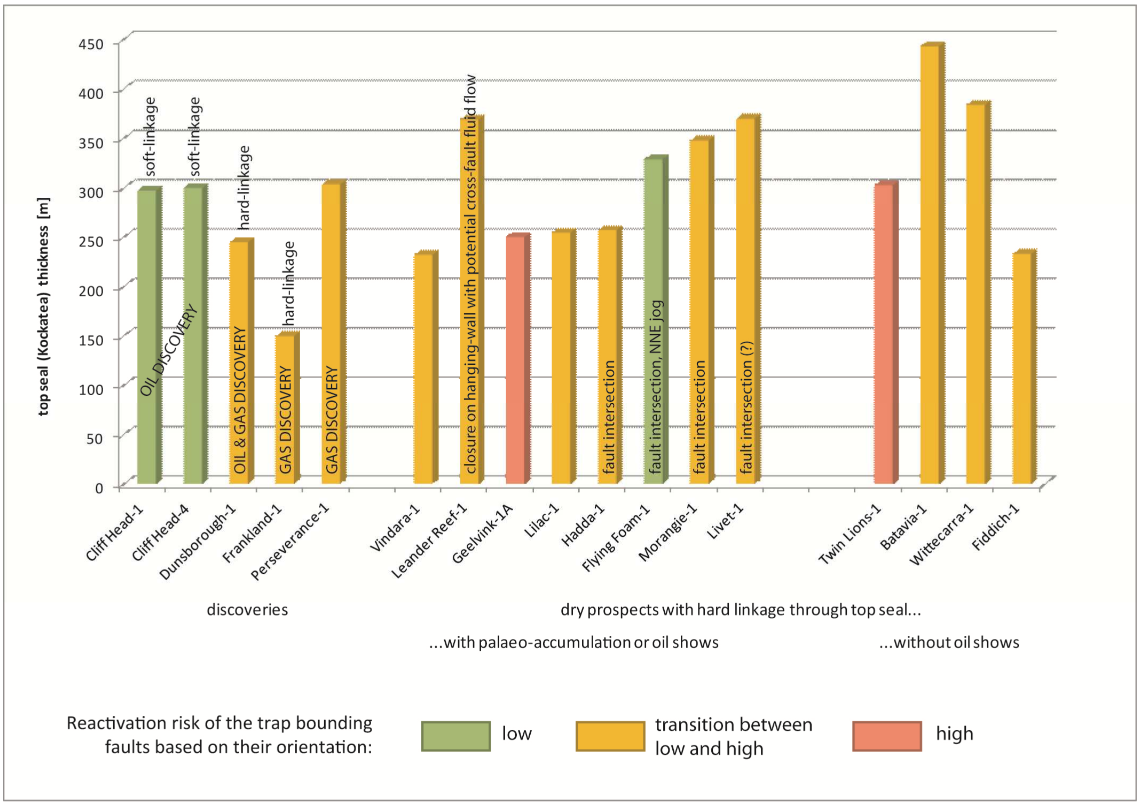

Figure 68: Comparison between top seal (Kockatea Shale) thickness and top seal bypass risks in the offshore northern Perth Basin. The group of wells on the left represents the four discoveries arranged form south to north. The group of wells in the middle represents dry structures with palaeo-accumulations and with along fault flow suggested as the cause of leakage. The group of wells on the right represents dry structures without oil shows. The bar colours refer to the risk of reactivation for the crest bounding faults as shown in Figure 65.

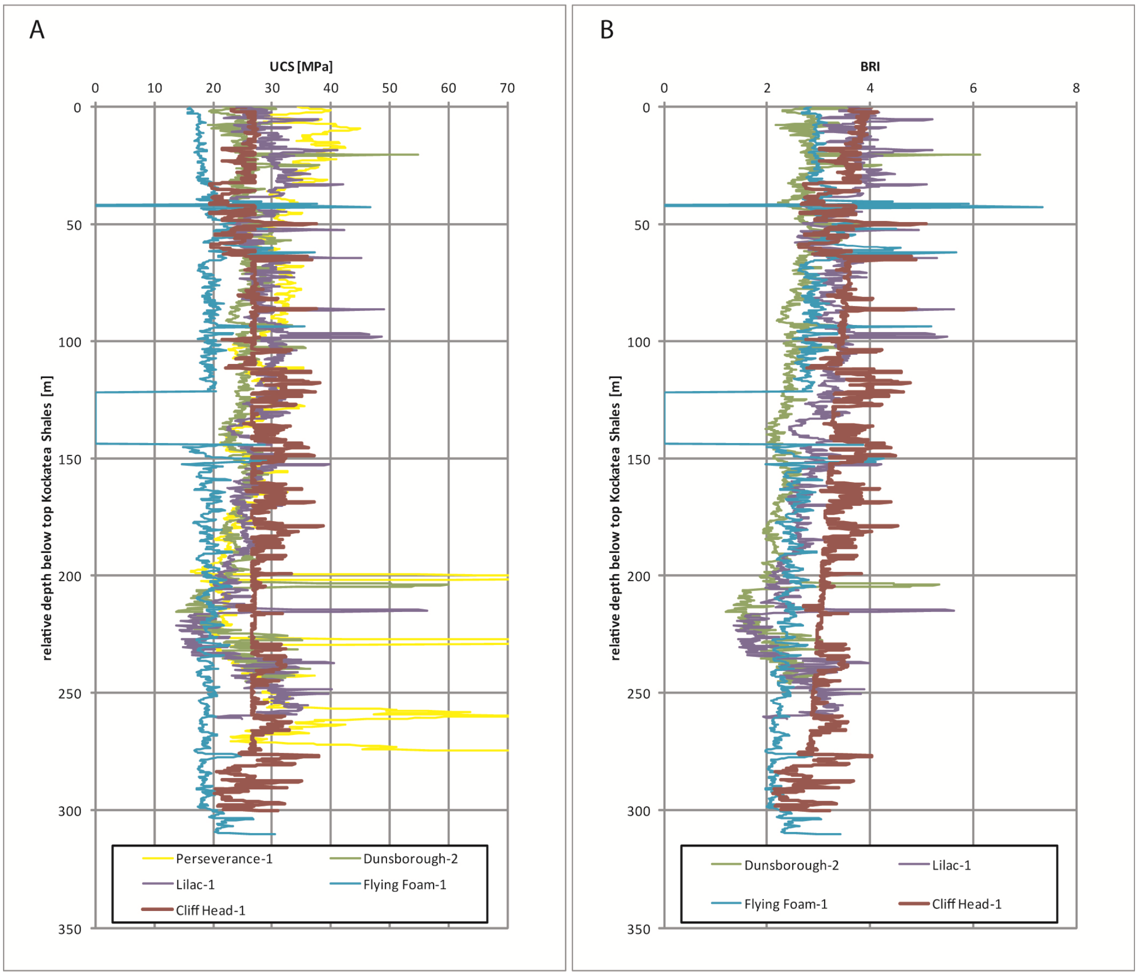

Figure 69: Mechanical properties of the Kockatea Shales seal. (A) Uniaxial compressive strength (UCS) in MPa for Cliff Head-1, Dunsborough-2, Perseverance-1, Lilac-1 and Flying Foam-1. Low UCS values represent incompetent facies and high UCS values represent competent facies; a classic range of UCS for shales is 5 MPa – 100 MPa. The soft-linkage observed over the Cliff Head oilfield cannot be attributed to a more incompetent Kockatea Shales; the average UCS for Cliff Head-1 is 28 MPa, which similar to the average UCS at locations where hard-linkage developed (Dunsborough-2, Perseverance-1, Lilac-1). (B) Brittleness index (BRI) for Cliff Head-1, Dunsborough-2, Lilac-11 and Flying Foam-1. For BRI>2 the risk of embrittlement increases with increasing BRI. The soft-linkage observed over the Cliff Head oilfield cannot be attributed to a more ductile Kockatea Shales; the BRI for Cliff Head-1 is between 3 and 6, which higher than the BRI at locations where hard-linkage developed (Dunsborough-2, Lilac-1, Flying Foam-1).

7 Limitations and Future Directions

The limitations of the methodologies used to assess the risk of top seal bypass are:

- The *geomechanical fault seal prediction* relies on the initial definition of a regional Middle Jurassic to Early Cretaceous stress field. We used a similar stress field for the *geomechanical deformation* models, but it is likely to be locally perturbed due to fault planes interaction which could impact on the fracture/slip stability and the slip/dilation tendency outcomes. However, we do not anticipate that this parameter would affect the overall risk pattern for fault seal prediction.

- The three *geomechanical deformation* models use a similar regional Middle Jurassic to Early Cretaceous stress field and variations in the stress field orientation will influence local stress and strain distribution. However, we do not expect major variations in this stress field between the Cliff Head and the Morangie structures.

- The *geomechanical fault seal prediction* tested the likelihood of fault plane failure under a specified stress regime. This represents a typical approach for up-fault flow prediction commonly utilised by the oil and gas industry. For this study we did not test cross-fault flow, as the initial seismic interpretation did not highlight a major risk of lateral flow (sand-sand juxtaposition). This is commonly assessed using fault-seal methodologies (i.e. clay smear potential, shale smear factor and predominantly, shale gouge ratio (SGR)), derived from assessing the geometry of fault juxtaposition and its interaction with the faulted lithologies. A recent study from Ciftci et al. (2012) shows a strong correlation between SGR and fault related seismic leakage indicators in the Gippsland Basin, attesting that the stress state and the lithology of a fault zone both play a major role in controlling up-fault fluid flow. A regional assessment of SGR might be a logical follow-up to this study.

8 Conclusions

- The development of faults bypassing the regional Kockatea Shale top seal represents a critical risk for trap integrity in the offshore northern Perth Basin.
- This fault bypass results from the interaction between reactivated Permian reservoir faults and the overlying faults that formed during the Middle Jurassic to Early Cretaceous reactivation event.
- The strain accommodated by the fault planes during the reactivation controls the development of hard-linkage through the top seal and the structural permeability.
- Shear and volumetric strain thresholds (0.1 and 0.05 respectively) can be defined for the specific structures and boundary conditions of our modelled areas. These values broadly differentiate fault sealing and leaking domains and could be used locally for first order structural integrity predictions. Cautions need to be taken if these predictions are to be applied to other areas with different stratigraphic architecture, pore pressure gradient and tectonic settings (i.e. bulk deformation, stress field orientation).
- The orientation of trap-bounding faults is the main factor controlling the distribution of strain and the likelihood of fault reactivation and growth. Fault segments oriented between NNW (~340°) and ESE (~100°) are more likely to fail, while fault segments oriented to the NW are more prone to seal.
- The intersection of fault planes can result in a concentration of shear deformation and dilation leading to up-fault fluid flow.
- Strain partitioning is important where large and critically oriented faults (between NNW and ESE) accommodate a large amount of the bulk deformation. This can shield the adjacent trap and help to preserve hydrocarbon.
- Variations in the top seal thickness and mechanical strength do not appear to be a key risk factor for the development of hard-linked top seal bypass.
- The high incidence of breach trap in the offshore northern Perth Basin is likely to result from the general tendency to drill structural traps that: (i) are bounded by larger faults with large offsets (i.e. larger volume but also higher risk of top seal fault breach and fault leakage) and (ii) have NNW fault orientations that align with the regional structural grain and that are prone to reactivate and leak.

REFERENCES

ABRAMS, M.A. (1996) Distribution of subsurface hydrocarbon seepage in near-surface marine sediments. AAPG Memoir 66, p. 1–14.

ANDERSON, R.N., FLEMINGS, P., LOSH, S., AUSTIN, J. AND WOODHAMS, R. (1994) Gulf of Mexico growth fault drilled, seen as oil, gas migration pathway. Oil & Gas Journal, v. 92(23), p. 97–104.

BRADSHAW, B.E., ROLLET, N., TOTTERDELL, J.M. AND BORISSOVA, I. (2003) A revised structural framework for frontier basins on the southern and southwestern Australian continental margin. Geoscience Australia, Record 2003/03.

CIFTCI, B., LANGHI, L., GIGER, S., GOLDIE-DIVKO, L., MIRANDA, J., O'BRIEN, G. (2012) Top seal bypass risk due to fracture systems, nearshore/onshore Gippsland Basin. APPEA Journal, 2012, in press.

CIFTCI, B. AND LANGHI, L. (2012) Evolution of the hourglass structures, Timor Sea, Australia: Implications for hydrocarbon traps, Journal of Structural Geology. In press.

COWIE, P. A. (1998) A healing-reloading feedback control on the growth rate of seismogenic faults: Journal of Structural Geology, v. 20, p. 1075– 1087.

CROSTELLA, A. AND BACKHOUSE, J. (2000) Geology and petroleum exploration of the central and southern Perth Basin, Western Australia. Western Australia Geological Survey, Report 57, 85p.

CROSTELLA, A. (2001) Geology and petroleum potential of the Abrolhos Sub-basin, Western Australia: Geological Survey of Western Australia, Report 75, 57 p.

CUNDALL, P. AND BOARD, M. (1988) A microcomputer program for modeling large-strain plasticity problems: Numerical Methods in Geomechanics, v. 6, p. 2101–2108.

EADINGTON P.J., LISK M. AND KRIEGER F.W. (1996) Identifying oil well sites: Patent No. 5,543,616, United States.

GARTRELL, A. P., AND M. LISK (2005) Potential new method for palaeostress estimation by combining 3D fault restoration and fault slip inversion techniques: First test on the Skua field, Timor Sea, in P. Boult and J. K. Kaldi, eds., Evaluating fault and cap rock seals: AAPG Hedberg Series 2, p. 23–36.

GARTRELL, A., BAILEY, W.R. AND BRINCAT, M. (2006) A new model for assessing trap integrity and oil preservation risks associated with postrift fault reactivation in the Timor Sea. AAPG Bulletin, v. 90(12), p. 1921–1944.

GORTER, J. AND DEIGHTON, I. (2002) Effects of igneous activity in the offshore northern Perth Basin – evidence from petroleum exploration wells, 2D seismic and magnetic surveys. In: Keep, M. and Moss, S.J. (Eds.), 2002, The Sedimentary Basins of Western Australia 3: Proceedings of the Petroleum Exploration Society of Australia Symposium, Perth, 875–899.

GEOMECHANICS INTERNATIONAL (2003) In Situ Stress, Wellbore Stability, and Fracture Permeability Cliff Head Field, Perth Basin, Australia. Memo for Roc Oil Copagny Limited (unpublished).

HARRIS, L.B. (1994) Structural and tectonic synthesis for the Perth Basin, Western Australia. Journal of Petroleum Geology, 17, 129–156.

HORSEMAN, S.T., MCCANN, D.M., MCEVAN, T.J., BRIGHTMAN, M.A. (1986) determination of the geotechnical properties of mudrocks from geophysical logging of the Harwell boreholes. Report Fluid Process Research Group, British Geological survey, FLPU, 84-14.

HORSRUD, P. (2001) Estimating mechanical properties of shale from empirical correlations. SPE Drilling and Completion 16, p. 68-73.

ITASCA (2005) Fast Lagrangian analysis of continua in 3 dimensions - User manual, version 3.1. Minneapolis, Itasca Consulting Group, Inc., 1994 p.

JONES, N.T. & HALL, A.D. (2002) The Cliff Head oil discovery – offshore Perth Basin. In: Keep, M., and Moss, S.J. (eds.) The sedimentary basins of Western Australia 3. Proceedings of the PESA Symposium, Perth, Australia, 20–23 October, 901–909.

JONES, A.T. KENNARD, J.M. NICHOLSON, C.J. BERNARDEL, G. MANTLE, D. GROSJEAN, E. BOREHAM, C.J. JORGENSEN D.C.AND ROBERTSON D. (2011) New exploration opportunities in the offshore northern Perth Basin. The APPEA Journal 51, p.45-78.

KEMPTON, R.H. (2002) Hydrocarbon charge history of the early Permian in Cliff Head-1, WA-286-P, offshore Perth Basin, Western Australia. CSIRO Division of Petroleum Resources, Confidential Report 02-054, June 2002, 41 p. A report to Roc Oil Company Limited [unpublished].

KEMPTON, R.H. (2005a) Hydrocarbon charge history of the Cliff Head Oil Field (Cliff Head-3 & -4), together with Permian reservoirs in satellite structures intersected by Mentelle-1, Twin Lions-1 and Vindara-1, WA-286-P & TP/15, Beagle Ridge, offshore Perth Basin, Western Australia. CSIRO Division of Petroleum Resources, Confidential Report 05-016, March 2005. A report to Roc Oil Company Limited [unpublished].

KEMPTON, R.H. (2005b) Investigation of hydrocarbon charge history in the Hadda-1 exploration well, WA-325-P, offshore northern Perth Basin, Western Australia. CSIRO Division of Petroleum Resources, Confidential Report 05-074, October 2005, 20 p. A report to Roc Oil (WA) Pty Ltd [unpublished].

KEMPTON, R.H. (2009a) Hydrocarbon charge in Dunsborough-1, WA-286-P, Abrolhos Sub-Basin, Australia. CSIRO Division of Petroleum Resources, Confidential Report 09-009, February 2009, 32 p. A report to Roc Oil (WA) Pty Ltd [unpublished].

KEMPTON, R.H. (2009b) Hydrocarbon charge in Dunsborough-2, WA-286-P, Abrolhos Sub-Basin, Australia. CSIRO Division of Petroleum Resources, Confidential Report 09-036, June 2009, 31 p. A report to Roc Oil (WA) Pty Ltd [unpublished].

KEMPTON, R.H. (2009c) Hydrocarbon charge in Frankland-1, WA-286-P, Abrolhos Sub-Basin, Australia. CSIRO Division of Petroleum Resources, Confidential Report 09-010, February 2009, 35 p. A report to Roc Oil (WA) Pty Ltd [unpublished].

KEMPTON, R.H. (2009d) Hydrocarbon charge in Frankland-2, WA-286-P, Abrolhos Sub-Basin, Australia. CSIRO Division of Petroleum Resources, Confidential Report 09-033, June 2009, 30 p. A report to Roc Oil (WA) Pty Ltd [unpublished].

KEMPTON, R.H. (2009e) Hydrocarbon charge in Lilac-1, WA-286-P, Abrolhos Sub-Basin, Australia. CSIRO Division of Petroleum Resources, Confidential Report 09-030, May 2009, 29 p. A report to Roc Oil (WA) Pty Ltd [unpublished].

KEMPTON, R.H. (2009f) Hydrocarbon charge in Livet-1, Abrolhos Sub-basin, Australia. CSIRO Division of Petroleum Resources, Open File Report 09-011, December 2009, 10 p. [unpublished].

KEMPTON, R.H., LIU, K., BOREHAM, C., BRADSHAW, B., EADINGTON, P. AND PASSMORE, V. (2005) Oil migration and accumulation in the offshore Perth Basin, Western Australia. CSIRO Division of Petroleum Resources, Open File Report, January 2005, 67 p. [unpublished].

KEMPTON, R., GONG, S,, KENNARD, J., VOLK, H., MILLS, D., EADINGTON, P. AND LIU, K. (2011a) Detection of Palaeo-Oil Columns in the offshore northern Perth Basin: Extension of the effective Permo-Triassic Charge System. The APPEA Journal 51, p. 377–396.

KEMPTON, R., MILLS, D., BOURDET, J. AND LIU, K. (2011b) Multi-well investigation of palaeo-hydrocarbon charge & migration in the northern offshore Perth Basin, Australia. CSIRO Earth Science & Resource Engineering, Open File Report EP113734, June 2011, 147 p [unpublished].

LANGHI, L., ZHANG, Y., GARTRELL, A., UNDERSCHULTZ, J. AND DEWHURST, D. (2010) Evaluating hydrocarbon trap integrity during fault reactivation using geomechanical three-dimensional modeling: An example from the Timor Sea, Australia. AAPG Bulletin, v. 94(4), p. 567–591.

MARSHALL, J.F., RAMSAY, D.C., MOORE, A.M.G., SHAFIK, S., GRAHAM, T.G., AND NEEDHAM, J. (1993) The Vlaming Sub-basin, offshore South Perth Basin. AGSO, Continental Margins Folio 7, 85p.

MORY, A.J. AND IASKY, R.P. (1996) Stratigraphy and structure of the onshore northern Perth Basin. Western Australia Geological Survey, Report 46.

MCLELLAN, J.G., OLIVER, N.H.S., SCHAUBS, P.M., BLENKINSOP, T.G., VEARNCOMBE, J.R. AND REDDY, S.M. (2004) Fluid flow in extensional environments, numerical modeling with an application to Hamersley iron ores. Journal of Structural Geology, v. 26(6–7), p. 1157–1171.

MEYER, V., A. NICOL, C. CHILDS, J. J. WALSH AND J. WATTERSON (2002) Progressive localisation of strain during the evolution of a normal fault population: Journal of Structural Geology, v. 24(8), p. 1215-1231.

MORY, A. J., and IASKY, R. P. (1996) Stratigraphy and structure of the onshore northern Perth Basin, Western Australia: Western Australia Geological Survey, Report 46.

MUIR-WOOD, R., KING G.C.P. (1993) Hydrological signatures of earthquake strain: Journal of Structural Geophysical Research-Solid Earth, v. 98, p. 22035-22068

NORVICK, M.S., 2004. Tectonic and stratigaphic history of the Perth Basin. Geoscience Australia Record 2004/16.

O'BRIEN, G.W, LISK, M., DUDDY, I.R., HAMILTON, J. WOODS, P. AND COWLEY, R. (1999) Plate convergence, foreland development and fault reactivation, primary controls on brine migration, thermal histories and trap breach in the Timor Sea, Australia. Marine and Petroleum Geology, v. 16(6), p.533–560.

ORD, A. (1991) Deformation of rock, a pressure-sensitive, dilatants material. Pure and Applied Geophysics, v. 137(4), p. 337–366.

ORD, A. AND OLIVER, N.H.S. (1997) Mechanical controls on fluid flow during regional metamorphism: some numerical models. Journal of Metamorphic Geology, v. 15, p. 345–359.

ORIGIN ENERGY DEVELOPMENTS PTY LTD (2003) Morangie 1 & 1ST1 Well Completion Report, WA-226-P. Origin Energy Developments Pty Ltd (unpublished).

QUAIFE, R., ROSSER, J. AND PAGNOZZI, S. (1994) The structural architecture and stratigraphy of the offshore northern Perth Basin. In: Purcell, P.G. and Purcell, R.R. (Eds.), The Sedimentary Basins of Western Australia. Proceedings of the West Australian Basins Symposium, Perth, 811–822.

ROC OIL (WA) PTY LTD. (2003) Cliff Head 3 incorporating Cliff Head 3 corehole 1 Well Completion Report Interpretation Volume. Roc Oil (WA) Pty Ltd (unpublished).

ROC OIL (WA) PTY LTD. (2004) Cliff Head Field, Cliff Head 3D MSS Interpretation Report. Roc Oil (WA) Pty Ltd (unpublished).

ROC OIL (WA) PTY LTD. (2005) Cliff Head 6 well completion report Interprative Volume. Roc Oil (WA) Pty Ltd (unpublished)

ROC OIL (WA) PTY LTD. (2006) Flying Foam-1 and Cliff Head-6, well completion report – part 2 - Interpretation. Roc Oil (WA) Pty Ltd (unpublished).

ROC OIL (WA) PTY LTD (2008) Dunsborough 1 well completion report Basic Volume. Roc Oil (WA) Pty Ltd (unpublished).

ROC OIL (WA) PTY LTD. (2009a) Dunsborough 2 well completion report Basic Volume. Roc Oil (WA) Pty Ltd (unpublished).

ROC OIL (WA) PTY LTD. (2009b) Lilac 1 well completion report Basic Volume. Roc Oil (WA) Pty Ltd (unpublished).

SANDERSON, D. J., AND X. ZHANG (1999) Critical stress localization of flow associated with deformation of well-fractured rock masses, with implications for mineral deposits: Geological Society (London) Special Publication 155, p. 69–81.

SIBSON, R.H. (1987) Earthquake rupturing as a hydrothermal mineralizing agent. Geology 15, 701-704.

SIBSON, R.H. (1996) Structural permeability of fluid-driven fault-fracture meshes. Journal of Structural Geology, v. 18, p. 1031–1042.

SMITH, D.A. (1966) Theoretical considerations of sealing and nonsealing faults. AAPG Bulletin, v. 50, p. 363– 374.

SMITH,G.C. AND COWLEY, R.G. (1987) The tectono-stratigraphy and petroleum potential of the northern Abrolhos Sub-basin, Western Australia. The APEA Journal, 27(1), 112–135

SONG, T. AND CAWOOD, P.A. (2000) Structural styles in the Perth Basin associated with the Mesozoic breakup of Greater India and Australia. Tectonophysics, 317, 55–72.

STRAYER, L.M., HUDLESTON, P.J. AND LORIG, L.J. (2001) A numerical model of deformation and fluid-flow in an evolving thrust wedge. Tectonophysics, v. 335, no. 1–2, p. 121–145.

VERMEER, P.A. AND DE BURST, R. (1984) Non-associated plasticity for soils, concrete and rocks. Heron, v. 29, p. 1–64.

WILKINS S. J., NARUK S. J. (2007) Quantitative analysis of slip-induced dilation with application to fault seal. AAPG Bulletin, v. 91, p. 97–113.

WIPRUT, D. AND ZOBACK, M.D. (2000) Fault reactivation and fluid flow along a previously dormant normal fault in the northern North Sea. Geology, 28, 595-598.

ZHANG, Y., GARTRELL, A., UNDERSCHULTZ, J.R. AND DEWHURST, D.N. (2009) Numerical modeling of strain localization and fluid flow during extensional fault reactivation: Implications for hydrocarbon preservation. Journal of Structural Geology, v. 31, p. 315–327.

APPENDIX A – PALAEO-OIL CHARGE RECONSTRUCTIONS

Specialised fluid inclusion technologies (GOI™; Eadington et al., 1996) have been used to identify a widespread charge system for oil accumulation below the Kockatea Shale regional seal in the offshore northern Perth Basin, with a series of palaeo-oil columns detected (Kempton, 2002, 2005a, 2005b; Kempton et al., 2005; Kempton 2009a, 2009b, 2009c, 2009d, 2009e, 2009f; Kempton et al., 2011a; Kempton et al., 2011b). These include those at the Cliff Head, Dunsborough, Frankland and Perseverance oil and gas fields, and in dry wells at Flying Foam–1, Geelvink-1A, Hadda–1, Houtman–1, Leander Reef–1, Lilac–1, Livet–1, Mentelle–1 and Morangie–1. Palaeo-oil charge reconstructions for the Cliff Head oilfield, Dunsborough oil/gas discovery, Lilac-1 and Morangie-1—which provide background to the geomechanical models in this study—are detailed below.

Cliff Head Oilfield

Palaeo-oil is only detected in oil zone samples from the Dongara Sandstone and Irwin River Coal Measures in Cliff Head-3 above 1300 mMD (1,236 mTVDSS; Figure 70). Oil inclusions have not formed within all of the present day oil-leg and are recorded in low abundance in oil zone samples below 1310 mMD (1,246 mTVDSS) in Cliff Head-3 and all oil zone samples from Cliff Head-1 and -4. The trapping of inclusion oil ceased before the oil zone reached its present configuration and the palaeo-oil zone in Cliff Head-3 represents a snapshot of oil in the reservoir—perhaps closure that was filled to spill prior to enhancement of the structure.

Dunsborough Oil/Gas Discovery

A palaeo-oil column is detected in the Dongara Sandstone and Irwin River Coal Measures in Dunsborough–1 (Figure 71). The lowermost detectable limit of palaeo-oil is down-to 1,518.2 mMD—52 m below the Kockatea seal—and close to an inferred base seal (Roc Oil (WA) Pty Ltd personal correspondence) within the Irwin River Coal Measures. In Dunsborough–2, palaeo-oil is detected down to 1,531 mMD—16 m below the Kockatea seal in this well intersection. The highest known palaeo-water zone sample from GOI is at 1,545 mMD and this refers to when fluid inclusions were forming in quartz cement.

A zone of carbonate cement, which crystallised after oil inclusions were trapped in quartz cement, also contains frequent oil inclusions by visual estimation (i.e. qualitative assessment). In Dunsborough–1 this is over the same depth interval as palaeo-oil zone from GOI and about coincident with oil shows from side-wall cores (SWC's) and cuttings. The highest known water zone at this time was at 1,571.8 mMD (the only other sample below this that had carbonate cement). In Dunsborough–2, the presence of oil inclusions in carbonate cement extends below the zone defined by GOI, possibly suggesting deepening of the palaeo-oil column at this location and a multi-stage fill history. Palaeo oil at this time was down-to 1,570 mMD, but above water zone at 1,573 mMD, and is coincident with the base of oil shows at 1,570 mMD.

Lilac-1

A palaeo-oil column is detected in the Dongara Sandstone and Irwin River Coal Measures of the Lilac–1 dry well (Figure 72). Sample spacing limits detection of palaeo-oil above 1,384.5 mMD, with the uppermost GOI cuttings sample being from across the Kockatea\Dongara contact. A palaeo-oil water contact is bracketed at 1,420 m by consecutive cuttings samples.

Morangie-1

A palaeo-oil column is interpreted from elevated GOI (4.3% to 18.7%) in the Dongara Sandstone of the Morangie-1 dry well (Figure 73) over a 52 m gross interval from below the Kockatea seal down to 2160 mMD (base of cuttings sample). This extends well below the zone of oil shows from SWC and indicates filling of the structure to deeper levels than would be indicated by conventional oil shows alone. The total depth of the palaeo-oil column, from GOI, is unconstrained by current sample spacing and a palaeo-oil water contact is not bracketed.

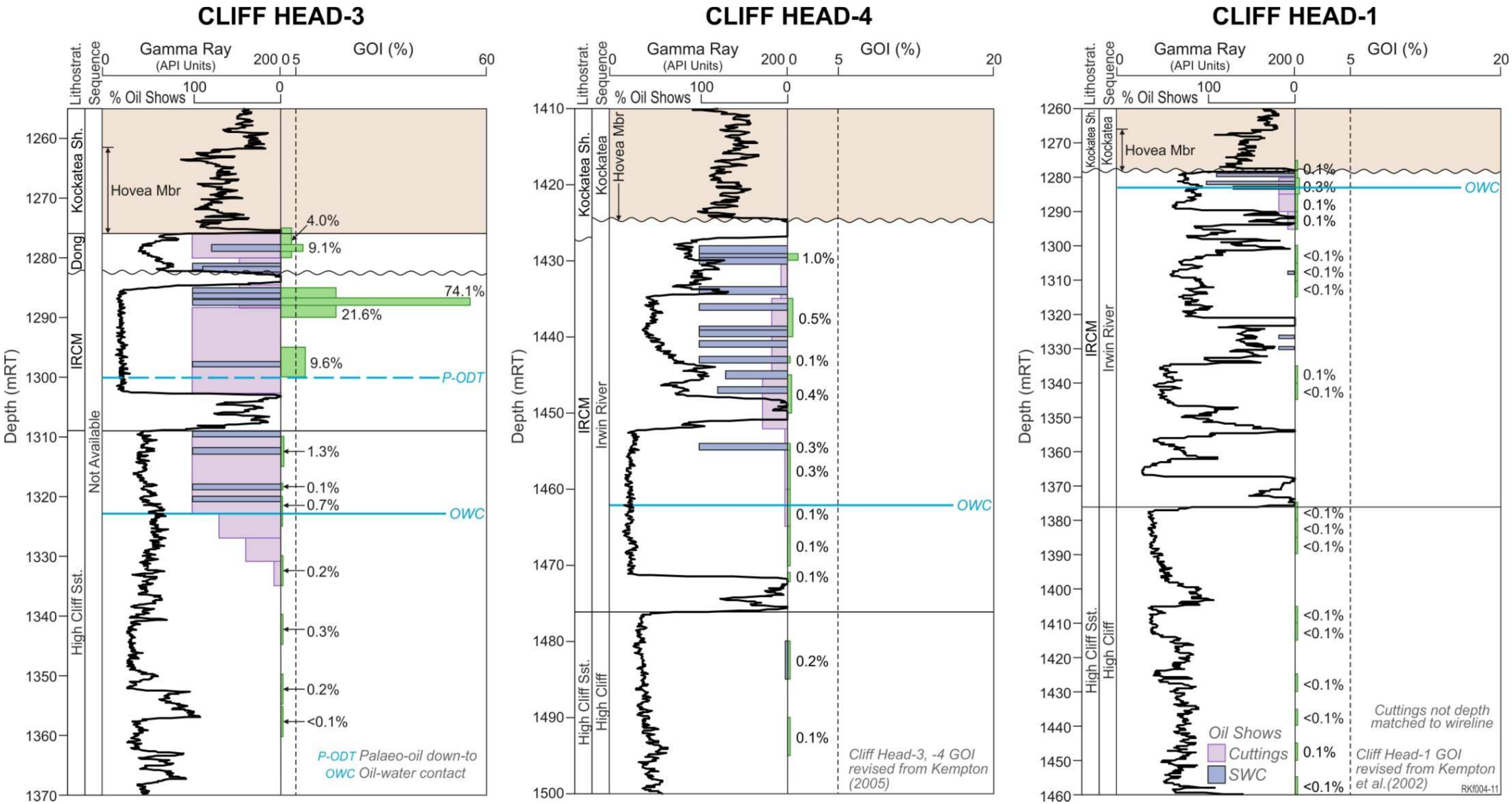

Figure 70: Cliff Head oilfield— GOI log.

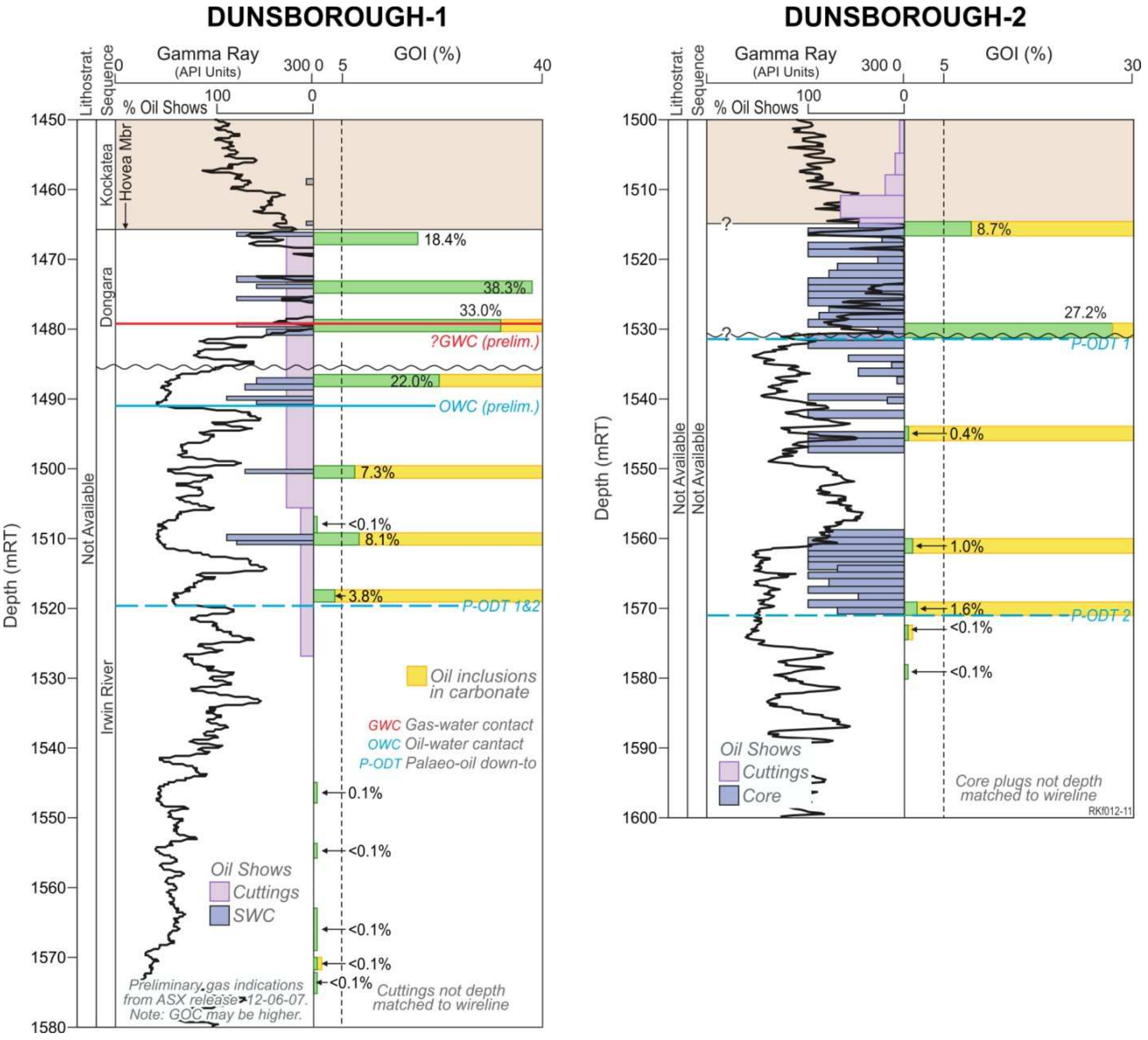

Figure 71: Dunsborough oil/gas discovery— GOI log.

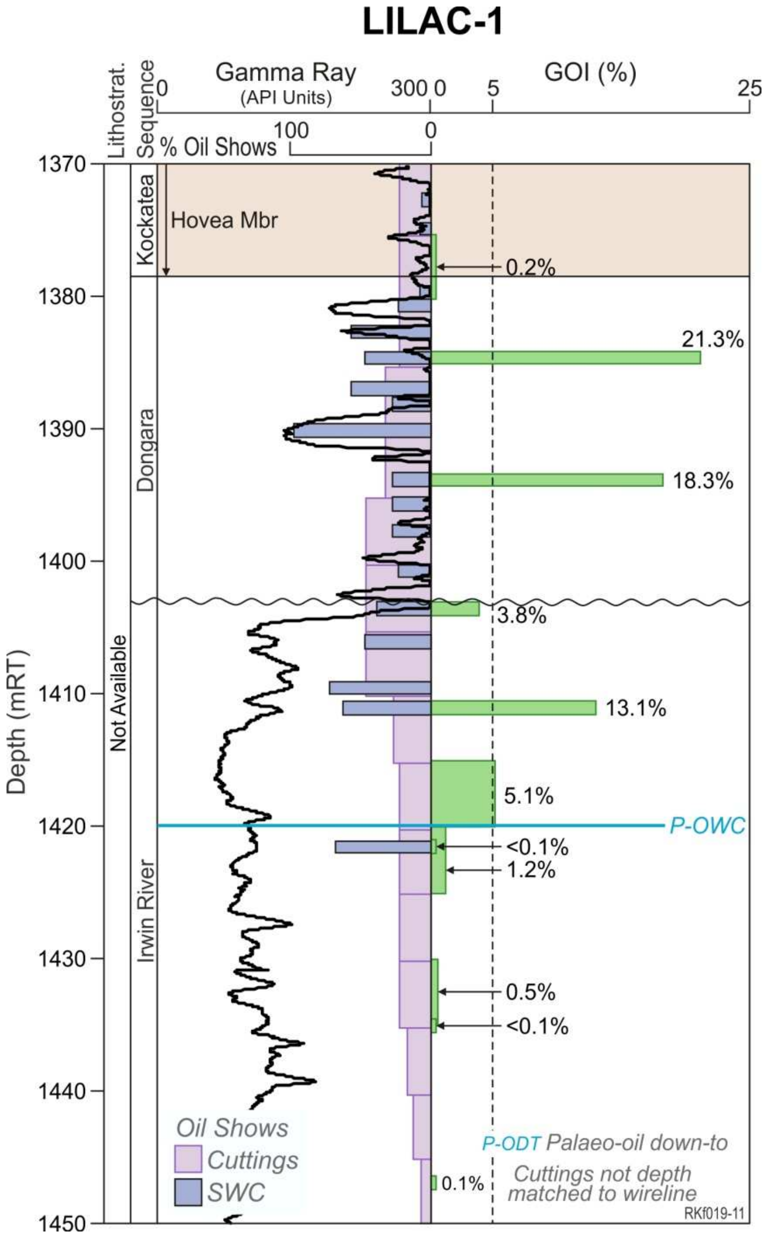

Figure 72: Lilac-1— GOI log.

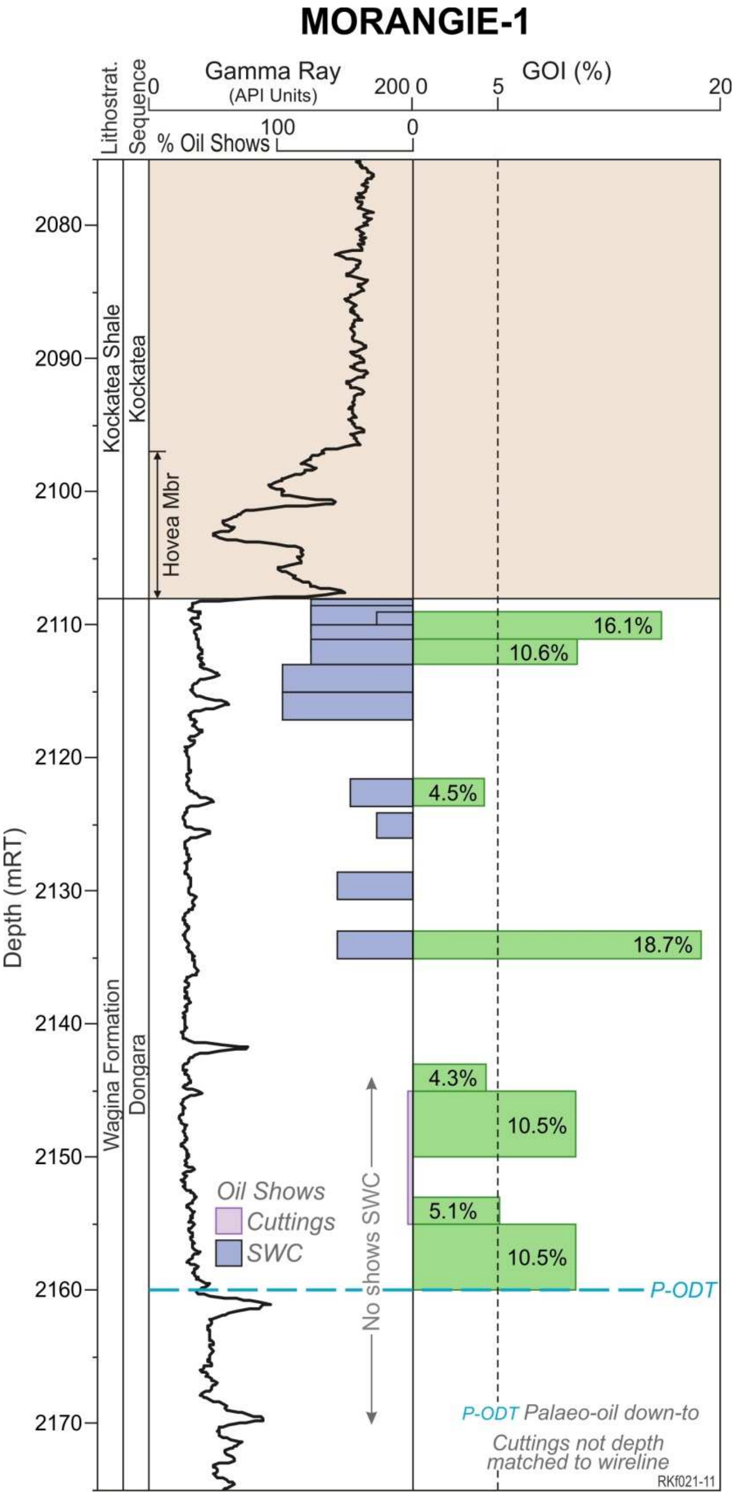

Figure 73: Morangie-1— GOI log.

CONTACT US

t 1300 363 400
+61 3 9545 2176
e enquiries@csiro.au
w www.csiro.au

YOUR CSIRO

Australia is founding its future on science and innovation. Its national science agency, CSIRO, is a powerhouse of ideas, technologies and skills for building prosperity, growth, health and sustainability. It serves governments, industries, business and communities across the nation.

FOR FURTHER INFORMATION

CSIRO EARTH SCIENCE AND RESOURCE ENGINEERING
Dr. Laurent Langhi
t +61 8 6436 8741
e Laurent.langhi@csiro.au

CSIRO EARTH SCIENCE AND RESOURCE ENGINEERING
Dr Richard Kempton
t +61 8 6436 8537
e Richard.kempton@csiro.au